NMR | MRI

BIOLOGY | CHEMISTRY | MEDICINE | PHYSICS

HANDBOOK OF MAGNETIC RESONANCE SPECTROSCOPY IN VIVO

MRS THEORY, PRACTICE AND APPLICATIONS

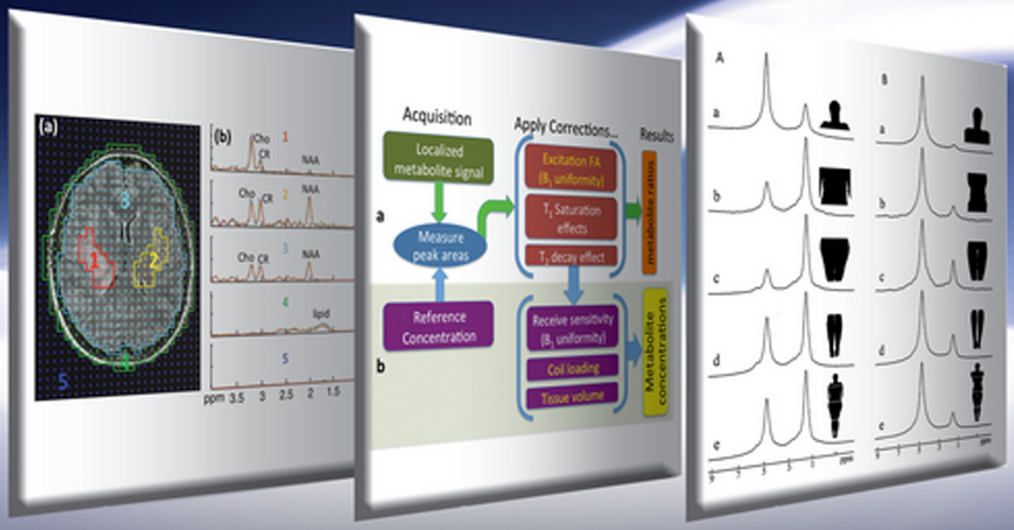

Editors | Paul A. Bottomley | John R. Griffiths

eMagRes BOOKS

Visit eMagRes at
www.wileyonlinelibrary.com/ref/eMagRes

WILEY

Handbook of Magnetic Resonance Spectroscopy In Vivo: MRS Theory, Practice and Applications

eMagRes Books

eMagRes (formerly the *Encyclopedia of Magnetic Resonance*) publishes a wide range of online articles on all aspects of magnetic resonance in physics, chemistry, biology and medicine. The existence of this large number of articles, written by experts in various fields, is enabling the publication of a series of *eMagRes* Books – handbooks on specific areas of NMR and MRI. The chapters of each of these handbooks will comprise a carefully chosen selection of *eMagRes* articles.

Published *eMagRes* Books

NMR Crystallography
Edited by Robin K. Harris, Roderick E. Wasylishen, Melinda J. Duer
ISBN 978-0-470-69961-4

Multidimensional NMR Methods for the Solution State
Edited by Gareth A. Morris, James W. Emsley
ISBN 978-0-470-77075-7

Solid-State NMR Studies of Biopolymers
Edited by Ann E. McDermott, Tatyana Polenova
ISBN 978-0-470-72122-3

NMR of Quadrupolar Nuclei in Solid Materials
Edited by Roderick E. Wasylishen, Sharon E. Ashbrook, Stephen Wimperis
ISBN 978-0-470-97398-1

RF Coils for MRI
Edited by John T. Vaughan, John R. Griffiths
ISBN 978-0-470-77076-4

MRI of Tissues with Short T_2s or T_2^*s
Edited by Graeme M. Bydder, Gary D. Fullerton, Ian R. Young
ISBN 978-0-470-68835-9

NMR Spectroscopy: A Versatile Tool for Environmental Research
Edited by Myrna J. Simpson, André J. Simpson
ISBN 978-1-118-61647-5

NMR in Pharmaceutical Sciences
Edited by Jeremy R. Everett, Robin K. Harris, John C. Lindon, Ian D. Wilson
ISBN 978-1-118-66025-6

Handbook of Magnetic Resonance Spectroscopy In Vivo: MRS Theory, Practice and Applications
Edited by Paul A. Bottomley, John R. Griffiths
ISBN 978-1-118-99766-6

Forthcoming *eMagRes* Books

EPR Spectroscopy
Edited by Daniella Goldfarb, Stefan Stoll
ISBN 978-1-119-16299-5

eMagRes

Edited by Roderick E. Wasylishen, Edwin D. Becker, Marina Carravetta, George A. Gray, John R. Griffiths, Tatyana Polenova, André J. Simpson, Myrna J. Simpson, Ian R. Young.

eMagRes (formerly the *Encyclopedia of Magnetic Resonance*) is based on the original publication of the *Encyclopedia of Nuclear Magnetic Resonance*, first published in 1996 with an updated volume added in 2000. The *Encyclopedia of Magnetic Resonance* was launched in 2007 online with all the existing published material, and was later relaunched as *eMagRes* in 2013. New updates are added on a regular basis through the year to keep content up to date with current developments. NMR and MRI have developed into two very different research and application areas with their own dynamic development. *eMagRes* addresses this development by presenting the content as two separate topics. Readers can browse through the extensive lists of either the NMR topics or the MRI topics.

For more information see: http://www.wileyonlinelibrary.com/ref/eMagRes

Handbook of Magnetic Resonance Spectroscopy In Vivo: MRS Theory, Practice and Applications

Editors

Paul A. Bottomley
Johns Hopkins University, Baltimore, MD, USA

John R. Griffiths
Cancer Research UK, Cambridge Research Institute, Cambridge, UK

WILEY

This edition first published 2016

Registered office
John Wiley & Sons Ltd, The Atrium, Southern Gate, Chichester, West Sussex,
PO19 8SQ, United Kingdom

Library of Congress Cataloging-in-Publication Data

Names: Bottomley, Paul A., editor. | Griffiths, John R., 1945- editor.
Title: Handbook of magnetic resonance spectroscopy in vivo : MRS theory, practice and applications / editors, Paul A. Bottomley, John R. Griffiths.
Description: Chichester, West Sussex, United Kingdom: John Wiley & Sons Ltd, 2016. | Includes bibliographical references and index.
Identifiers: LCCN 2016032970| ISBN 9781118997666 (cloth) | ISBN 9781118997697 (Adobe PDF) | ISBN 9781118997673 (epub)
Subjects: | MESH: Magnetic Resonance Imaging--methods | Magnetic Resonance Imaging--instrumentation | Magnetic Resonance Spectroscopy--methods
Classification: LCC RC386.6.M34 | NLM WN 185 | DDC 616.07/548--dc23 LC record available at https://lccn.loc.gov/2016032970

A catalogue record for this book is available from the British Library.

ISBN: 978-1-118-99766-6

Front Cover: Left image adapted from Reference 28 of Chapter 11, Copyright 2013, with permission from Elsevier. Right image adapted from Reference 28 of Chapter 44, Copyright 2001, with permission from Elsevier.

Set in 9.5/11.5 pt TimesLTStd by SPi Global, Chennai, India

1 2016

eMagRes

Editorial Board

MRI & MRS

John R. Griffiths
Cancer Research UK
Cambridge Research Institute
Cambridge
UK

Ian R. Young
Imperial College
London
UK

HISTORICAL PERSPECTIVES

Edwin D. Becker
National Institutes of Health
Bethesda, MD
USA

International Advisory Board

George K. Radda
University of Oxford
Oxford
UK

Hans Wolfgang Spiess
Max-Planck Institute
of Polymer Research
Mainz
Germany

Charles P. Slichter
University of Illinois
at Urbana-Champaign
Urbana, IL
USA

John S. Waugh (deceased)
Massachusetts Institute
of Technology (MIT)
Cambridge, MA
USA

Bernd Wrackmeyer
Universität Bayreuth
Bayreuth
Germany

Kurt Wüthrich
The Scripps Research
Institute
La Jolla, CA
USA

and

ETH Zürich
Zürich
Switzerland

Contents

Contributors

Fernando Arias-Mendoza *University of Pennsylvania Health System, Philadelphia, PA, USA*
Chapter 60: Clinical Trials of MRS Methods

Carles Arús *Centro de Investigación Biomédica en Red (CIBER), Cerdanyola del Vallès, Spain*
Universitat Autònomade de Barcelona (UAB), Cerdanyola del Vallès, Spain
Chapter 22: Pattern Recognition Analysis of MR Spectra

Peter B. Barker *The Johns Hopkins University School of Medicine, Baltimore, MD, USA*
Kennedy Krieger Institute, Baltimore, MD, USA
Chapter 18: Quantifying Spectra in the Frequency Domain

Michael J. Barlow *University of Nottingham, Nottingham, UK*
Chapter 33: Hyperpolarization Methods for MRS

Jimmy D. Bell *University of Westminster, London, UK*
Chapter 44: Body Fat MRS

Monique Bernard *Aix-Marseille Université, Marseille, France*
Chapter 50: Assessing Cardiac Transplant Viability with MRS

Jonathan R. Birchall *University of Nottingham, Nottingham, UK*
Chapter 33: Hyperpolarization Methods for MRS

Andrew M. Blamire *Newcastle University, Newcastle upon Tyne, UK*
Chapter 54: Studying Stroke and Cerebral Ischemia by ^{1}H MRS

Chris Boesch *University and Inselspital Bern, Bern, Switzerland*
Chapter 41: Muscle Studies by ^{1}H MRS

Paul A. Bottomley *Johns Hopkins University, Baltimore, MD, USA*
Chapter 1: Basics of NMR
Chapter 11: Accelerated Spatially-Encoded MRS of Arbitrarily-Shaped Compartments Using Linear Algebraic Modeling
Chapter 24: Quantifying Metabolite Ratios and Concentrations by Non-^{1}H MRS
Chapter 28: Measuring Biochemical Reaction Rates In Vivo with Magnetization Transfer
Chapter 51: MRS in the Failing Heart: From Mice to Humans
Chapter 52: MRS Studies of Creatine Kinase Metabolism in Human Heart
Appendix 1: Properties of NMR-Visible Isotopes and their Biological Content in Human Tissues
Appendix 5: Some Standard Formulae Used in MRS
Appendix 6: Common MRS Artifacts

Elizabeth A. Browning *University of Pennsylvania, Philadelphia, PA, USA*
Chapter 35: MRS of Perfused Cells, Tissues, and Organs

Thierry Caus *Amiens-Picardie Hospital, Amiens, France*
Chapter 50: Assessing Cardiac Transplant Viability with MRS

Eduard Y. Chekmenev *Vanderbilt University, Nashville, TN, USA*
Chapter 33: Hyperpolarization Methods for MRS

Yuen-Li Chung *The Institute of Cancer Research, London, UK*
Chapter 36: Metabolism and Metabolomics by MRS

Kieran Clarke *University of Oxford, Oxford, UK*
Chapter 49: Cardiac MRS Studies in Rodents and Other Animals

Aaron M. Coffey *Vanderbilt University, Nashville, TN, USA*
Chapter 33: Hyperpolarization Methods for MRS

Robin A. de Graaf *MRRC, Yale University, New Haven, CT, USA*
Chapter 5: Adiabatic Excitation Pulses for MRS
Chapter 31: Spectral Editing

E. James Delikatny *University of Pennsylvania, Philadelphia, PA, USA*
Chapter 35: MRS of Perfused Cells, Tissues, and Organs

Michael S. Dodd *University of Oxford, Oxford, UK*
Chapter 49: Cardiac MRS Studies in Rodents and Other Animals

Ulrike Dydak *Purdue University, West Lafayette, IN, USA*
Indiana University School of Medicine, Indianapolis, IN, USA
Chapter 8: Chemical Shift Imaging with Phase and Sensitivity Encoding

Richard A.E. Edden *The Johns Hopkins University School of Medicine, Baltimore, MD, USA*
Kennedy Krieger Institute, Baltimore, MD, USA
Chapter 56: The Significance of *N*-Acetyl Aspartate in Human Brain MRS

Uzi Eliav *Tel Aviv University, Tel Aviv, Israel*
Chapter 32: Multiple Quantum MRS

Pedro M. Enriquez-Navas *H. Lee Moffitt Cancer Center, Tampa, FL, USA*
Chapter 25: Measuring Intra- and Extracellular pH by MRS

J. Eric Jensen *McLean Hospital, Belmont, MA, USA*
Harvard Medical School, Boston, MA, USA
Chapter 55: ^{31}P MRS in Psychiatric Disorders

Michael Garwood *University of Minnesota, Minneapolis, MN, USA*
Chapter 6: Localized MRS Employing Radiofrequency Field (B_1) Gradients

Max E. Gemeinhardt *Southern Illinois University, Carbondale, IL, USA*
Chapter 33: Hyperpolarization Methods for MRS

Robert J. Gillies *H. Lee Moffitt Cancer Center, Tampa, FL, USA*
Chapter 25: Measuring Intra- and Extracellular pH by MRS

Lidia Glodzik *New York University School of Medicine, New York, NY, USA*
Chapter 53: Studying Aging, Dementia, Trauma, Infection, and Developmental Disorders of the Brain with ^{1}H MRS

Oded Gonen *New York University School of Medicine, New York, NY, USA*
Chapter 53: Studying Aging, Dementia, Trauma, Infection, and Developmental Disorders of the Brain with ^{1}H MRS

Boyd M. Goodson *Southern Illinois University, Carbondale, IL, USA*
Chapter 33: Hyperpolarization Methods for MRS

Jeremy W. Gordon *University of California – San Francisco, San Francisco, CA, USA*
Chapter 34: Pulse Sequences for Hyperpolarized MRS

Varan Govind *University of Miami, Miami, FL, USA*
Chapter 21: ^{1}H-NMR Chemical Shifts and Coupling Constants for Brain Metabolites
Appendix 4: Biochemical Reactions and Molecular Structures of Common MRS Metabolites

Danielle Graveron-Demilly *Laboratoire CREATIS, CNRS UMR 5220, Inserm U1044, Université Claude Bernard LYON 1, INSA Lyon, Lyon, France*
Chapter 19: Quantifying Spectra in the Time Domain

John R. Griffiths *Cancer Research UK, Cambridge Research Institute, Cambridge, UK*
Chapter 36: Metabolism and Metabolomics by MRS
Chapter 60: Clinical Trials of MRS Methods
Chapter 61: Clinical Trials that Utilize MRS as a Biomarker
Appendix 4: Biochemical Reactions and Molecular Structures of Common MRS Metabolites
Appendix 6: Common MRS Artifacts
Appendix 7: In Vivo Spectra with Peak Assignments

Ashish Gupta
Johns Hopkins Hospital, Baltimore, MD, USA
Chapter 51: MRS in the Failing Heart: From Mice to Humans

Brogan M. Gust
Southern Illinois University, Carbondale, IL, USA
Chapter 33: Hyperpolarization Methods for MRS

David G. Harper
McLean Hospital, Belmont, MA, USA
Harvard Medical School, Boston, MA, USA
Chapter 55: ^{31}P MRS in Psychiatric Disorders

Ashley D. Harris
The Johns Hopkins University School of Medicine, Baltimore, MD, USA
Kennedy Krieger Institute, Baltimore, MD, USA
University of Calgary, Calgary, Canada
Chapter 56: The Significance of *N*-Acetyl Aspartate in Human Brain MRS

Arend Heerschap
Radboud University Medical Center Nijmegen, Nijmegen, The Netherlands
Chapter 37: In Vivo ^{19}F MRS

Anke Henning
Max Planck Institute of Biological Cybernetics, Tübingen, Germany
University and ETH Zurich, Zürich, Switzerland
Chapter 20: Advanced Spectral Quantification: Parameter Handling, Nonparametric Pattern Modeling, and Multidimensional Fitting

Diego Hernando
University of Wisconsin-Madison, Madison, WI, USA
Chapter 13: Direct Water–Fat Imaging Methods: Chemical Shift-Selective and Chemical Shift-Encoded MRI

Davina J. Honess
CRUK Cambridge Institute, Cambridge, UK
Chapter 14: Physiological Maintenance in Animal Experiments

David Hoult
David Hoult Consulting Ltd., Winnipeg, Manitoba, Canada
Chapter 2: Magnetic Resonance Spectroscopy Instrumentation

Franklyn A. Howe
University of London, London, UK
Chapter 57: MRS in Brain Cancer

Houchun Harry Hu
Phoenix Children's Hospital, Phoenix, AZ, USA
Chapter 13: Direct Water–Fat Imaging Methods: Chemical Shift-Selective and Chemical Shift-Encoded MRI

Xiaoping Hu
Georgia Tech and Emory University, Atlanta, GA, USA
Chapter 12: High-Speed Spatial–Spectral Encoding with Echo-Planar and Spiral Spectroscopic Imaging

Amir Huda
University of California, Los Angeles, CA, USA
California State University, Fresno, CA, USA
Chapter 30: Two-Dimensional NMR Spectroscopy Plus Spatial Encoding

Zohaib Iqbal
University of California, Los Angeles, CA, USA
Chapter 30: Two-Dimensional NMR Spectroscopy Plus Spatial Encoding

Naranamangalam R. Jagannathan
All India Institute of Medical Sciences, New Delhi, India
Chapter 58: MRS in Breast Cancer

Thomas Jue
University of California Davis, Davis, CA, USA
Chapter 43: Measuring Intracellular Oxygenation with Myoglobin ^{1}H MRS

Margarida Julià-Sapé
Centro de Investigación Biomédica en Red (CIBER), Cerdanyola del Vallès, Spain
Universitat Autònomade de Barcelona (UAB), Cerdanyola del Vallès, Spain
Chapter 22: Pattern Recognition Analysis of MR Spectra
Chapter 60: Clinical Trials of MRS Methods

Graham J. Kemp
University of Liverpool, Liverpool, UK
Chapter 42: Muscle Studies by ^{31}P MRS

Markus von Kienlin
Roche Innovation Center Basel, Basel, Switzerland
Chapter 10: Accurate Localized Spectroscopy from Anatomically Matched Regions with Optimal Spatial Response Function

Ivan I. Kirov
New York University School of Medicine, New York, NY, USA
Chapter 53: Studying Aging, Dementia, Trauma, Infection, and Developmental Disorders of the Brain with ^{1}H MRS
Appendix 2: Concentration Ranges of Common Metabolites Detected by MRS in Healthy Human Tissue

Frank Kober
Aix-Marseille Université, Marseille, France
Chapter 50: Assessing Cardiac Transplant Viability with MRS

Dara L. Kraitchman
Johns Hopkins University, Baltimore, MD, USA
Chapter 15: Physiological Maintenance in MRI and MRS of Large Animals

Roland Kreis
University and Inselspital Bern, Bern, Switzerland
Chapter 41: Muscle Studies by ^{1}H MRS
Appendix 6: Common MRS Artifacts

Rebecca A. Krimins
Johns Hopkins University, Baltimore, MD, USA
Chapter 15: Physiological Maintenance in MRI and MRS of Large Animals

Martin Krššák
Medical University of Vienna, Vienna, Austria
Chapter 38: ^{13}C MRS in Human Tissue

John Kurhanewicz
University of California, San Francisco, CA, USA
Chapter 39: Hyperpolarized ^{13}C MRI and MRS Studies
Chapter 59: MRS in Prostate Cancer

Kagayaki Kuroda
Tokai University, Hiratsuka, Japan
Chapter 26: Temperature Monitoring Using Chemical Shift

Russell Lagore
University of Minnesota, Minneapolis, MN, USA
Chapter 3: Detection Coils for MRS

Fan Lam
University of Illinois at Urbana-Champaign, Champaign, IL, USA
Chapter 9: Encoding and Decoding with Prior Knowledge: From SLIM to SPICE

Peder E.Z. Larson
University of California – San Francisco, San Francisco, CA, USA
Chapter 34: Pulse Sequences for Hyperpolarized MRS

Zhi-Pei Liang
University of Illinois at Urbana-Champaign, Champaign, IL, USA
Chapter 9: Encoding and Decoding with Prior Knowledge: From SLIM to SPICE

Alexander Lin
Harvard Medical School, Boston, CA, USA
Chapter 61: Clinical Trials that Utilize MRS as a Biomarker

Paulo Lisboa
Liverpool John Moores University, Liverpool, UK
Chapter 22: Pattern Recognition Analysis of MR Spectra

E. Louise Thomas
University of Westminster, London, UK
Chapter 44: Body Fat MRS

Chao Ma
University of Illinois at Urbana-Champaign, Champaign, IL, USA
Chapter 9: Encoding and Decoding with Prior Knowledge: From SLIM to SPICE

Paul M. Macey
University of California, Los Angeles, CA, USA
Chapter 30: Two-Dimensional NMR Spectroscopy Plus Spatial Encoding

Jürgen Machann
University of Tübingen, Tübingen, Germany
German Center for Diabetes Research (DZD), Neuherberg, Germany
Chapter 45: In Vivo MRS of Lipids in Adipose Tissue, Bone Marrow, and Liver

Basetti Madhu
University of Cambridge, Cambridge, UK
Chapter 36: Metabolism and Metabolomics by MRS

Craig R. Malloy
University of Texas Southwestern Medical Center, Dallas, TX, USA
UT Southwestern Medical Center and the VA North Texas Health Care System, Dallas, TX, USA
Chapter 40: Integrating ^{13}C Isotopomer Methods with Hyperpolarization for a Comprehensive Picture of Metabolism

Dominick J.O. McIntyre *CRUK Cambridge Institute, Cambridge, UK*
Chapter 4: A Practical Guide to In Vivo MRS

Mary A. McLean *University of Cambridge, Cambridge, UK*
Chapter 23: Quantifying Metabolite Ratios and Concentrations by ^{1}H MRS

David Menon *University of Cambridge, Cambridge, UK*
Chapter 16: Physiological Monitoring in Human MRS

Matthew Milkevitch *Philadelphia University, Philadelphia, PA, USA*
Chapter 35: MRS of Perfused Cells, Tissues, and Organs

Rajakumar Nagarajan *University of California, Los Angeles, CA, USA*
Chapter 30: Two-Dimensional NMR Spectroscopy Plus Spatial Encoding

Gil Navon *Tel Aviv University, Tel Aviv, Israel*
Chapter 32: Multiple Quantum MRS

Virginia Newcombe *University of Cambridge, Cambridge, UK*
Chapter 16: Physiological Monitoring in Human MRS

Klaas Nicolay *Eindhoven University of Technology, Eindhoven, The Netherlands*
Chapter 47: MRS Studies of Muscle and Heart in Obesity and Diabetes

Panayiotis Nikolaou *Vanderbilt University, Nashville, TN, USA*
Chapter 33: Hyperpolarization Methods for MRS

Dirk van Ormondt *TU Delft, Delft, The Netherlands*
Chapter 19: Quantifying Spectra in the Time Domain

Sandra Ortega-Martorell *Liverpool John Moores University, Liverpool, UK*
Centro de Investigación Biomédica en Red (CIBER), Cerdanyola del Vallès, Spain
Chapter 22: Pattern Recognition Analysis of MR Spectra

Geoffrey S. Payne *The Institute of Cancer Research and Royal Marsden Hospital, Surrey, UK*
Chapter 7: Single Voxel MRS

Andrew C. Peet *Institute of Child Health, Birmingham, UK*
Chapter 57: MRS in Brain Cancer

Stefan Posse *University of New Mexico, Albuquerque, NM, USA*
Chapter 12: High-Speed Spatial–Spectral Encoding with Echo-Planar and Spiral Spectroscopic Imaging

Subechhya Pradhan *The Johns Hopkins University School of Medicine, Baltimore, MD, USA*
Chapter 18: Quantifying Spectra in the Frequency Domain

Jeanine J. Prompers *Eindhoven University of Technology, Eindhoven, The Netherlands*
Chapter 47: MRS Studies of Muscle and Heart in Obesity and Diabetes

Eva-Maria Ratai *Massachusetts General Hospital and Harvard Medical School, Charlestown, MA, USA*
Chapter 53: Studying Aging, Dementia, Trauma, Infection, and Developmental Disorders of the Brain with ^{1}H MRS

Perry F. Renshaw *University of Utah, Salt Lake City, UT, USA*
Chapter 55: ^{31}P MRS in Psychiatric Disorders

Itamar Ronen *Leiden University Medical Center, Leiden, The Netherlands*
Chapter 27: Diffusion-Weighted MRS

Douglas L. Rothman *MRRC, Yale University, New Haven, CT, USA*
Chapter 31: Spectral Editing

Ben Rowland *Harvard Medical School, Boston, CA, USA*
Chapter 61: Clinical Trials that Utilize MRS as a Biomarker

Manoj K. Sarma *University of California, Los Angeles, CA, USA*
Chapter 30: Two-Dimensional NMR Spectroscopy Plus Spatial Encoding

Michael Schär *Johns Hopkins University, Baltimore, MD, USA*
Chapter 8: Chemical Shift Imaging with Phase and Sensitivity Encoding
Chapter 17: Physiologic Motion: Dealing with Cardiac, Respiratory, and Other Sporadic Motion in MRS

Fritz Schick *University of Tübingen, Tübingen, Germany*
German Center for Diabetes Research (DZD), Neuherberg, Germany
Chapter 45: In Vivo MRS of Lipids in Adipose Tissue, Bone Marrow, and Liver

Akansha Ashvani Sehgal *The Johns Hopkins University School of Medicine, Baltimore, MD, USA*
Kennedy Krieger Institute, Baltimore, MD, USA
Chapter 29: Proton Chemical Exchange Saturation Transfer MRS and MRI

Uma Sharma *All India Institute of Medical Sciences, New Delhi, India*
Chapter 58: MRS in Breast Cancer

A. Dean Sherry *University of Texas Southwestern Medical Center, Dallas, TX, USA*
University of Texas at Dallas, Richardson, TX, USA
Chapter 40: Integrating ^{13}C Isotopomer Methods with Hyperpolarization for a Comprehensive Picture of Metabolism
Appendix 3: Peak Assignments for Some Common Metabolites

Roman V. Shchepin *Vanderbilt University, Nashville, TN, USA*
Chapter 33: Hyperpolarization Methods for MRS

Fan Shi
Southern Illinois University, Carbondale, IL, USA
Chapter 33: Hyperpolarization Methods for MRS

Paul E. Sijens
University of Groningen, University Medical Center Groningen, Groningen, The Netherlands
Chapter 46: Assessing Fatty Liver with MRS

Diana M. Sima
KU Leuven, Leuven, Belgium
iMinds Medical IT, Leuven, Belgium
Chapter 19: Quantifying Spectra in the Time Domain

Jason G. Skinner
University of Nottingham, Nottingham, UK
Chapter 33: Hyperpolarization Methods for MRS

Laura G. Smith
Cedars-Sinai Medical Center, Los Angeles, CA, USA
Chapter 48: Studying Cardiac Lipids in Obese and Diabetic Patients by ^{1}H MRS

Brian J. Soher
Duke University, Durham, NC, USA
Chapter 18: Quantifying Spectra in the Frequency Domain

Renuka Sriram
University of California, San Francisco, CA, USA
Chapter 39: Hyperpolarized ^{13}C MRI and MRS Studies

Bernhard Strasser
Medical University of Vienna, Vienna, Austria
Chapter 8: Chemical Shift Imaging with Phase and Sensitivity Encoding

Lidia S. Szczepaniak
MRS Consulting in Biomedical Research, Albuquerque, NM, USA
Chapter 48: Studying Cardiac Lipids in Obese and Diabetic Patients by ^{1}H MRS

M. Albert Thomas
University of California, Los Angeles, CA, USA
Chapter 30: Two-Dimensional NMR Spectroscopy Plus Spatial Encoding

Jinfeng Tian
University of Minnesota, Minneapolis, MN, USA
Chapter 3: Detection Coils for MRS

Damian J. Tyler
University of Oxford, Oxford, UK
Chapter 49: Cardiac MRS Studies in Rodents and Other Animals

Julien Valette
Commissariat à l'énergie atomique, Fontenay-aux-Roses, France
Chapter 27: Diffusion-Weighted MRS

Sabine Van Huffel
KU Leuven, Leuven, Belgium
iMinds Medical IT, Leuven, Belgium
Chapter 19: Quantifying Spectra in the Time Domain

Peter C.M. van Zijl
The Johns Hopkins University School of Medicine, Baltimore, MD, USA
Kennedy Krieger Institute, Baltimore, MD, USA
Chapter 29: Proton Chemical Exchange Saturation Transfer MRS and MRI

J. Thomas Vaughan *Columbia University, New York, NY, USA*
Chapter 3: Detection Coils for MRS

Daniel B. Vigneron *University of California, San Francisco, CA, USA*
Chapter 39: Hyperpolarized ^{13}C MRI and MRS Studies
Chapter 59: MRS in Prostate Cancer

Robert G. Weiss *Johns Hopkins Hospital, Baltimore, MD, USA*
Chapter 51: MRS in the Failing Heart: From Mice to Humans

Nicholas Whiting *The University of Texas MD Anderson Cancer Center, Houston, TX, USA*
Chapter 33: Hyperpolarization Methods for MRS

Stephen R. Williams *University of Manchester, Manchester, UK*
Chapter 19: Quantifying Spectra in the Time Domain

Yi Zhang *Johns Hopkins University, Baltimore, MD, USA*
Chapter 11: Accelerated Spatially-Encoded MRS of Arbitrarily-Shaped Compartments Using Linear Algebraic Modeling

Series Preface

The *Encyclopedia of Nuclear Magnetic Resonance* was originally published in eight volumes in 1996, in part to celebrate the fiftieth anniversary of the first publications describing the discovery of NMR in January 1946. Volume 1 contained a historical overview and 200 articles by prominent NMR practitioners, whilst the remaining seven volumes consisted of 500 articles on a wide variety of topics in NMR, including MRI. A ninth volume was brought out in 2000 and two "spin-off" volumes incorporating the articles on MRI and MRS (together with some new ones) were published in 2002. In 2006 the decision was taken to publish all the articles electronically with the resulting Encyclopedia becoming available online in 2007. Since then, new articles have been published online every three months and many of the original articles have been updated. To recognize the fact that the *Encyclopedia of Magnetic Resonance* is a true online resource, the website was redesigned and new functionalities added, with a relaunch in January 2013 in a new Volume and Issue format, under the new name *eMagRes*. In December 2012, a new print edition of the *Encyclopedia of NMR* was published in ten volumes (6200 pages). This much needed update of the 1996 edition of the Encyclopedia encompassed the entire field of NMR.

As part of the development of *eMagRes*, a series of printed handbooks on specific areas of magnetic resonance have been introduced. The handbooks are planned in advance by specially-selected editors, and new articles written to give appropriate complete coverage of the subject area. The handbooks are intended to be of value and interest to research students, postdoctoral fellows, and other researchers learning about the topic in question and undertaking relevant experiments, whether in academia or industry. Consult the *eMagRes* website at (www.wileyonlinelibrary.com/ref/eMagRes) for the latest news on magnetic resonance Handbooks.

Roderick E. Wasylishen

March 2016

Preface

The project to create this book began from discussions in 2013, at the ISMRM meeting in Salt Lake City. The drivers were multi-fold. First, world-wide, many key contributors from the hey-days of the 1970s and 80s, when NMR spectroscopy was translated to the in vivo setting, were either approaching retirement or no longer active in the field. Second, the almost half-century of ensuing in vivo MRS activity had culminated, bibliographically, in a diffuse cloud of scientific papers spanning numerous topics in a large diversity of journals, ranging from the pure physical sciences to the pure clinical '-ology' literature. Like trying to identify an elephant by examining one of its limbs, visualizing the entire in vivo MRS animal in to is no longer practical by viewing 1, or even a 1000 scientific papers. Third, there is now an enormous amount of accumulated inside knowledge on what makes a successful in vivo MRS study that has never been published, and is known only to its present and past practitioners. Fourth, many of the published MRS techniques created over the past decades were never actually applied in vivo, due to hardware or software limitations extant at the time of their innovation. Today, advances in MRI technology – for example, coil sensitivity encoding and compressed acquisition techniques – as well as advances in MRS technology such as hyperpolarization, offer far greater flexibility than ever before to implement previously overlooked MRS techniques, and to explore previously inaccessible metabolic pathways with an MRS sensitivity potentially approaching that of positron emission tomography.

The fifth and final impetus is that there are many practical and useful applications of in vivo MRS today. Experimental animal models provide an understanding of healthy physiology, the underlying genetics and the metabolic response to disease and therapy. Human MRS research reveals the metabolism of healthy and disease states and provides a noninvasive metabolic assessment of the efficacy of interventions and life-style changes. Moreover, clinical MRS can provide critical diagnostic information for monitoring and predicting therapeutic response. Yet, in this second decade of the 21st century, there are no up-to-date guides that explain how in vivo MRS can be applied now, what it is useful for, and how the results might be interpreted.

The goal of this book is to steer a pathway through all of the technologies needed to perform MRS in vivo, in practice, today and tomorrow. The book starts with a first half on methodology that spans the basics of NMR, localization methods and MRS parametric measurements. The reader will find multiple choices of spatial localization and signal processing techniques; how to measure metabolite diffusion, pH, chemical reaction rates and magnetization transfer, metabolite and fat concentrations, spin coupling, and multiple quantum transitions among non-proton (^{1}H) nuclei. There are "how to" chapters on performing MRS on non-^{1}H nuclei in vivo, hyperpolarizing nuclei, and the sequences needed to realize the enormous sensitivity gains now available therefrom. The second half of the book is comprised of applications to healthy and diseased tissues from animal models to humans, covering the entire body from head to limb. It starts with cells and tissue extracts, moves to muscle disease and reviews of MRS applications in obesity, diabetes, heart, brain disorders and cancer. This is followed by two reviews on the current state of clinical trials that employ MRS. Finally, we end with appendices that include tabulations of tissue concentrations of NMR nuclei, common metabolites, spectral assignments, frequently used equations, typical spectra, and common artefacts appearing in MRS in vivo.

We are truly honored and humbled to have been able to attract such an outstanding group of world experts on MRS in vivo as contributors to this project. We doubt there are any better or more knowledgeable. We are indebted to them for all the time, effort and first-hand expertise that they have poured into these contributions, and thank them for their perseverance

in putting up with us during the editing process. We believe the sum total is far greater than what either or both of us together could ever have achieved by ourselves, albeit at a small cost to integration, which is perhaps inevitable for an edited volume. Lastly, special thanks go to Jenny Cossham, Elke Morice-Atkinson, and Stacey Woods at John Wiley and Sons, as well as M Vinoth at SPI Global for masterful type-setting and production. We hope you will agree that the result is a real 'Handbook of MRS in vivo' that can be used as a 'hands on guide' to the field.

Paul A. Bottomley
Johns Hopkins University
Baltimore, MD, USA

John R. Griffiths
Cancer Research UK, Cambridge Research Institute
Cambridge, UK

April 2016

Abbreviations and Acronyms

AA	amino acid
AA	ascorbic acid
ACC	anterior cingulate cortex
AcCoA	acetyl-CoA
AcCrn	acetylcarnitine
ACE-I	angiotensin-converting enzyme inhibitor
acetyl-CoA	acetyl coenzyme A
ACS	acetyl-CoA synthetase
ACS	auto-calibration signal
acyl-CoA	acyl-coenzyme A
AD	Alzheimer's disease
ADC	AIDS dementia complex
ADC	analog-to-digital converter
ADC	apparent diffusion coefficient
ADP	adenosine diphosphate
ADR	adriamycin
ADT	androgen deprivation therapy
2AEP	2-aminoethyl phosphonate
AF	annulus fibrosus
AFP	adiabatic full (or fast) passage
AGAT	amidinotransferase
AHP	adiabatic half-passage
AL-COSY	adiabatic localized correlated spectroscopy
ALD	adrenoleukodystrophy
ALS	amyotrophic lateral sclerosis
ALT	alanine transaminase
ALT	aminotransferase
AMARES	advanced method for accurate, robust, and efficient spectral fitting
AMP	adenosine monophosphate
AMPK	5′ adenosine monophosphate-activated protein kinase
3-APP	3-aminopropyl phosphonate
APT	amide proton transfer
APTw	amide proton transfer weighted
AQSES	automated quantification of short echo-time MRS
ARSOS	All Rank Selection Order Statistic-filtering
ARVD	atherosclerotic renovascular disease
ASD	autism spectrum disorder
ASPA	aspartoacylase
ASTM	American Society for Testing and Materials
AT	adipose tissue
ATP	adenosine triphosphate
α-ATP	α adenosine triphosphate
β-ATP	β adenosine triphosphate
γ-ATP	γ adenosine triphosphate
AUC	area under the curve
AUROC	area under the receiver operating characteristic
AV	arterial-venous
AV	automated valves
BASING	band-selective inversion with gradient dephasing
BAT	brown adipose tissue
BATMAN	Bayesian automated metabolite analyzer for NMR spectra
BB-CK	brain creatine kinase
BBB	blood–brain barrier
BCAT	branched chain amino acid transferase
BDPA	1,3-bisdiphenylene-2-phenylallyl
BIR4	B1-independent rotation
BMD	bone mineral density
BMI	body mass index
BNC	Bayonet Neill–Concelman
BOLD	blood oxygen level-dependent
BP	blood pressure
BPH	benign prostatic hyperplasia
BQUANT	Bayesian quantification
BSLIM	B0 compensated Spectral Localization by IMaging
bSSFP	balanced steady-state free precession
BW	bandwidth
CA	contrast agents
CAG	cytosine, adenine, and guanine trinucleotide DNA
CAT	carnitine acetyltransferase
CAV	cardiac allograft vasculopathy
CD	Canavan's disease
CE	Conformité Européenne
CERT	chemical exchange rotation transfer
CEST	chemical exchange saturation transfer
CF	continuous-flow
CFIT	circle fitting
CGL	congenital generalized lipodystrophy
CHD	coronary heart disease
CHESS	chemical shift selective
CHF	congestive heart failure
Cho	choline
ChoSNR	choline signal-to-noise ratio
CK	creatine kinase
CM	cardiomyopathy
CMR	cardiovascular magnetic resonance
CNC	central neurocytomas
CNI	choline-NAA Index
CNR	contrast-to-noise ratio
CNS	central nervous system
Co-EDTA	cobalt-ethylenediaminetetraacetic acid
CoA	coenzyme A
convex-NMF	convex non-negative matrix factorization
COSY	correlation spectroscopy
CP	Carr–Purcell
CP	critical power
cPLA2	cytosolic phospholipase A2
CPMG	Carr–Purcell–Meiboom–Gill
CPS	central peak suppression
CR	complete response
Cr	creatine
Cr+PCr	creatine plus phosphocreatine
CrCEST	creatine CEST

CRI	constant rate infusion
CRLB	Cramer–Rao lower bound
CRO	contract research organization
CRPC	castration-resistant prostate cancer
CS	compressed sensing
CSA	chemical shift anisotropy
CSD	chemical shift displacement
CSDE	chemical shift displacement error
CSE	chemical shift-encoded
CSF	cerebrospinal fluid
CSI	chemical shift imaging
CT	computer tomography
CT/DXA	computer tomography/dual-energy-x-ray absorptiometry
CV	coefficients of variability
c.w.	continuous wave
3D CSI	three-dimensional chemical shift imaging
d-DNP	dissolution dynamic nuclear polarization
DAC	digital-to-analogue converter
DAG	diacylglyceride
DCA	dichloroacetate
DCE	dynamic contrast-enhanced
DCM	dilated cardiomyopathy
DENSE	displacement-encoded imaging with stimulated echoes
DEPT	distortionless enhanced polarization transfer
DFT	discrete Fourier transform
DGE	dynamic glucose enhanced
DHA	dehydroascorbic acid
DHAP	dihydroxyacetone phosphate
DIACEST	diamagnetic CEST
DLB	dementia with Lewy bodies
DLBCL	diffuse large B-cell lymphoma
DMMP	dimethyl methylphosphonate
DMO	5,5-dimethyl-2,4-oxazolidinedione
DMSO	dimethyl sulfoxide
DNP	dynamic nuclear polarization
DPG	2,3-diphosphoglycerate
DPG+Pi	2,3-diphosphoglycerate with inorganic phosphate
DRESS	depth-resolved surface coil spectroscopy
DS	direct water saturation
DSC	dynamic susceptibility contrast
DSCAT	deep subcutaneous adipose tissue
dSRF	discrete spatial response function
DSS	4,4-dimethyl-4-silapentane-1-sulfonic acid
DSS	decision support system
DTI	diffusion tensor imaging
DW	diffusion-weighted
DW-MRI	diffusion-weighted magnetic resonance imaging
DW-MRS	diffusion-weighted magnetic resonance spectroscopy
DWI	diffusion-weighted imaging
EBM	evidence-based medicine
EC	eddy current
ECC	eddy-current correction
ECE	extracapsular extension
ECG	electrocardiogram
EDP	end-diastolic pressure
EEG	electroencephalography
EF	ejection fraction
EHS	Engelbreth–Holm–Swarm
EMCL	extramyocellular lipid
EP-COSI	echo-planar correlated spectroscopic imaging
EP-JRESI	echo-planar J-resolved spectroscopic imaging
EPA	eicosapentaenoic acid
EPI	echo-planar imaging
EPSI	echo-planar spectroscopic imaging
ESR	electron spin resonance
FREO	fractional reorientation
FA	fatty acids
FA	flip-angle
FAS	fatty acid synthase
FAST	four-angle saturation transfer
FBAL	α-fluoro-β-alanine
FDA	Food and Drug Administration
FDG-PET	fluoro-deoxy glucose positron emission tomography
FE	fractional enrichment
FF	fat fraction
FFA	free fatty acid
FFT	fast Fourier transform
FH	fumarate hydratase
FID	free induction decay
FISP	fast imaging with steady precession
FiTAID	fitting tool for arrays of interrelated datasets
FLAIR	fluid attenuated inversion recovery
FLASH	fast low-angle shot
FLEX	frequency-labeled exchange transfer
FM	frequency modulation
fMRI	functional MRI
FOCI	frequency-offset corrected inversion
FOD	fiber orientation dispersion
FOV	field of view
FSC	frequency sweep-cycled
FSE	fast spin-echo
FSL	FMRIB Software Library
FSW	Fourier series window
FT	Fourier transform
FU	fluorouracil
FWHM	full-width at half-maximum height
g-factor	geometry factor
GA3P	glyceraldehyde-3-phosphate
GA3PDH	glyceraldehyde-3-phosphate dehydrogenase
GABA	γ-aminobutyric acid
gag	glycosaminoglycan
GAMMA	general approach to magnetic resonance mathematical analysis
GAPDH	glyceraldehyde-3-phosphate dehydrogenase
GAVA	GAMMA visualization and analysis
GBM	glioblastoma multiforme

GC	gas chromatography
GLC	gas-liquid chromatography
Gln	glutamine
Glu	glutamate
Glx	glutamate plus glutamine
Gly	glycine
GM	gray matter
GNG	gluconeogenesis
GOIA	gradient offset independent adiabaticity
GPC	glycerophosphocholine
GPE	glycerol-phosphoethanolamine
GRAPPA	generalized autocalibrating of partially parallel acquisitions
GRASE	gradient and spin echo
GRE	gradient-echo
GRES	gradient-enhanced shim
GSH	glutathione
GSLIM	generalized spectral localization by imaging
GSSH	glutathione disulfide
GUI	graphical user interface
^{1}H-MRS	proton magnetic resonance spectroscopy
HAMD	Hamilton depression rating scale
HAND	HIV-associated neurocognitive disorders
HCA	contrast agent
HD	Huntington disease
HEP	high-energy phosphate
HEPES	4-(2-hydroxyethyl)-1-piperazineethanesulfonic acid
HER 2	human epidermal growth factor receptor 2
HF	heart failure
HFD	high-fat diet
2-HG	2-hydroxyglutarate
HIF	hypoxia-inducible factor
HIV	human immunodeficiency virus
HLSVD	Hankel–Lanczos singular value decomposition
HMP	hexose monophosphate
HP	hyperpolarized
HR-MAS	high-resolution magic angle spinning
HS	Horska–Spencer
HS1	hyperbolic secant
HSCT	hematopoietic stem cell transplantation
HSQC	heteronuclear single quantum coherence
HSVD	Hankel singular value decomposition
HT	hypertension
IA	iodoacetamide
ICA	independent component analysis
ICM	iterated conditional mode
ICMJE	International Committee of Medical Journal Editors
ICP	intracranial pressure
ICU	intensive care unit
IDC	infiltrating ductal carcinoma
IDEAL	iterative decomposition with echo asymmetry and least-squares estimation
IDH	isocitrate dehydrogenase
IDH1	isocitrate dehydrogenase 1-gene
IDH2	isocitrate dehydrogenase 2-gene
IDL	interactive data language
IEPA	(±)2-imidazole-1-yl-3-ethoxycarbonylpropionic acid
IGT	impaired glucose tolerance
IHL	intrahepatic lipid
IHTG	intrahepatic triglyceride
IM	intramuscular
IMAC	intramyocellular acetylcarnitine
IMCL	intramyocellular lipid
iMQC	intermolecular multiple quantum coherence
IMRT	intensity-modulated radiotherapy
IND	investigational new drug
IP	in-phase
iPLA2	calcium independent phospholipase A2
IR	inversion recovery
IRB	Institutional Review Board
ISIS	image-selected in vivo spectroscopy
ISMRM	International Society for Magnetic Resonance in Medicine
ISUCA	(±)2-(imidazol-1-yl)succinic acid
IT	inversion transfer
IV	intravenous
IVD	intervertebral disc
JB	Jeener–Broekaert
JDE	J-difference editing
jMRUI	Java-based magnetic resonance user interface
JPRESS	J-resolved point-resolved spectroscopy
α-KG	α-ketoglutarate
KIC	ketoisocaproate
KM	Kingsley–Monahan
KO	knockout
L-COSY	localized correlated spectroscopy
L-SECSY	localized spin-echo correlation spectroscopy
LABC	locally advanced breast cancer
LASER	localization by adiabatic selective refocusing
LC	liquid chromatography
LCAD	long-chain acyl-CoA dehydrogenase
LCModel	linear combination of model spectra
LD	Lorentzian difference
LDA	laser diode array
LDA	linear discriminant analysis
LDH	lactate dehydrogenase
LDHA	lactate dehydrogenase A
LDL	low density lipoproteins
LGE	late gadolinium-enhanced
LHRH	luteinizing hormone-releasing hormone
Lip	lipids
LLS	linear least-squares
LogR	logistic regression
LOVARS	length- and offset-varied saturation
LPSVD	linear prediction and singular value decomposition
LS-SVM	least-squared support vector machine

LSEPSI	line-scan echo-planar spectroscopic imaging
LT	lactate threshold
LTM	label transfer module
LV	left ventricular
LVAD	left ventricular-assist device
LVH	left ventricular hypertrophy
LW	line-width
Lys	lysine
MA	magic angle
MAD	metabolic activity decomposition
MAG	monoacetone glucose
MAT	marrow adipose tissue
MCI	mild cognitive impairment
MCT	monocarboxylate transporter
MDD	major depressive disorder
MDH	malate dehydrogenase
ME	multiecho
ME-EPSI	multiecho-based echo-planar spectroscopic imaging
MEA	multiple-event analysis
MEEP-COSI	multiecho echo-planar correlated spectroscopic imaging
MEEP-JRESI	multiecho-based echo-planar J-resolved spectroscopic imaging
MEG	magneto-encephalography
MEGA-PRESS	Mescher–Garwood point resolved spectroscopy
MELAS	mitochondrial encephalomyopathy, lactic acidosis, and stroke-like episodes
MFG	magnetic field gradient
MHD	magnetohydrodynamic
MHRA	Medicine and Healthcare Products Regulatory Agency
mI	myo-Inositol
MI	myocardial infarction
Mi-CK	mitochondrial creatine kinase
MIDAS	metabolite imaging and analysis system
MM	macromolecule
mM	millimolar
MM	mobile macromolecule
MMMF	MRS-based measures of mitochondrial function
MODY-2	mature-onset diabetes of young-2
MOI	moiety of interest
MP-FIR	maximum phase finite impulse response
mp-MRI	multiparametric MRI
MPA	methylphosphonic acid
MPDA	methylenediphosphonic acid
MQF	multiple-quantum-filtered
MR	magnetic resonance
MRI	magnetic resonance imaging
mRNA	messenger-RNA
MRS	magnetic resonance spectroscopy
MRSI	magnetic resonance spectroscopic imaging
MRSI	multidimensional/multivoxel MRS imaging
MRST	magnetic resonance saturation transfer
MS	mass spectrometry
MS	multiple sclerosis
MT	magnetization transfer
MTC	magnetization transfer contrast
MTL	medial temporal lobe
MTR	magnetization transfer ratio
MUFA	monounsaturated fatty acid
MV	manual valves
MV	multivolume
MVS	multivoxel spectroscopy
MyD	myotonic dystrophy
NAA	N-acetylaspartate
NAAG	N-acetylaspartylglutamate
NACT	neoadjuvant chemotherapy
NADH	nicotinamide adenine dinucleotide reduced form
NAFLD	nonalcoholic fatty liver disease
NASH	nonalcoholic steatohepatitis
NAV	number of averages
NCR	not complete response
NF	noise figure
NFT	neurofibrillary tangles
NHL	non-Hodgkin's lymphoma
NIH	National Institutes of Health
NIRS	near infrared spectroscopy
NIWVF	normalized intensity-weighted variance filter
NMF	non-negative matrix factorization
NMR-SCOPE	NMR spectra calculation using OPErators
NOBLE	narrow-band localized excitation
NOE	nuclear Overhauser effect
NOESY	nuclear Overhauser effect spectroscopy
NOM	numerically optimized modulation
NOMAR	normalized magnetization transfer ratio
NP	nucleus pulposus
NSA	number of signal averages
NTP	nucleoside triphosphate
nuFFT	nonuniform fast Fourier transform
NUS	nonuniform undersampling
NWS	nonwater-suppressed
NYHA	New York Heart Association
OAA	oxaloacetate
OD	outer diameter
OIA	offset-independent adiabaticity
OP	opposed-phase
OPARACHEE	on-resonance paramagnetic chemical exchange effects
OPLS-DA	orthogonal partial least squares-discriminant analysis
OSA	obstructive sleep apnea
OVS	outer-volume suppressed
OXPHOS	oxidative phosphorylation
P/O	phosphate/oxygen
PA	phased-array
PACE	prospective acquisition correction sequence
PACS	picture archiving and communications system

PARACEST	paramagnetic chemical exchange saturation transfer
PARP	poly(ADP)-ribose polymerase
PB	phenylbutyrate
PC	pyruvate carboxylase
PCA	principal component analysis
PCC	posterior cingulate cortex
pCEST	positive CEST
PCho	phosphocholine
PCr	phosphocreatine
PDE	phosphodiesters
pdf	probability density function
PDFF	proton density fat fraction
PDH	pyruvate dehydrogenase
PE	phosphoethanolamine
PEG	polyethylene glycol
PEGS	phase-encoding gradient step
PEMT	phosphatidylethanolamine N-methyltransferase
PEP	phosphoenolpyruvate
PEPCK	phosphoenolpyruvate carboxykinase
PEPSI	proton echo-planar spectroscopic imaging
PET	positron emission tomography
PEtn	phosphoethanolamine
PFC	perfluorinated compound
PFCE	perfluoro-15-crown-5-ether
PG	pressure gauges
PG	proteoglycan
PGC-1α	peroxisome proliferator-activated receptor-γ coactivator-1α
PGK	phosphoglycerate kinase
PGSE	pulsed gradient spin-echo
Phe	phenylalanine
pHi	Intracellular pH
PHIP	para-hydrogen induced polarization
Pi	inorganic phosphate
PIN	positively doped, intrinsic and negatively doped semiconductors
PK	pyruvate kinase
PLA2	phospholipase A2
PLS	partial least square
PLS–DA	partial least squares–discriminant analysis
PME	phosphomonoester
PNCT	phosphonitrilic chloride trimer
PNET	primitive neuroectodermal tumor
PO2	pressure of oxygen
PPA	phenylphosphonic acid
PPAR-γ	peroxisome proliferator-activated receptor-γ
ppm	parts per million
PPV	positive predictive value
PR	pattern recognition
PRESS	point-resolved spectroscopy
ProFit	prior knowledge fitting
PS	partial saturation
PS	partial separability
PSA	prostate specific antigen
PSer	phsophatidylserine
PSF	point spread function
PTR	proton transfer ratio
PUFA	polyunsaturated fatty acid
QA	quality assessment
QC	quality control
QUEST	quantification based on quantum estimation
RARE	rapid acquisition with relaxation enhancement
RBC	red blood cell
REO	reorientation
RF	radiofrequency
RFID	radiofrequency identification
RFZ	rotating frame zeugmatography
RMS	root-mean-square
RMSE	root-mean-square error
rNOE	NOE-relayed
ROC	receiver operating characteristic
ROI	region-of-interest
ROS	reactive oxygen species
RPP	rate-pressure product
RR	respiratory rate
RT	room-temperature
SABRE	signal amplification by reversible exchange
SAFARI	saturation with frequency alternating radiofrequency irradiation
SAR	specific absorption rate
SB	sine-bell
SC	subcutaneous
SD	standard deviation
SE	spin echo
SE	standard error
SE-EPI	single-shot, echo-planar imaging
SENSE	sensitivity encoding
SEOP	spin-exchange optical pumping
SF	stopped-flow
SG	specific gravity
SI	spectroscopic imaging
SIACI	superselective intraarterial cerebral infusion
SL	slice thickness
SLAM	spectroscopy with linear algebraic modeling
sLASER	semi-localization by adiabatic selective refocusing
SLIM	spectral localization by imaging
SLOOP	spatial localization with optimum point-spread function
SLR	Shinnar–Le Roux
SNR	signal-to-noise ratio
SOP	standard operating procedure
SoS	sum-of-the-square
SPAIR	spectral attenuated inversion recovery
SPECIAL	spin-echo full-intensity acquired localized spectroscopy
SPECT	single photon emission computed tomography
SPICE	spectroscopic imaging by exploiting spatiospectral correlation
SPIR	spectral presaturation with inversion recovery
sPLA2	secretory phospholipase A2

SPLASH	spectral localization achieved by sensitivity heterogeneity
SPM	semiparametric modeling
SPSP	spectral-spatial
SQ	single quantum
SQC	single quantum coherence
SR	sarcoplasmic reticulum
SR	saturation recovery
SRF	spatial response function
SS	steady state
SSCAT	superficial subcutaneous adipose tissue
SSFP	steady-state free precession
SSRI	serotonin reuptake inhibitor
ST	saturation transfer
starSLIM	static and radiofrequency-compensated spectral localization by imaging
STE	stimulated echo
STEAM	stimulated echo acquisition mode
SURE-SENSE	super-resolution sensitivity encoding
SV	single voxel
SVD	singular value decomposition
SVM	support vector machine
SVS	single-voxel spectroscopy
T/R	transmit/receive
T1D	type 1 diabetes
T2D	type 2 diabetes
T2W	T2-weighted
TAC	thoracic aortic constriction
TARQUIN	totally automatic robust quantitation in NMR
TBI	traumatic brain injury
TCA	tricarboxylic acid
tCho	total choline
tCr	total creatines
TDFDfit	time-domain and frequency-domain fitting
TE	echo time
TEM	transverse electromagnetic
TG	triglyceride
TI	inversion time
TIM	total imaging matrix
TKX	telazol, ketamine, xylazine
TM	mixing time
TMA	trimethylammonium
TMS	tetramethylsilane
TMZ	trimetazidine
TOCSY	total-correlated spectroscopy
TPP	tetraphenylporphyrin
TPPhos	triphenylphosphite
TQF	triple quantum filtering
TR	repetition time
TRAMP	transgenic adenocarcinoma of mouse prostate
TRE-CEST	transfer rate-edited CEST
TRIM	time-domain removal of irrelevant magnetization
TRiST	triple repetition time saturation transfer
trueFISP	true fast imaging and steady-state precession
TRUS	transrectal ultrasound
TS	transversal system
TSC	tissue slice culture
TSE	turbo spin-echo
TSP	trimethylsilyl propanoic
TSVD	truncated singular value decomposition
TTF	time to treatment failure
TV	total variation
TwiST	two-repetition time saturation transfer
UFA	unsaturated fatty acids
UI	user interface
UISNR	ultimate intrinsic signal-to-noise ratio
UNOS	United Network for Organ Sharing
UTE	ultrashort echo-time
VaD	vascular dementia
VAPOR	variable pulse power and optimized relaxation delay
VARPRO	variable projection method
VAT	visceral adipose tissue
VDMP	variable-delay multipulse
VERSE	variable rate selective excitation
VeSPA	versatile simulation, pulses and analysis
VFA	variable flip angle
VLCD	very low-calorie diet
VOI	voxel-of-interest
VSS	very selective saturation
WASSR	water saturation shift referencing
WAT	white adipose tissue
WBNAA	whole brain N-acetyl aspartate
WET	water suppression enhanced through T_1 effects
WEX	water exchange
WHO	World Health Organization
WM	white matter
WS	water-suppressed
WT	wild-type
X-ALD	X-linked adrenoleukodystrophy
XO	xanthine oxidase
ZAPI	Z-spectroscopy with alternating phase irradiation
ZDF	Zucker diabetic fatty

PART A
Methodology

Basics

Chapter 1
Basics of NMR

Paul A. Bottomley

Johns Hopkins University, Baltimore, MD, USA

1.1 NUCLEAR MAGNETIC RESONANCE

1.1.1 Eligible Nuclei

The NMR phenomenon is exhibited by atomic nuclei with an odd number of either protons or neutrons. This includes, for example, neutrons, protons or hydrogen nuclei (^{1}H), deuterons (^{2}H), carbon-13 (^{13}C), nitrogen-14 and -15, and oxygen-17 (O^{17}), but not unfortunately the more abundant ^{12}C or ^{16}O (Table 1.1). The NMR nuclei possess quantum mechanical spin angular momentum that endows them with a tiny magnetic field or dipole moment whose strength is characterized by a magnetic moment, μ, that is unique to each nucleus. The spin angular momentum has a quantum number, I, that can have values of $^{1}/_{2}$, 1, 3/2, 2, 5/2, etc., depending on the nucleus. When placed in an applied magnetic field, $\mathbf{B_0}$, a weak torque is exerted on the nuclear magnetic moment, which tends to align it, but because the spin is quantized, only certain orientations of the moment with $\mathbf{B_0}$ are allowed. The number of available orientations is $2(I+1)$, and they are symmetrically oriented about the direction of $\mathbf{B_0}$, which by convention is always chosen as the z-axis of a Cartesian coordinate system (Figure 1.1).

Because each allowed orientation of the nuclear magnet is more or less favorably disposed relative to $\mathbf{B_0}$, each is associated with a different energy level. The lowest energy levels correspond to orientations that are most closely aligned with $\mathbf{B_0}$, and the highest energy states are aligned against $\mathbf{B_0}$. Transitions between energy levels correspond to jumps between the allowed orientations. These require the emission or absorption of energy quanta in accordance with the Planck relation for the energy difference, $E = h\nu_0$, where h is Planck's constant ($=6.626\times10^{-34}$ Js) and we introduce ν_0 as the NMR frequency (Figure 1.1). This is the frequency at which nuclear magnets rotate or 'precess'† about $\mathbf{B_0}$ at its allowed orientation with the z-axis. In addition to being proportional to ν_0, the energy difference, whose existence is due to the presence of both the nuclear magnet and $\mathbf{B_0}$, is in fact proportional to the magnitude of $\mathbf{B_0}$, denoted B_0. These two proportionalities are combined in the Larmor equation:

$$\omega_0 = \gamma B_0 \tag{1.1}$$

†Quotation marks define common NMR terms at first usage, throughout.

Handbook of Magnetic Resonance Spectroscopy In Vivo: MRS Theory, Practice and Applications.
Edited by Paul A. Bottomley and John R. Griffiths

ISBN: 978-1-118-99766-6
Also published in eMagRes (online edition)
DOI: 10.1002/9780470034590.emrstm1485

Table 1.1. NMR properties and relative signal-to-noise ratios (SNRs) in muscle tissue at constant B_0 for some common elements[a]

Nucleus	Spin, I	Isotopic abundance (%)	ν_0 (MHz) at $B_0 = 1$ T	SNR/mole of NMR nucleus[a] vs ^{1}H	Elemental concentration in muscle[b] (mmol g^{-1} wet wt)	Relative SNR vs ^{1}H in muscle[c]
^{1}H	1/2	99.98	42.577	1	99.21	1
^{2}H	1	0.0156	6.536	0.0628	99.21	9.81×10^{-6}
^{13}C	1/2	1.108	10.705	0.0632	8.920	6.3×10^{-5}
^{14}N	1	99.64	3.076	0.0139	1.963	2.75×10^{-4}
^{17}O	5/2	0.037	5.772	0.2144	46.88	3.75×10^{-5}
^{31}P	1/2	100	17.235	0.1639	0.058	9.52×10^{-5}

[a]Assumes SNR varies linearly with B_0 (SNR$\propto\gamma^2 I[I+1]$), that nuclei are 100% NMR visible and monochromatic, no polarization enhancement, equilibrium, and a noiseless receiver with the same bandwidth (BW; see Section 1.5.3.1). Note that SNR differs from 'NMR sensitivity' ($\propto\gamma^3\ I[I+1]$) reported variously. Relative SNRs are consistent with relative magnetizations at 1 T in Ref. 1 (p. 309), and equation (1.30) in the Section 1.5.2 divided by $\nu_n \propto \omega_0$, to account for frequency-dependent sample noise.
[b]Assumes elemental contents and wet weights for human tissue in Ref. 2.
[c]SNR/mol of nucleus scaled by isotopic abundance and elemental concentration in muscle.

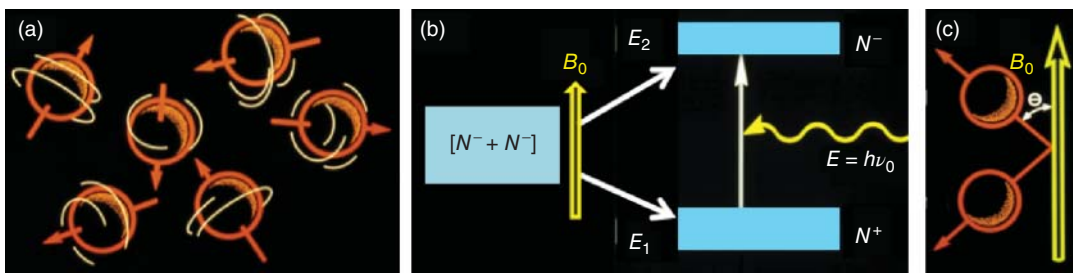

Figure 1.1. Exposing a population of nuclear spin magnets (a) to a magnetic field $\mathbf{B_0}$ causes the nuclear spin energy to split into two or more levels, E_1 E_2, etc., separated by $E \propto B_0$ (b). The levels are populated according to Maxwell–Boltzmann statistics and the available thermal energy of the lattice. There is a slight excess (N^+/N^-) in the lowest energy state because more nuclei are aligned with $\mathbf{B_0}$ than against it. The orientations of the nuclei relative to $\mathbf{B_0}$ are quantized into $2(I+1) = 2$ levels for spin $I = 1/2$ nuclei such as ^{1}H or ^{31}P (c). Transitions between energy levels and orientations result in emission or absorption of energy at the resonant frequency, ν_0, with a characteristic transition rate $1/T_1$. The widths of E_1 and E_2 are broadened by variations in the local field characterized by rates $1/T_2$ or $1/T_2{}^*$

where $\omega_0 = 2\pi\nu_0$ is the angular NMR frequency (in rad s^{-1}) and γ the proportionality constant called the 'gyromagnetic' ratio. Equation (1.1) is the key to NMR, nuclear magnetic resonance spectroscopy (MRS), MRI, and all of the spatial localization methods used in these endeavors. The gyromagnetic ratio is different for each NMR isotope, and for practical B_0 values of 0.1–10 tesla (T), ν_0 falls in the radio frequency (RF) band: about 0.5–450 MHz. These two facts allow, in principle, each nucleus to be tuned in for NMR, like tuning a radio station on the FM (frequency modulation) band.

However, NMR is not performed on a single nuclear spin, but typically on vast numbers of them. The nuclear spin density for a pure substance with formula weight FW is $[n_m A_0/\text{FW}]$ per gram, where A_0 is Avogadro's number (6.02×10^{23}) and n_m the number of NMR nuclei on each molecule of the substance. For example, a 1 ml or 1 g sample of water with FW = 18 and $n_m = 2$ hydrogen nuclei contains

about $N_{ml} = 6.7 \times 10^{22}$ nuclei that are eligible for ^{1}H NMR. Biological tissue is about two-thirds water but the other one-third also contains ^{1}H at a comparable density, so there are about 6×10^{22} ^{1}H nuclei in 1 g of tissue as well.

It is fortunate from a safety perspective that when all these nuclei in a living sample are placed in a $\mathbf{B_0}$ field at a temperature of $T = 37\,^\circ$C, they do not all suddenly align, lest there be some dire physiological response. In fact, the thermal motion present in the nuclear spin environment or 'lattice' is much greater than the alignment torque. The $2(I+1)$ energy levels arising from the combined effect of $\mathbf{B_0}$ and the quantized spin angular momentum are populated by all the nuclei in accordance with Maxwell–Boltzmann statistics. For a spin $I = 1/2$ nucleus such as ^{1}H with two orientations (Figure 1.1c), the excess of spins aligned with a $\mathbf{B_0}$ of 1 tesla (T) instead of against it is only

$$<N^+/N^-> = \exp(E/KT) = \exp(h\nu_0/KT) \approx \text{seven in a million}$$

where K is Boltzmann's constant and T is in Kelvin. Nevertheless, this leaves a total excess of $\mathbf{B_0}$-aligned nuclear magnets in the 1 ml water of $7N_{ml}//10^6 \sim 5 \times 10^{17}$.

1.1.2 Exciting Resonance

The collective effect of this many nuclei aligning with $\mathbf{B_0}$ is to create a weak net or 'bulk nuclear magnetization', $\mathbf{M}$, proportional to $\mathbf{B_0}$ with magnitude $\mathrm{M} = \{N_{ml} \cdot \mu \cdot <N^+/N^->\}$ per milliliter. At equilibrium, $\mathbf{M}$ is aligned with $\mathbf{B_0}$ and denoted $\mathrm{M}_0\ \hat{\mathbf{z}}$, where $\hat{\mathbf{z}}$ is a unit vector in the z-direction (Figure 1.2a). Because the spins are precessing with random coherence and jostled by thermal motion, there is no net 'transverse magnetization', $\mathbf{M_{xy}}$, in the x–y plane in which the nuclear spins precess. This means that no actual resonance is observed – just the slight increase in sample magnetization. To see a NMR, $\mathbf{M}$ must be perturbed away from equilibrium. This is equivalent to requiring

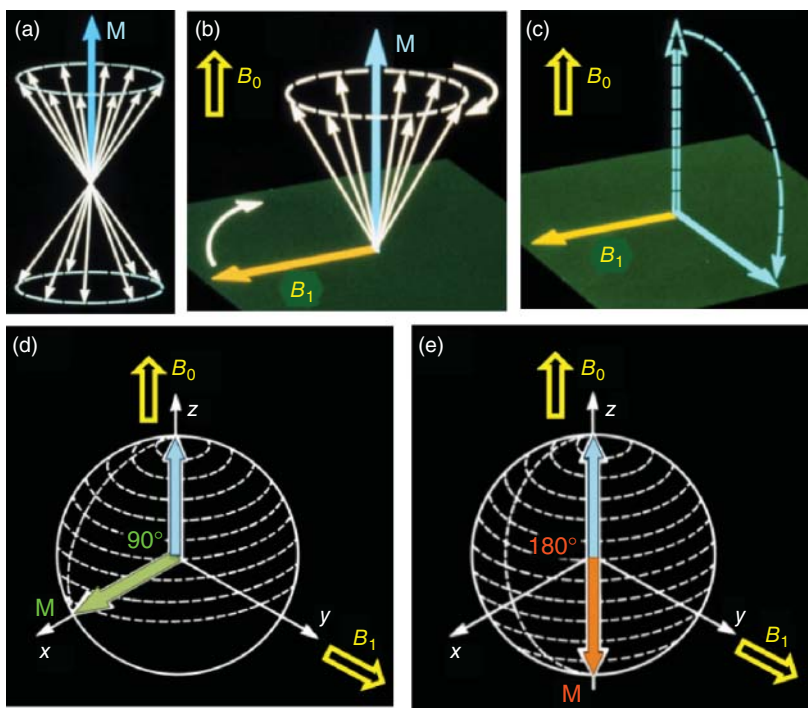

Figure 1.2. At equilibrium, nuclei precessing about $\mathbf{B_0}$ produce a net longitudinal magnetization, $\mathbf{M}$, aligned with $\mathbf{B_0}$, but they are out of phase so there is no net transverse magnetization (a). Application of a transverse RF field, $\mathbf{B_1}$, tuned to ν_o rotates $\mathbf{M}$ into the transverse plane (b and c). The trajectory of $\mathbf{M}$ is a spiral rotating about $\mathbf{B_0}$ at ν_o (d and e). If $\mathbf{B_1}$ is turned off when $\mathbf{M}$ crosses the x–y plane, the B_1-pulse is called a 90° pulse (d). If it is turned off when $\mathbf{M}$ is inverted, it is a 180° pulse (e)

that the population distribution of the nuclear energy levels be disrupted, after which **M** might be observed as it returns or 'relaxes' back to $\mathbf{B_0}$ and the population distribution returns to thermal equilibrium. To perturb **M** away from $\mathbf{B_0}$ would normally require exerting a torque on **M** of comparable magnitude to that provided by $\mathbf{B_0}$ in say a transverse or minus-$\mathbf{B_0}$ direction, which would be impractical. Instead, a much smaller magnetic field, $\mathbf{B_1}$, can be used to tip **M** if it is precisely tuned to the NMR frequency, ν_0, satisfying equation (1.1) (Figure 1.2b). This is analogous to a pendulum whose swing can be increased to extreme levels with the slightest force applied at the pendulum's resonant frequency, transverse to the pendulum's axis. Similarly, $\mathbf{B_1}$ must be applied in the x–y plane because applying it in the z-direction will not perturb **M** away from $\mathbf{B_0}$.

The first NMR on condensed matter[3,4] and indeed the first MRI[5] were performed by 'continuous wave (c.w.)' NMR wherein the B_0 field was swept over a tiny range about the value satisfying equation (1.1), while a transverse $\mathbf{B_1}$ was applied continuously at the NMR frequency, ν_0: sweeping B_0 was less technically difficult[3] than sweeping the frequency, ν. At resonance, transitions between energy levels are induced, resulting in a net absorption of energy and the first 'NMR spectrum' (Figure 1.3)[4] or plot of the NMR signal as a function of frequency or equivalently – in light of equation (1.1) – field strength.

The c.w. method generated the spectrum one point at a time, and is now passé. It was replaced by much more efficient pulsed NMR methods that were introduced a few years after c.w. NMR.[6] Pulsed NMR can excite and measure a whole spectrum (or spatial MRI projection of a sample) at once. In pulsed NMR, $\mathbf{B_1}$ is applied as an RF pulse tuned to ν_0. Its amplitude, although tiny (typically 5–100 μT) compared to B_0, nudges **M** away from the z-axis down into the x–y plane over many cycles, by virtue of being resonant (Figure 1.2c). The trajectory of **M** is actually a spiral at the resonant frequency (Figure 1.2d): a 20 μs pulse applied at 42.577 MHz for ^{1}H at $B_0 = 1$ T, for example, would undergo $(20 \times 42.577) = 852$ revolutions. The trick is to turn off $\mathbf{B_1}$ when **M** is precisely at some desirable point in its 3D vector space.

If you start with M_0 aligned with the $+z$-axis and turn off B_1 exactly when it intersects the x–y plane, you have rotated **M** by a 'flip-angle (FA)' of $\alpha = 90°$ (Figure 1.2d). At this time, you have the maximum nuclear magnetization vector precessing, rotating coherently, or 'resonating' at ν_0 in the transverse plane.

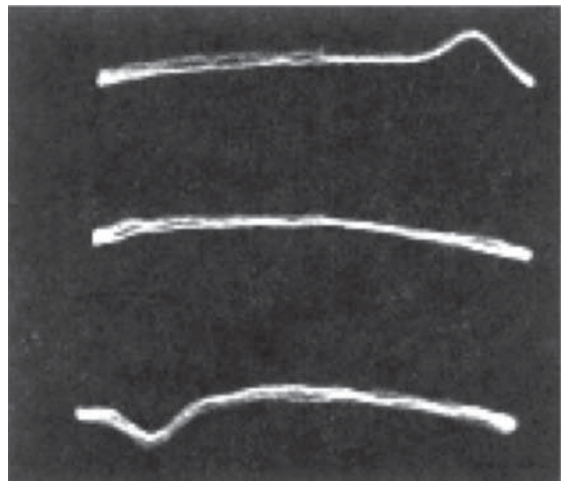

Figure 1.3. Oscilloscope trace depicting one of the first NMR spectra – from water.[4] The field is cycled at 60 Hz through the resonance at $B_0 = 0.183$ T with the field slightly higher (top) and lower (bottom) than the resonance. In the central trace, the field sweep was centered on the resonance, saturating it. (Reprinted figure with permission from F. Bloch, W. W. Hansen, and M. Packard, Phys. Rev., 69, 127, 1946. Copyright 1946 by the American Physical Society. DOI: http://dx.doi.org/10.1103/PhysRev.70.474)

With B_1 now off, the rotating magnet can induce a voltage or 'NMR signal' in a pick-up coil that is tuned to ν_0 and is sensitive to the transverse field (Figure 1.4a). The pulse whose duration and amplitude first generate the maximum NMR signal following a period of equilibration is deemed to be a '90° or π/2 NMR pulse'.

If B_1 is left on after M_0 passes through 90°, the magnetization will keep going until it is fully inverted (Figure 1.2e). At this point, the transverse magnetization is minimal, as is the NMR signal induced in the coil. This defines a '180°' or 'π NMR pulse'. If B_1 has the same amplitude profile as the 90° pulse, the 180° pulse is exactly twice the duration of the 90° pulse. While 90° and 180° pulses are often applied sequentially as 'pulse sequences' in NMR and MRI, other arbitrary FAs are certainly allowed and used. As minima can be easier to detect than maxima, determining the 180° pulse length from the first signal minimum following a maximum is often the easier way to calibrate FA in practice. The relation between an FA of α radians B_1 (Tesla) and pulse length τ (s) derives directly from equation (1.1) with B_1 substituted for B_0:

$$\alpha = \gamma B_1 \tau \tag{1.2}$$

This reflects the fact that in a frame-of-reference rotating at exactly the NMR frequency about the z-axis, the spiral trajectory of **M** during the pulse vanishes, and the effective field is equal to B_1. In this 'rotating frame of reference', B_1 appears static and directed along say the x-axis of the rotating transverse plane. Thus, when B_1 is turned on, M will precess or 'nutate' directly about B_1, traversing an arc of α (Figure 1.2c). The transverse component is simply $M_{xy} = M \sin \alpha$.

The pick-up coil that detects the RF voltage induced by M_{xy} can be the same one used to generate B_1, or a separate tuned NMR receiver coil (see Chapter 3). The coil is connected to an NMR spectrometer or MRI scanner. There, the tiny NMR signal is first amplified, and then 'demodulated' by removing the ν_0 component (see Chapter 2). This brings the NMR signal essentially into an audio frequency range for display and processing. Such processing is analogous to the demodulation that an FM radio performs on an 88.1 MHz radio signal from Baltimore station WYPR say to enable us to listen to the sound. On an NMR radio tuned to ν_0, we listen to the rotating frame directly.

1.2 RELAXATION

1.2.1 T_1 and T_2

The NMR signal excited by the $\alpha \neq \pi$ NMR pulse is called a 'free induction decay' or 'FID' (Figure 1.4c). The decay in M_{xy} is due to two distinct processes. First, M_{xy} decays owing to the dephasing of nuclear spins in the sample owing to tiny differences in the local B_0 magnetic field, which affect the local NMR frequency via equation (1.1). This dephasing can have both intrinsic and external or instrumental origins, which are respectively irreversible or reversible using NMR methods described in the following text. Generally, the FID is assumed to be a mixture of both components, and the decay is deemed to have a time constant 'T_2* (T_2-star)', which is assumed to be exponential whether it is or not. The most common instrumental contributor to T_2* is inhomogeneity in B_0 due to gradients, metal, eddy currents, etc. The irreversible part of the decay is characterized by a time constant 'T_2' (no asterisk), called the 'transverse relaxation time' or the 'spin–spin relaxation time'. T_2 decay results from irreversible dephasing owing to the presence of local gradients at the molecular level arising from both static and mobile molecular-level sources.[6–9]

Second, if the M_{xy} dephasing processes do not dominate, **M** must eventually relax back to the z-axis to align with $\mathbf{B_0}$ (Figure 1.1b). The growth in the z-magnetization, M_z, is characterized by a time constant 'T_1', called the 'longitudinal' or 'spin–lattice relaxation time'. T_1 relaxation is facilitated by the presence of variations in the local magnetic field at ν_0 and $2\nu_0$, such as those caused by inter- and intramolecular motions of nearby nuclear dipoles. Just like B_1, these local field fluctuations at the NMR frequency facilitate the transitions between energy levels that are necessary to restore the equilibrium state.[7,8]

Expressions for T_1 and T_2 due to dipole–dipole interactions are[8]:

$$\frac{1}{T_1} = \frac{3}{2}\gamma^4 \bar{h}^2 I(I+1)[J_1(\nu_0) + J_2(2\nu_0)] \tag{1.3}$$

and

$$\frac{1}{T_2} = \gamma^4 \bar{h}^2 I(I+1)\left[\frac{3}{8}J_0(0) + \frac{15}{4}J_1(\nu_0) + \frac{3}{8}J_2(2\nu_0)\right] \tag{1.4}$$

where $\bar{h} = h/2\pi$ and the J's are the spectral density of motion calculated at ν_0, $2\nu_0$, and static ($\nu = 0$) frequencies. The $2\nu_0$ term arises because motion at twice the frequency can reverse the sense of a spin going

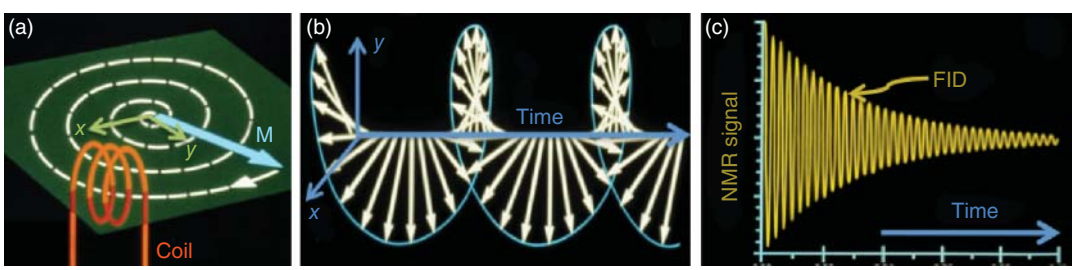

Figure 1.4. The magnetization rotating in the x–y plane generates an RF voltage in a tuned pick-up coil sensitive to the transverse field (a). The amplitude of the rotating magnetization (b), and the induced voltage (c) decay with a time constant T_2 or T_2*, producing a free induction decay (FID)

the wrong way, inducing a transition.[7] Equation (1.3) was used to calculate a reasonably accurate T_1 for ^{1}H nuclei (protons) in pure water, based on J's deduced assuming only an isotropic diffusion motion for the protons.[7] Nevertheless, models describing the relaxation times of nuclei in biological tissue remain at best empirical.[9,10]

The T_1 and T_2 values depend on the molecular-level environment, and typically vary with ν_0, temperature, the molecule, the location of the nuclei on the molecule, and in biological applications, the tissue it is in.[9,10] In biological systems ^{1}H, T_1s typically range from 0.1 to 2 s. T_2s are shorter at about 10–300 ms, owing to the added effects of the low-frequency and static processes (the J_0 term), which ensure that T_2 is always less than T_1. Differences between the relaxation times of ^{1}H in water in biological tissue are responsible for image contrast in MRI, and its utility in medicine.[9,10] *The importance of relaxation times to MRI contrast is truly immense, but of even greater importance to the field of NMR as a whole is that they endow the NMR spin system with a memory that lasts several T_1s. Without such memory, stringing together, sequentially, all of the crafty space- and time-encoding methods that make possible just about everything NMR, MRI, and MRS does would not work.*

1.2.2 The Bloch Equations

Generally, an NMR experiment will be comprised of one or more excitations and periods of detection. The resulting magnetization is described by the 'Bloch equations'[11]:

$$\begin{aligned}\frac{\mathrm{d}M_x(t)}{\mathrm{d}t} &= \gamma(M_y(t)B_z(t) - M_z(t)B_y(t)) - \frac{M_x(t)}{T_2}\\ \frac{\mathrm{d}M_y(t)}{\mathrm{d}t} &= \gamma(M_z(t)B_x(t) - M_x(t)B_z(t)) - \frac{M_y(t)}{T_2}\\ \frac{\mathrm{d}M_z(t)}{\mathrm{d}t} &= \gamma(M_x(t)B_y(t) - M_y(t)B_x(t)) - \frac{M_z(t) - M_0}{T_1}\end{aligned} \tag{1.5}$$

The first bracketed terms on the right describe in component form, the nutation of $\mathbf{M}$ from the torque imparted by the $\mathbf{B}$ field during excitation. This derives from the vector cross product, $\mathrm{d}\mathbf{M}(t)/\mathrm{d}t = \gamma\mathbf{M}(t) \times \mathbf{B}(t)$. The subtracted quotients describe the decay in the transverse magnetization at a rate $1/T_2$, and the growth in longitudinal magnetization at $1/T_1$. These equations permit numerical simulation of any NMR experiment by breaking the differential terms on the left into tiny steps, ΔM_x, Δt, etc. Usually, the pulse length $\tau \ll T_1$, so the T_1 and T_2 terms can be neglected during pulses while the $\mathbf{B_1}$ terms vanish between pulses.

1.2.2.1 Circular Polarization of B_1

Importantly, the nuclei only rotate or precess in one direction relative to $\mathbf{B_0}$ or $\mathbf{B_1}$ (Figures 1.2 and 1.4). This means that the RF signal that is emitted or absorbed during NMR is circularly polarized, which has two practical consequences. First, only the circularly polarized component of $\mathbf{B_1}$ rotating in the same direction as the spins can excite NMR. Before the mid-1980s, $\mathbf{B_1}$ was generated in a single transverse direction, the x-axis in the laboratory frame-of-reference say, by applying a sinusoidal current, $I\cos\omega t$, to a loop coil (such as a solenoid, a 'saddle', a 'figure-8', or surface coils) in a configuration that is now referred to as 'linear excitation'. The sinusoidal current only produces a sinusoidal B_1 which is not circularly polarized. This nevertheless works because the linear field can be decomposed into two counter-rotating fields:

$$\begin{aligned}B_1\hat{\mathbf{x}} = B_{10}\cos\omega t \cdot \hat{\mathbf{x}} &= (B_{10}/2)(\cos\omega t \cdot \hat{\mathbf{x}} + \sin\omega t \cdot \hat{\mathbf{y}})\\ &\quad + (B_{10}/2)(\cos\omega t \cdot \hat{\mathbf{x}} - \sin\omega t \cdot \hat{\mathbf{y}})\end{aligned} \tag{1.6}$$

where $\hat{\mathbf{x}}$ and $\hat{\mathbf{y}}$ are unit vectors in the x- and y-directions and B_{10} is the amplitude of $\mathbf{B_1}$. The cost of creating this virtual circularly polarized field is that only half the B_1 is being used to excite NMR: the other half is wasted on the counter-rotating component. Given that $B_1 \propto$ current, I, in the excitation coil and power $\propto I^2$, the difference in the peak RF power required to produce B_{10} vs $B_{10}/2$ is a factor of 4.

By the mid-1980s, linear excitation for head and whole body NMR was replaced by circularly polarized excitation, primarily as a consequence of the invention of the 'birdcage' coil for MRI (see Chapter 3).[12] Circular polarization is achieved by applying two sinusoidal waves, 90° out of phase, to two 'quadrature' ports that are both physically and electromagnetically displaced by 90° (or a 1/4-wavelength) around the coil. The excitation field is then just

$$\mathbf{B_1} = B_{10}(\cos\omega t \cdot \hat{\mathbf{x}} + \sin\omega t \cdot \hat{\mathbf{y}}) \tag{1.7}$$

This configuration cuts the peak power requirement fourfold. However, the total average power input and the total power deposited in the sample are only halved because power must now be applied to two ports instead of the one.[12] The circular polarization of the NMR signal can be verified by interchanging the two

quadrature inputs: no NMR occurs with the inputs backwards, except at locations where the circular polarization is imperfect.[12]

The second consequence of the rotating field relates to the 'signal-to-noise ratio' (SNR) of the NMR signal.[13,14] Here the 'signal' is the NMR voltage induced in the detector coil. The 'noise' voltage, v_n, is measured as the 'root-mean-square' (RMS) of what is left over when the NMR signal has decayed away. Even though the NMR signal rotates in only one direction, a linear detector is sensitive to both counter-rotating components and therefore detects the noise voltage from both components, $v_{n0°}$ and $v_{n90°}$. Because $v_{n0°}$ and $v_{n90°}$ are uncorrelated, the RMS noise adds as $\sqrt{(v_{n0°}{}^2 + v_{n90°}{}^2)} = v_n\sqrt{2} \approx 1.4v_n$. Thus, using a linear detector carries a 40% SNR penalty compared to a true quadrature detector sensitive only to the rotating component.[14]

1.2.3 Measuring Relaxation

1.2.3.1 T_1 and Partial Saturation

The simplest NMR pulse sequence just involves applying an $\alpha°$ FA pulse of duration $\tau \ll T_1$, and acquiring the excited signal. Some 'repetition period', TR, is waited before the $\alpha°$ pulse is applied again. After the first pulse, M_0 is rotated $\alpha°$ into the x–y plane and begins to precess at ω_0 about the z-axis (Figure 1.5a). According to the solution of equation (1.5) with the pulse off, the M_z component starts with magnitude $M_0 \cos\alpha$ and begins to grow back to M_0 at a rate of T_1. It is convenient to represent the transverse component as a single rotating vector $\mathbf{M_{xy}}$. It starts with magnitude $M_0 \sin\alpha$ and decays with time constant $T_2{}^*$. Thus:

$$M_{xy}(t,\ T_2{}^*) = M_0 \sin\alpha \cdot \exp(-t/T_2{}^*)$$

and

$$M_z(t,\ T_1) = M_0 \cos\alpha \cdot [1 - \exp(-t/T_1)] \qquad (1.8)$$

If this sequence is repeated with a TR comparable to T_1 and if M_{xy} dephases irreversibly between pulses, a 'steady state' is reached at which point M_{xy} after the pulse is equal to M_z immediately before the pulse (Figure 1.5b). The NMR signal decreases to

$$\frac{M_{xy}}{M_0} = \frac{[1 - \exp(-TR/T_1)]\sin\alpha}{1 - \cos\alpha \cdot \exp(-TR/T_1)} \exp(-t/T_2{}^*) \quad (1.9)$$

which includes the $T_2{}^*$ decay measured at time t relative to the last NMR pulse. The maximum NMR signal

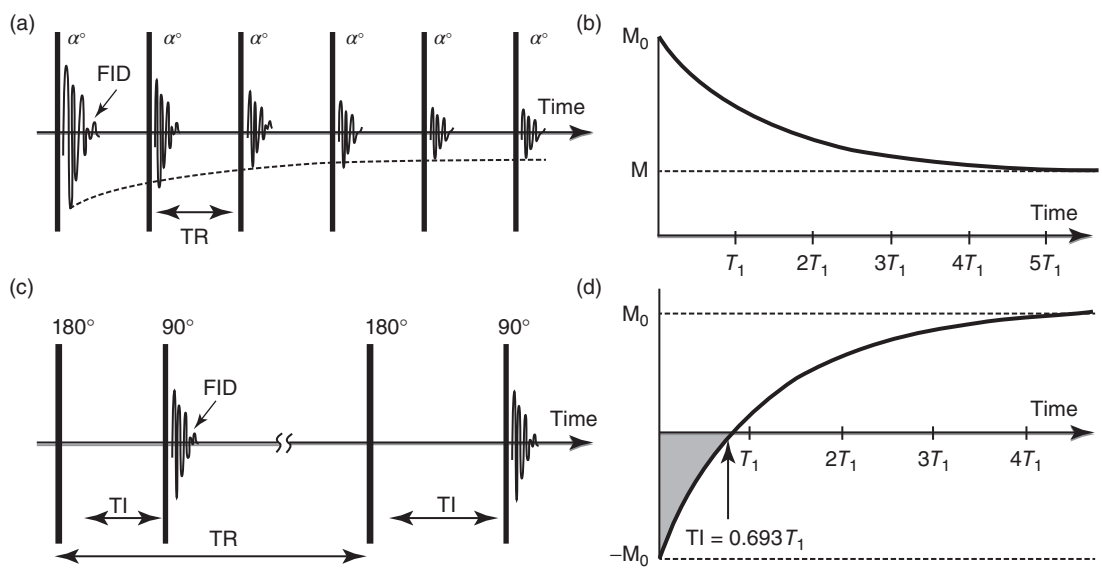

Figure 1.5. The effect of applying an RF pulse sequence comprised of a series of FA = $\alpha°$ pulses with period TR $\ll T_1$ (a) is to partially saturate the NMR signal, which declines to a steady-state value after several T_1s given by equation (1.9) (b). When $\alpha = 90°$, the steady-state value is $M_0(1 - \exp TR/T_1)$, per equation (1.12). Inversion recovery (IR) comprises a 180°–TI–90° sequence repeated at TR $\gg T_1$ (c). The magnetization is initially inverted and negative for TI $< 0.69\,T_1$, zero at TI $= 0.69\,T_1$, and positive for TI $> 0.69\,T_1$, spanning the range $\pm M_0$ (d)

per unit time occurs at the so-called 'Ernst angle' given by

$$\cos\alpha_E = \exp(-\mathrm{TR}/T_1), \text{ at which point} \quad (1.10)$$

$$\frac{\mathrm{M_{xy}}}{\mathrm{M_0}} = \sqrt{\frac{1-\exp(-\mathrm{TR}/T_1)}{1+\exp(-\mathrm{TR}/T_1)}}\exp(-t/T_2{}^*) \quad (1.11)$$

Equation (1.9) shows that if the simple $\alpha°$ pulse sequence is repeated with different values of TR, the signal measured at steady state will be dependent on T_1, which can be determined therefrom. In particular, when $\alpha = 90°$, the transverse magnetization has an initial amplitude

$$\mathrm{M_{xy}}/\mathrm{M_0} = [1-\exp(-\mathrm{TR}/T_1)] \quad (1.12)$$

In practice, the prudent course of analysis is to perform a three-parameter fit to the signal

$$\mathrm{S} = P - Q\cdot\exp(-\mathrm{TR}/T_1) \quad (1.13)$$

with P, Q, and TR as fitting constants, to compensate in part for the ill effects of B_1 inhomogeneity on FA. Because S declines or 'saturates' as TR is decreased because the spin population has insufficient time to equilibrate, this method of measuring T_1 is known as the *partial saturation (PS) method*. Note that the signal is considered completely 'saturated' when the population of spins occupying all of the nuclear magnetic energy levels are identical.

1.2.3.2 T_1 and Inversion Recovery

Adding pulses with different FAs adds complexity, especially for $\alpha \neq 90°$ or $\alpha \neq 180°$ and for short TRs, because the accumulated effect of all excitations applied within the spin memory of several T_1 periods must be accounted for. The special case of the 'inversion recovery (IR) method' starts with the magnetization at equilibrium, $\mathrm{M_0}\hat{\mathbf{z}}$, directed along the z-axis with unit vector $\hat{\mathbf{z}}$. A 180° 'inversion pulse' is applied, which inverts the longitudinal magnetization to $\{-\mathrm{M_0}\hat{\mathbf{z}}\}$. This generates no transverse magnetization ($\mathrm{M_{xy}} = 0$) and therefore no NMR signal. Nevertheless, the longitudinal magnetization begins to shrink from $\{-\mathrm{M_0}\hat{\mathbf{z}}\}$ and grows back along the z-axis toward equilibrium. Then, at some 'inversion time', TI, after the 180° pulse, a 90° pulse is applied (Figure 1.5c). This flips the residual shrinking/growing $\mathrm{M_z}$ component into the x–y plane. The signal immediately following the 90° pulse (with the $T_2{}^*$ term omitted) is:

$$\mathrm{M_{xy}} = \mathrm{M_0}[1-2\exp(-\mathrm{TI}/T_1)] \quad (1.14)$$

Repeating this sequence with a set of different TI values yields an exponential curve from which T_1 can be obtained from signals measured at the same time t relative to the last (90°) pulse (Figure 1.5d).

Again, it is prudent to fit the data to an equation of the form of equation (1.13), replacing TR by TI. The IR method is advantageous over PS in that it provides twice the dynamic range of signal dependence on T_1. A disadvantage is that equation (1.14) is only valid when starting from equilibrium: repeat applications of the sequence require a delay of $\mathrm{TR} \gg T_1$, which reduces its efficiency for signal averaging or spatial localization. Note also that in the special case when

$$\exp(-\mathrm{TI}/T_1) = 1/2, \text{ i.e., } \mathrm{TI} = 0.693\ \mathrm{T_1} \quad (1.15)$$

Equation (1.14) shows that $\mathrm{M_{xy}}$ passes through zero. At this point, T_1 can be obtained directly from a single determination of the TI that yields zero signal from an IR experiment, using equation (1.15). This is known as the *T_1-null* method.

1.2.3.3 T_2 and Spin-Echoes

The distinction between T_2 from $T_2{}^*$ is whether the decay in $\mathrm{M_{xy}}$ is facilitated by intrinsic molecular-level interactions or by other external instrumental factors. Of the latter, the primary culprit is static magnetic field inhomogeneity. Such dephasing can be reversed by the 'Hahn spin-echo (SE)' experiment.[6] The SE experiment also employs 90° and 180° pulses, but in reverse order to IR (Figure 1.6a). Starting with the nuclei at equilibrium, the first 90° pulse flips $\mathrm{M_0}$ into the transverse (x–y) plane, where it begins to decay at $T_2{}^*$. Nuclei in different locations in the sample dephase owing to local differences in B_0 arising from the inhomogeneity and equation (1.1). However, even though the observed signal may have completely dephased to zero, nuclei at different locations in the sample may still precess coherently about $B_0\hat{\mathbf{z}}$ at their own Larmor frequencies, as yet unaffected by the intrinsic spin–spin (T_2) relaxation processes.

Application of a 180° inversion pulse at time TE/2 following the 90° pulse inverts all of the spins in the x–y plane: they remain in the x–y plane, but their relative phases are now reversed (Figure 1.6b). The B_0 inhomogeneity that caused the dephasing is unchanged, so the phases of the nuclei continue to evolve at the same rates. However, now as a consequence of the phase reversal imparted by the 180° pulse, the continued phase evolution brings the nuclei back into phase, producing a 'SE' at time TE.[6] The echo signal waxes

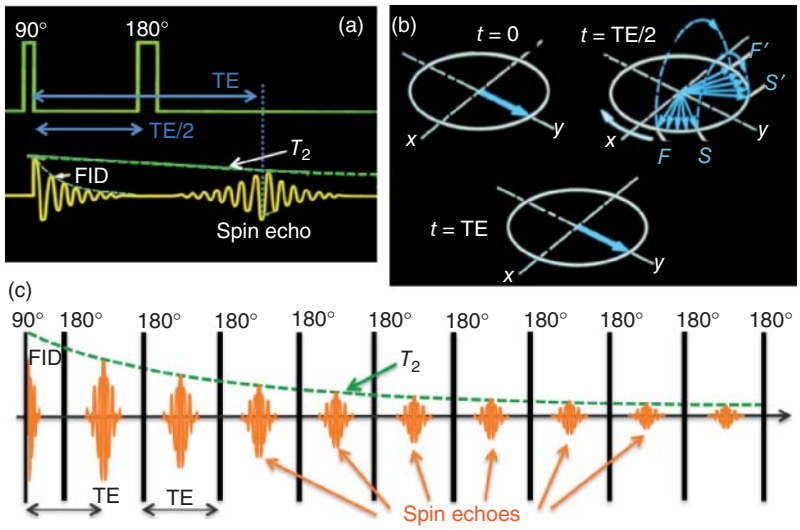

Figure 1.6. (a) The spin-echo pulse sequence comprises a 90°–TE/2–180° pulse sequence producing a spin-echo at time TE whose peak height is attenuated by T_2. (b) At time $t = 0$, the 90° pulse tips **M** into the x–y plane and the spins begin to dephase owing to T_2* processes. At $t = \mathrm{TE}/2$, the 180° pulse flips over the dephasing spins, but the continued dephasing now brings spins F to S back together to form the echo at $t = \mathrm{TE}$. (c) In the Carr–Purcell sequence, a train of spin-echoes are induced by repeating the 180° pulses at intervals of TE after the first 180° pulse. The height of the echoes traces the T_2 decay

and wanes with time constant T_2*, but the signal at the center of the echo is decreased relative to the signal immediately following the initial 90° pulse, by only the intrinsic T_2, plus the effects of translational diffusion.[6,15] The latter arises because echo formation does not compensate for the effects of spins moving to a slightly different B_0 during TE. A plot of the maximum echo-height measured after repeating the experiment with a series of different TE values is – according to equation (1.5) – exponential with time constant T_2.

Echo formation need not end with a single echo. The T_2*-dephased echo can be refocused again and again using a 'Carr–Purcell (CP)' sequence[15] wherein 180° pulses are repeated at intervals of TE following the first 180° pulse, which was applied at time TE/2 after the first 90° pulse (Figure 1.6c). The echoes form at the center of each TE period, and it can be shown that the mean-square of the phase dispersion due to translational diffusion in a B_0 field with static inhomogeneity is reduced by n_e^2, where n_e is the number of spin echoes in the CP 'echo-train' with $\mathrm{TE} \ll T_2$.[15] The peak signal of each echo in the train traces the exponential T_2 decay, so T_2 can be measured from a single 90°–n_e{TE/2–180°–TE/2} pulse sequence (with n_e = the number of echoes; Figure 1.6c). However, if the 180° pulses are not perfectly set, errors accumulating during the course of the echo-train cause dephasing that results in the measured T_2 being lower than it should be. This error may be remedied by phase-shifting the B_1 by 90° between the 90° pulse and the subsequent 180° pulses – basically shifting the B_1 field from the x-axis to the y-axis in the rotating frame of reference, say.[16] The effect of the error – the displacement of **M** above or below the x–y plane – remains, but it is not cumulative. This small modification to CP is known as the 'Carr–Purcell–Meiboom–Gill' (CPMG) sequence.[16] The decay in the peak echo height following the ith 180° pulse is thus:

$$\mathrm{M} = \mathrm{M}_0 \exp(-n_i \mathrm{TE}/T_2) \qquad (1.16)$$

Note that while the SE, CP, and CPMG experiments are designed to overcome the effects of static (B_0) magnetic field inhomogeneity, they are ineffective in dealing with time-dependent inhomogeneities occurring within periods of order T_2, such as those due to eddy currents induced in surrounding metallic structures by MRI or MRS localization gradients, 'unbalanced' spatial localization gradients, temperature, or current variations in the permanent or electromagnets used to generate B_0.

1.2.3.4 Stimulated Echoes

Spin echoes can actually be stimulated whenever multiple pulses are applied in intervals that are short compared to T_2. For example, when a 90° pulse followed by another 90° pulse at time TE/2, an echo will form at time TE (Figure 1.7a).[6] This is because after the first 90° pulse, the spins dephase to form a pancake in the x–y plane, which is tipped into the y–z plane by the second 90° pulse (Figure 1.7b,c). The relative phases of the spins are also inverted, as in the SE method. This pancake has a component equal to half of the magnetization in the x–y plane, which refocuses to form a 'stimulated echo (STE)' (Figure 1.7d).[6,17] The rest of the signal is in the longitudinal direction, not subject to T_2 relaxation processes, and is not detected. The height of the echo in the x–y plane traces an exponential in TE/T_2 as in the other T_2 methods.

Echoes stimulated in this manner are generally not used to measure T_2 because of their reduced signal vs the SE and CP approaches. However, the sequence is used in MRS and MRI to buy time for other spatial or functional encoding involving the half of the magnetization that is preserved from T_2 decay in the longitudinal direction with its 'spin memory' otherwise intact. The typical application involves a third 90° pulse applied at a 'mixing time, TM' after the second 90° pulse (Figure 1.7e). During the TM ($\ll T_1$) period, the half of the magnetization comprising the longitudinal components of the pancake is dispersed along the z-axis, quietly relaxing at T_1. Meanwhile, the STE occurring between the second and third 90° pulses from the other half of the magnetization in the transverse plane is ignored or deliberately dephased (see the following text). The third 90° pulse tips all of the remaining longitudinal components into the x–y plane, where they are again subject to T_2 processes resulting in an STE at time TE/2 later. Although in this case, a total time {TE + TM} has elapsed (Figure 1.7e), the T_2 decay approximates that of the shorter period, TE.

Generally, in order for the STE to derive solely from all three 90° pulses together and not subsets thereof, other spurious NMR signals must be suppressed. For example, in addition to the signal from the longitudinal component preserved during TM and stimulated by all three pulses, there are three FIDs from the three

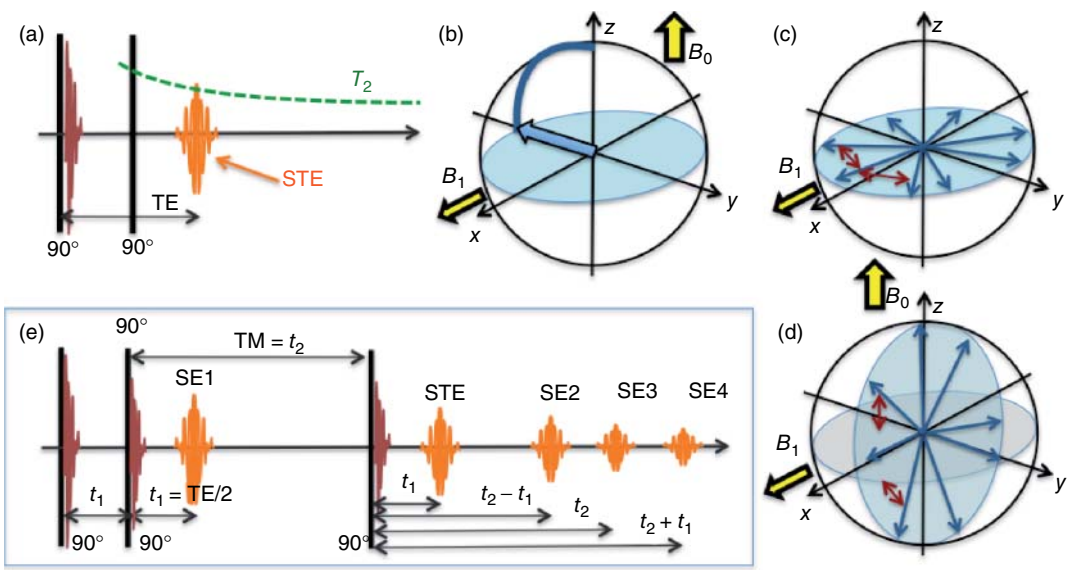

Figure 1.7. (a) Simple stimulated echo (STE) pulse sequence comprised of two 90° pulses spaced by period TE/2. The STE produced by repeating the sequence with different TEs traces a T_2 curve. (b) The first 90° pulse flips the spins into the x–y plane where they dephase owing to T_2* processes (c). The second 90° flips the pancake vertically inverting half (d), which refocuses forming the STE. (e) A typical STE sequence used for MRS includes a third 90° at time t_2 = TM after the second. This tips the longitudinal component not included in SE1 into the x–y plane to generate the STE. However, there are four other echoes (SE1–SE4) that are not produced by all three pulses, and are generally not acquired or deliberately dephased. (Adapted from Refs 6 and 17)

90° pulses taken individually; then the three STEs from the first and second, the first and third, and the second and third pulses; plus an echo from the first STE and the third pulse (Figure 1.7e).[17] Suppression is generally performed by application of short intense magnetic field gradient 'crusher pulses' applied after each RF pulse gradient (see Chapter 7).[18] The crusher pulses rapidly dephase the unwanted signals, to vanquish them from the echo time at {TE + TM} at which point the signal is sampled. To ensure that the same dephasing environment (due to the field inhomogeneity imposed by the gradient pulses) is present during the first and second TE/2 periods for correct formation of the STE, the gradient pulses after the first and the third 90° pulses must be identical.

1.2.3.5 T_2 and Linewidth

While T_1 is a measure of the rate of transitioning between the $2(I+1)$ energy levels that arise from the combined effect of $\mathbf{B_0}$ and the quantized spin angular momentum, T_2 being a measure of the local magnetic field environment reflects the linewidth of the energy levels (Figure 1.1b). Because the local magnetic field experienced by each spin affects the local NMR frequency, ν_0, via equation (1.1) and ν_0 is related to energy via $E = h\nu_0$, the linewidth of the resonance in units of B_0, frequency, and energy are all proportionate. If the effects of instrumental B_0 inhomogeneity can be neglected (i.e., $T_2 \ll T_2{}^*$), the linewidth of the NMR signal measured in hertz at 'full-width half-maximum (FWHM)' in a c.w. NMR experiment is

$$\Delta\nu_0 = 1/(\pi T_2) \tag{1.17}$$

This relates an exponential decay with time constant T_2 seen by pulsed NMR to the width of the same resonance studied in a c.w. frequency-sweep experiment. The lineshape in c.w. NMR that corresponds to the exponential decay in the pulse experiment is a 'Lorentzian function', which is given by:

$$f_{\mathrm{L}}(\nu, T_2) = \frac{T_2}{1 + \{2\pi(\nu - \nu_0)T_2\}^2} \tag{1.18}$$

with ν as the sweep frequency. This function peaks at $\nu = \nu_0$. Equation (1.17) is the solution of equation (1.18) for $f_{\mathrm{L}} = \pm 1/2$.

Another lineshape often encountered in NMR is 'Gaussian'. This differs from Lorentzian in that it decays faster at the wings of the resonance, or equivalently, as time advances during the FID. This can arise owing to more ordered (lattice-like) interactions between the spins, or more commonly in vivo, owing to instrumental factors such as transient gradients arising from residual eddy currents that are induced in the magnet structure by magnetic field gradient pulses used for spatially localizing the NMR signal. In any case, Gaussian lines have the form:

$$\begin{aligned} f_{\mathrm{G}}(\nu, T_2) &= \exp(-[\nu - \nu_0]^2/2\sigma^2) \\ &= \exp(-4\pi[\nu - \nu_0]^2 T_2{}^2) \end{aligned} \tag{1.19}$$

where $\sigma = 1/\{T_2\sqrt{(8\pi)}\}$ is the standard deviation of the Gaussian function. Solving for $f_{\mathrm{G}} = \pm 1/2$ analogous to equation (1.17) yields an FWHM for Gaussian lines of:

$$\Delta\nu_0 = \frac{\sqrt{\ln 2/\pi}}{T_2} \tag{1.20}$$

Even though T_2 can be obtained from linewidth measurements via equations (1.17) or (1.20), it is prudent to replace T_2 by $T_2{}^*$ when instrumental contributions are significant or unknown.

1.3 FOURIER TRANSFORM NMR

The healthy ear is accustomed to differentiating the time-dependent audible signals of popular music by their discrete frequencies – bass, mid-range, treble, monotonic drones, whistles, etc. As implied by equations (1.17–1.20), the time-dependent NMR signal is intimately related to the frequency spectrum. A single exponentially decaying time-domain NMR signal detected by an FM radio receiver tuned to $\{\nu_0 + 1000\}$ Hz sounds such as a single pure 1 kHz note struck and decaying with a time constant T_2. Its frequency spectrum is a single peak at 1 kHz whose sharpness increases as T_2 (or $T_2{}^*$) lengthens.

The standard method of determining a frequency spectrum from a time signal mathematically (vs the human ear) is the 'Fourier transform (FT)'. The FT fits an interval of time domain, say an NMR acquisition window tAQ, with a mathematical series comprised of a sum of time-dependent sine and cosine waves.[19] The frequencies of the waves are in practice limited to the 'bandwidth (BW)' set by the receiver (analogous to the audible frequency range of hearing). Because the NMR signal is circularly polarized (see Section 1.2.2.1), it is convenient to represent it by Euler's formula, $\exp(i\omega t) = \cos(\omega t) + i\sin(\omega t)$, with complex 'real' and 'imaginary' components 90° out of phase, and $i = \sqrt{-1}$. The FT is thus generally

written in complex form. A plot of the amplitudes of all the sine (and cosine) waves obtained by FT of the complex time-domain signal from the pulsed NMR experiment, arranged as a function of frequency, now constitutes the 'NMR spectrum'. The complex spectrum obtained by FT of the time-domain signal from the pulse experiment is:

$$S(\omega) = \int_{\mathrm{tAQ}} s(t)\mathrm{e}^{-i\omega t}\mathrm{d}t \;\text{ or }\; S(\nu) = \int_{\mathrm{tAQ}} s(t)\mathrm{e}^{-i2\pi\nu t}\mathrm{d}t \tag{1.21}$$

Moreover, this result is equivalent to the complex (circularly polarized) spectrum measured by c.w. NMR. Conversely, the FT of the frequency-domain signal from the c.w. experiment is:

$$s(t) = \frac{1}{2\pi}\int_{\mathrm{BW}} S(\omega)\mathrm{e}^{i\omega t}\mathrm{d}\omega \;\text{ or }\; s(t) = \int_{\mathrm{BW}} S(\nu)\mathrm{e}^{i2\pi\nu t}\mathrm{d}\nu \tag{1.22}$$

which is equivalent to the time-domain signal measured by pulsed NMR.

As an example, the real component of the FT of $s(t) = \mathrm{M}_{\mathrm{xy}}(t,\ T_2)$ from equation (1.8) is equal to $S_{\mathrm{Re}}(\nu) = f_{\mathrm{L}}(\nu,\ T_2)\cdot \mathrm{M}_0 \sin\alpha$, with f_{L} defined in equation (1.18). The corresponding imaginary component is $S_{\mathrm{Im}}(\nu) = f_{\mathrm{L}}'(\nu, T_2)\cdot \mathrm{M}_0 \sin\alpha$, where

$$f_{\mathrm{L}}'(\nu, T_2) = \frac{2\pi(\nu-\nu_0){T_2}^2}{1+\{2\pi(\nu-\nu_0)T_2\}^2} \tag{1.23}$$

is the 90° 'out-of-phase' complement of equation (1.18). By convention, the real, 'in–phase' or pure 'absorption-mode' component of the complex spectrum is taken as that in which the signal is all positive. The 'imaginary', 'quadrature', or 'dispersion-mode' component, being 90° out of phase, has both positive and negative components. In practice, FT often produces an asymmetric mixture of absorption and dispersion modes that must be corrected by adding a phase term (ϕ) to the exponent (e.g., $\exp\{i\omega t + \phi\}$etc.) when the absorption mode is to be viewed as is customary.

Of course, equations (1.18–1.23) also assume a continuous distribution of signal in the time and frequency domains. While a continuous distribution is appropriate for analog detection, NMR signals today are invariably not continuous, but digitally sampled by analog-to-digital converters (ADCs) into N complex data points, a process performed after they have been amplified and demodulated (see Section 1.1.2). FT is then done in a digital computer. In this case, the integrals in equations (1.21) and (1.22) are replaced by the corresponding series formed by the digitized data points:

$$S\left(\frac{k}{N\Delta t}\right) = \sum_{n=0}^{N-1} s(n\Delta t)\mathrm{e}^{-i2\pi nk/N} \tag{1.24}$$

where Δt is the 'sampling interval' per datum also known as the 'dwell time'; and n and k and integers denoting the nth and kth point in the time and frequency domains, respectively. Equation (1.24) is known as the *discrete Fourier transform* (*DFT*). Similar series replace the other integrals in equations (1.21) and (1.22).

The great advantage of the FT NMR method is that it can acquire an entire spectrum in a single acquisition, whereas the c.w. method must acquire it one point at a time. The upshot is an enormous N-fold efficiency advantage for FT NMR, which can translate to SNR. For example, if the pulse experiment is repeated N-times and the results added to obtain a spectrum in the same time as the point-by-point c.w. experiment, a $\sqrt{N}$-fold SNR advantage results, because the signals add $\propto N$ while the RMS of random noise adds $\propto\sqrt{N}$. This assumes equivalent receiver BW and RF excitations for the two experiments, which may well not be the case. Nevertheless, enormous gains in efficiency and SNR were realized when FT NMR was introduced.[19]

1.3.1 Time-Domain Filtering

So, how long should the acquisition window in the time domain, tAQ, be, and how does it relate to the receiver BW or 'sweep-width' in the c.w. experiment? Because time and frequency are 'conjugate pairs', in the DFT experiment

$$\mathrm{BW} = 1/(\mathrm{tAQ}) = 1/(N\Delta t) \tag{1.25}$$

As it takes at least two points in each cycle to define a frequency, the highest frequency that can be digitally sampled and accurately resolved in this interval is $\nu_{\mathrm{Nyq}} = 1/(2\,N\Delta t) = 1/(2\cdot \mathrm{tAQ})$. Thus, BW must at least extend to the range $\pm\nu_{\mathrm{Nyq}}$, where ν_{Nyq} is known as the *Nyquist frequency*. Because the frequency or 'spectral' resolution is inversely proportional to the acquisition window, the spectral resolution increases when tAQ is extended. However, extending tAQ for more than 2.5 times $T_2{}^*$ may add little more than noise, limits TR and TE, and reduces SNR efficiency (SNR per unit time). One trick that is routinely used in MRS is to double or quadruple the time-domain data simply by appending zeros or 'zero-filling' the acquisitions. Noticeable improvements in spectral resolution can be obtained with

up to about a fourfold zero fill. Zero-filling is mathematically equivalent to interpolation and adds no new information – neither signal nor noise. Its only cost is digital memory and processing time.

Given the signal's approximately exponential decay with time t during the acquisition window while the RMS noise remains constant, it also makes sense to match the corresponding decline in SNR with a filter that reduces the noise at the same rate. Multiplication of the time-domain signal by an exponential filter, $\exp(-t/T_f)$ whose time-constant, T_f, matches the signal decay, $T_2{}^*$, is another standard MRS practice. Exponential filtering improves SNR, albeit at the expense of a broader linewidth produced by the faster decay. The decay rates are additive, so the apparent T_2-rate post-filtering is $1/T_{2f} = \{1/T_2{}^* + 1/T_f\}$. From equation (1.17) after filtering the FWHM is $\{1/(\pi T_2{}^*) + 1/(\pi T_f)\}$. Gaussian filtering may be performed with a function $\exp\{-\pi(t/2T_f)^2\}$ to match T_f to T_2 consistent with the time-domain conjugate of equation (1.19), $f_G(t) \sim \exp\{-2(\pi\sigma t)^2\}$. The filter settings are conventionally reported as rates, $1/T_f$ in hertz.

1.4 NMR SPECTROSCOPY

1.4.1 Chemical Shift

Many of the earliest NMR experiments were designed to measure the gyromagnetic ratios (γ's) of the nuclei. However, as B_0 homogeneity and the spectral resolution of NMR spectrometers improved, it was found that the same nuclei on different molecular compounds resonated at slightly different frequencies.[20,21] The effect was attributed to the fact that nuclei experience not exactly the main externally applied magnetic field, but the net local field after it is screened or shielded by the electrons that surround the nucleus. This shielding arises from the effect of B_0 on the electron's motion, which produces a small magnetic field that opposes B_0 (analogous to Lenz's law). The effective field at the nucleus is

$$\mathbf{B}_{\text{eff}} = \mathbf{B_0}(1 - \sigma) \tag{1.26}$$

where σ is called the 'shielding constant'. Consequently, the NMR frequency is shifted to

$$\nu = \gamma B_{\text{eff}} = \gamma B_0(1 - \sigma) = \nu_0(1 - \sigma) \tag{1.27}$$

This frequency shift is known as the *chemical shift*.

In equation (1.27), ν_0 is now the resonant frequency of the bare nucleus – in theory. In practice, it is the frequency of an agreed upon reference compound. For ^{1}H and ^{13}C NMR, the reference resonance is tetramethyl silane (TMS); for ^{31}P NMR, it is phosphoric acid (H_3PO_4) in vitro or phosphocreatine (PCr) in vivo. The chemical shift is customarily defined as the difference in resonant frequency from the reference, measured in 'parts-per-million (ppm)' relative to ν_0,

$$\delta = (\nu_0 - \nu) \cdot 10^6/\nu_0 \tag{1.28}$$

displayed with δ increasing to the left ($-x$-axis). *Because σ is not field dependent, neither is δ.* However, because $\nu = \gamma B_{\text{eff}}$, the magnitude of the chemical shift dispersion, $\{\nu_0 - \nu\}$ measured in hertz, increases linearly with B_0. Consequently, *the spectral resolution of an NMR spectrum also increases linearly with B_0*, provided that the linewidths (or T_2s) are not frequency dependent.

The chemical shift phenomenon has proven immensely valuable in chemistry and biochemistry, because the same groups of magnetically equivalent nuclei or 'moieties' in different chemical environments can be distinguished and identified based on their resonant frequencies. One of the earliest examples is pictured in Figure 1.8.[21] This c.w. NMR spectrum of ethanol revealed ^{1}H resonances from its three moieties, $-CH_3$, $-CH_2-$, and $-OH$, in characteristic locations with relative intensities 3 : 2 : 1 corresponding to the relative nuclear spin densities, n_m, of protons on each moiety, on the molecule.[21] *The chemical shift effect requires a chemical (electron)*

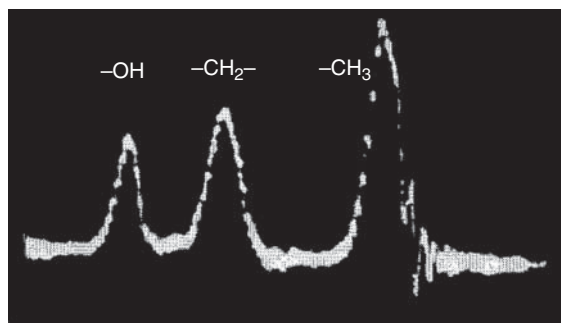

Figure 1.8. Perhaps the first NMR spectrum of an organic compound published.[21] This ^{1}H spectrum from ethanol recorded at 0.76 T shows the three moieties ($-OH$, $-CH_2-$, and $-CH_3$) as a function of field strength, with the $-OH$ and $-CH_2-$ groups separated by about 1.6 μT or 2 ppm (Reprinted with permission from J. T. Arnold, S. S. Dharmatti, and M. E. Packard, J. Chem. Phys., 1951, 19, 507. Copyright 1951, AIP Publishing LLC)

bond, and does not occur through space (hydration or hydrogen bonds do not qualify). In general, the relative peak areas from each moiety are proportional to the number of NMR nuclei on the moiety. Because relaxation is intimately associated with the local molecular-level environment, which can vary with position and the degrees of freedom of mobility on the molecule, *each moiety can have its own separate T_1 and T_2,* and often does.

Note that, strictly speaking, σ is a tensor that depends on the orientation of the molecule relative to $\mathbf{B_0}$. However, for molecules in liquid-like phases, as in most in vivo applications, σ may be considered a scalar. Early attempts at calculating σ from the effect of electron shielding currents on nuclei in magnetic fields decomposed it into a sum of paramagnetic and diamagnetic terms that were linked to the symmetry of electronic orbitals, interactions with neighboring atoms, and interatomic currents.[22,23] While differences in the paramagnetic contribution provided some insights into the large chemical shift ranges seen in nuclei such as ^{19}F (~300 ppm), ^{31}P (~40 ppm in vivo), and ^{13}C (~200 ppm in vivo), as compared to ^{1}H (~10 ppm in vivo), in practice, the complexity and sheer number of chemical interactions render such computations far less useful than the few seconds it takes to perform an actual NMR spectroscopy experiment. Chemical shift ranges for some common ^{1}H moieties are depicted in Figure 1.9.

1.4.2 Spin–Spin Coupling

In striving to further improve the NMR spectroscopy experiment with yet more homogeneous magnets to achieve narrower resonance linewidths and therefore higher SNR, it was found that not only did NMR spectra consist of individual lines for each moiety, but that each moiety itself often split into groups of lines, or 'multiplets'.[24] The multiplet structure arises from interactions involving 'spin–spin coupling' between nuclei that cause energy levels to split, resulting in several transitions instead of the single transition otherwise expected. The interactions responsible for spin–spin coupling are *intramolecular: acting only through electron bonds, and not through space*. These are not to be confused with spin–spin coupling involving dipole–dipole interactions that can be intermolecular, but often average to near zero for small molecules in solution.

Consider two spin-1/2 nuclei, A and B, with A parallel to $\mathbf{B_0}$. An electron near A will tend to orient antiparallel to A. Another electron in the same orbital will be antiparallel to the first electron (by the Pauli exclusion principle), and therefore parallel to A. If the second electron is near B, it will tend to orient B, thereby communicating information about the spin orientation of nucleus A to nucleus B. The most favorable state is when nuclei A and B are antiparallel. When A flips during NMR, its transition energy depends on the initial orientation of B relative to A, giving rise to two spectral lines. The difference in frequency corresponding to the energy difference is proportional to the interaction or coupling between A and B, and is called the 'coupling constant, J', measured in hertz. Coupling can occur when two nuclei are bonded together or when several bonds intervene, although the magnitude of the coupling tends to decrease as the number of intervening bonds increases. *Coupling can be between the same nuclear isotopes – termed 'homonuclear coupling' – or between different NMR nuclei – called 'heteronuclear coupling'. Importantly, J, in hertz, is independent of B_0.*

Spin–spin coupling in spectra arising from nuclei of the same type is commonly treated by a first-order

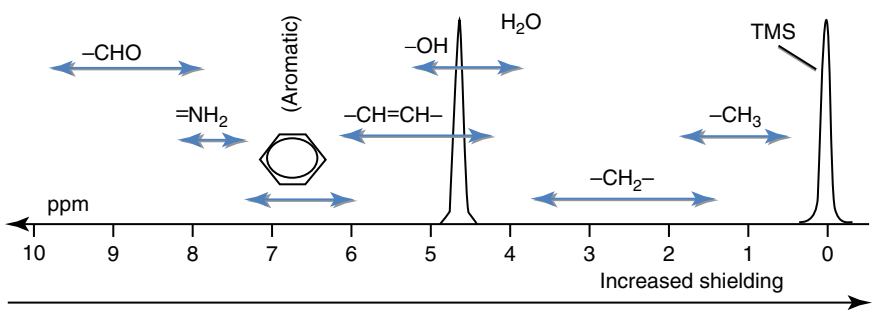

Figure 1.9. ^{1}H chemical shift ranges (horizontal arrows) for some common organic moieties (TMS = tetramethyl silane)

analysis when (i) the chemical shift difference between nuclei or groups of nuclei is much larger than the spin coupling between them and (ii) the nuclei on a coupled group or moiety are both chemically and magnetically equivalent. Nuclei are chemically equivalent when they have the same chemical shift, and magnetically equivalent when they are of the same isotope, coupled equally with any other single nucleus in the molecule. Under these conditions, the number of peaks in a multiplet, their spacing, and their relative intensities follow the following rules:

1. A nucleus or moiety coupled to another moiety comprised of a set of n_m nuclei with spin I, will have a multiplet of $\{2n_m I + 1\}$ lines.
2. The relative intensities of the $\{2n_m I + 1\}$ lines are determined from the number of ways each spin state (aligned with or against B_0 etc.) can be formed. For $I = 1/2$ (e.g., ^{1}H, ^{31}P, and ^{13}C), the relative intensities of the $\{n_m + 1\}$ lines correspond to the coefficients of a binomial series (Table 1.2).
3. The $\{2n_m I + 1\}$ lines are equally spaced and separated by J, the coupling constant.
4. Coupling between magnetically equivalent nuclei within a moiety does not affect the spectrum.

When condition (i) is not met, the spectrum may be strongly coupled or 'second order'. In this case, multiplet symmetry may be lost, the spacing may not equal J, and the splittings and multiplets may no longer correspond to a single moiety. Computer simulations may aid spectral assignment.

The rules are applied by assuming the viewpoint of each moiety in turn, treating all nuclei on the moiety you are on as one. For example, consider the case of homonuclear ^{1}H spin–spin coupling in acetaldehyde (CH_3CHO), which has two moieties, CHO and CH_3 (Figure 1.10a). All the CH_3 protons are magnetically equivalent and have a single chemical shift. From the CH_3 moiety proton's viewpoint (Figure 1.10b), there is a carbon bond that has a 98.9% isotopic probability of being a ^{12}C with no nuclear spin, and a single proton (^{1}H) on the CHO group. The 99.96% abundant ^{16}O isotope also has no spin. Thus, from Table 1.2, $n_m = 1$ and the CH_3 is split into a doublet with equal peak intensities that correspond to the two possible spin alignments of the CHO proton, with and against B_0. Now from the CHO's viewpoint, there are $n_m = 3$ proton nuclear magnets on the other side of the carbon bond. Therefore, the proton on the CHO group is split into a quadruplet with relative amplitudes 1 : 3 : 3 : 1. This arises from the $2^3 = 8$ combinations that three protons can be oriented with and against B_0 (one combination each with all spins oriented either with or against B_0 and three combinations each with two of three spins oriented either with or against B_0 (Figure 1.10a)). Finally, because there are three protons on the CH_3 and only one on the CHO, the integrated signal of the doublet is three times the integrated signal from the quadruplet.

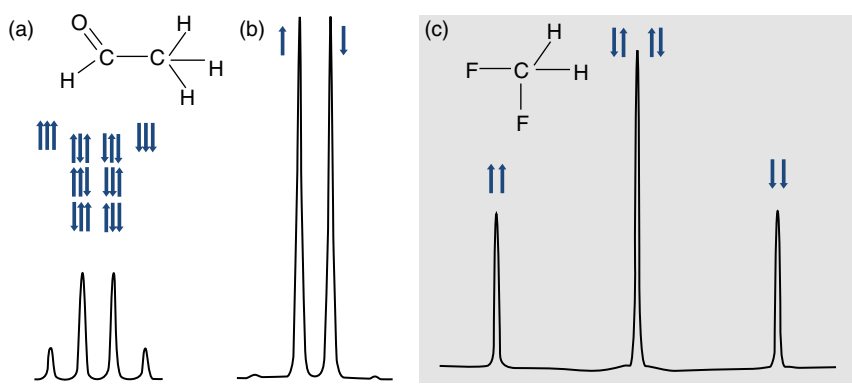

Figure 1.10. (a, b) Acetaldehyde has two ^{1}H-bearing moieties, –CHO and CH_3. (a) The –CHO moiety is split into a 1 : 3 : 3 : 1 multiplet corresponding to the number of energetically different orientations of the three spins on the CH_3 group (blue arrows: all up, all down, three combinations with two spins up, and three combinations with two spins down). (b) The $-CH_3$ moiety is split into a doublet from the two possible orientations of the proton on the –CHO group (up or down). The integral of the doublet is 3× that of the quadruplet. (c) Difluoro-methane has two magnetically different moieties of two spins each, giving rise to a 1 : 2 : 1 triplet in ^{1}H and ^{19}F spectra arising from the three different spin combinations (all up, all down, and two combinations with one spin up and one down)

Table 1.2. Number of multiplet peaks and relative intensities in spin–spin coupled spectra

n_m	Number of peaks in multiplet	Relative intensities
0	1	1
1	2	1, 1
2	3	1, 2, 1
3	4	1, 3, 3, 1
4	5	1, 4, 6, 4, 1, etc.

Heteronuclear spin–spin coupling is illustrated in the case of difluoromethane (CH_2F_2; Figure 1.10c). The ^{19}F nucleus has 100% isotopic abundance, has a strong nuclear magnetic moment, and is chemically bonded to the same carbon. If this were regular methane (CH_4), all the protons would be indistinguishable and constitute a single moiety with a single peak. However, two ^{19}F nuclei cannot be magnetically equivalent to two ^1H nuclei. The H_2 and F_2 therefore behave as two moieties, each split by the other into a single triplet in the ^1H spectrum and also in the ^{19}F spectrum. The triplets have amplitudes $1:2:1$ corresponding to $n_m = 2$.

1.4.3 Decoupling and Overhauser Enhancement

While spin–spin coupling provides information on the chemical structure of adjacent chemically shifted moieties, in applications of MRS to materials comprised of mixtures of substances such as biological tissues, the presence of overlapping multiplet structures can obfuscate the identification and quantification of metabolites and/or compounds of interest. In addition, dividing up the NMR signal from a moiety into multiple peaks reduces the SNR relative to having the entire signal concentrated in a single peak. Fortunately, it is possible to collapse the multiplet structure of a moiety A that arises from its spin–spin coupling to a neighboring moiety B, into a single line. This is achieved by applying a second 'decoupling' B_1 magnetic field precisely tuned to moiety B, in addition to the regular MRS excitation field. Spin decoupling of moiety A occurs when moiety B changes its alignment relative to $\mathbf{B_0}$ (i.e., flips between its multiplet energy states) at a rate faster than the coupling constant J_{AB} between A and B. This results in saturation of the multiplet states. Decoupling simplifies the spectrum of A and increases its SNR by the sum of the heights of the collapsed multiplet peaks.

When A and B are of the same isotope, the technique is called 'homonuclear decoupling'. Practical difficulties in implementing it in vivo include ensuring that the decoupling B_1 field is precisely tuned to moiety B and does not clip moiety A, especially when B_0 and ν_0 vary relative to the chemical shifts and/or linewidths of A and B over the large sample volumes encountered in vivo. The power requirements for achieving complete decoupling and protecting the NMR spectrometer's sensitive preamplifier from the decoupling power are other considerations.

When A and B are different nuclei or isotopes (e.g., ^1H and ^{13}C or ^{19}F), the decoupling is said to be 'heteronuclear'. Here the resonances are typically far enough away (i.e., many megahertz), that the selection of B can be 'broadband'. Broadband decoupling ensures not only the decoupling of B from A on a single 'moiety of interest' (MOI) but also the decoupling of all other B nuclei from type A nuclei, on all moieties. From the practical standpoint, all that is required is some RF filtering applied at B's NMR frequency, to stop the B_1 decoupling signal from affecting detection of A at the spectrometer's preamplifier input.

The 'Overhauser effect' is a method of transferring magnetization of one spin system – originally unpaired electrons in metals – to another spin system, via dipole–dipole interactions.[25,26] Although far less effective than 'hyperpolarization' techniques (see Chapters 33, 39, and 40), the 'nuclear Overhauser effect (NOE)' is primarily used in vivo for transferring polarization from a high-γ nucleus B, such as ^1H, to a low-γ nucleus A, such as ^{13}C, for the purpose of enhancing the SNR of the latter. An NOE can be observed when dipole–dipole interactions between A and B represent a prominent T_1 relaxation mechanism for A. Basically, nucleus B is irradiated to saturation, which equalizes the spin populations in its nuclear energy levels. The spin population and transitions for A, being dipolar coupled, are also altered proportional to the ratio of γ_B/γ_A depending on the strength of the dipolar interaction [equation (1.3)]. The NOE can be positive or negative depending on the sign of μ, and decreases as A–B dipolar interactions lessen. The maximum achievable NOE is $\{1 + \gamma_B/2\gamma_A\}$. The maximum NOE achievable by irradiating ^1H during ^{13}C MRS, for example, is $\{1 + \gamma_{^1H}/2\gamma_{^{13}C}\} = 3$.

Unlike spin–spin coupling, NOE can occur through space and via intramolecular processes: it does not require a chemical bond. The NOE irradiation can be turned off for periods that are short compared to T_1, such as during an acquisition window, without

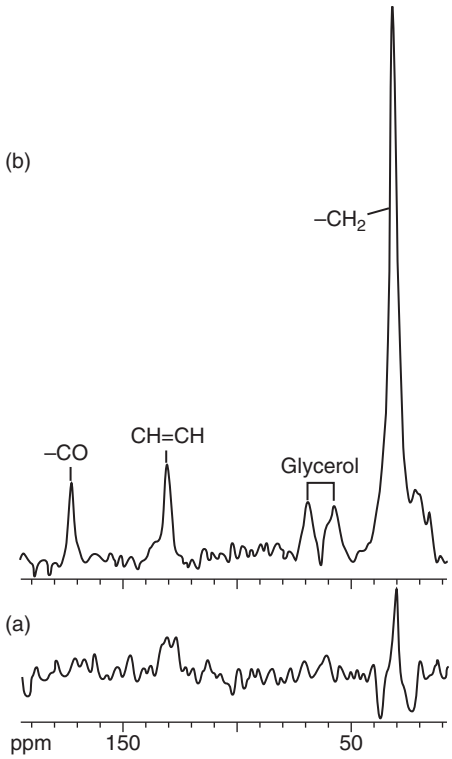

Figure 1.11. Natural abundance ^{13}C NMR spectrum acquired at 1.5 T by placing a loop detector coil on the leg of a healthy human volunteer without (a), and with (b) ^{1}H decoupling and NOE.[27] Two FIDs were averaged (TR = 0.5 s) and the decoupler deposited 3 W of RF power into the tissue. Chemical shift is relative to TMS. (Reproduced with permission from Ref. 27. © John Wiley & Sons, Ltd., 1989)

a significant loss in enhancement. Conversely, the decoupling irradiation must be on *during* signal acquisition to achieve spin–spin decoupling, but not necessarily *on* at other times. Figure 1.11 illustrates the combined effect of decoupling and NOE on a ^{13}C spectrum from a human leg in vivo at 1.5 T.[27]

1.4.4 Water Suppression

^{1}H NMR spectra of solutions such as milk, wine, tissue extracts, or tissues including blood, muscle, brain, etc. are often dominated by the signal from a single component – water. This can interfere with the detection and quantification of signals from metabolite MOIs when the dynamic range of the NMR receiver is limited, when their concentrations are <0.1% of water, and/or when they are obfuscated by broad side-wings or intense motion artifacts propagating from the water signal. Signal from mobile lipid ($-CH_2-$ and $-CH_3$) moieties from fat can also be problematic in ^{1}H and ^{13}C spectra.

The problem is countered by 'solvent suppression,' 'water suppression,' and fat suppression or 'fat saturation' techniques that include the following.

1.4.4.1 T_1 Discrimination

The spectroscopy sequence is preceded by an inversion pulse applied at time TI equal to 0.693 times the T_1 of the water or lipid resonance to be suppressed, in accordance with the T_1-null method (see Section 1.2.3.2). Note that the MOI signal will also be modulated according to equation (1.14) and its own T_1s.

1.4.4.2 T_2 Discrimination

If the unwanted resonances have shorter T_2s than the moieties of interest they can be suppressed with a long-TE SE sequence (see Section 1.2.3.3). Note that the MOI signals will also be attenuated by their own T_2s via the factor $\exp(-T_2/\mathrm{TE})$.

1.4.4.3 Chemical-selective Irradiation of the Unwanted Peak

In the homonuclear decoupling experiment (see Section 1.4.3), an unwanted coupled resonance was eliminated by applying a B_1 field precisely tuned to saturate the resonance. The same saturation technique can be used to eliminate any undesirable peak in the spectrum. The simplest approach is a low-level c.w. B_1 signal applied throughout the experiment. Because saturation depends on T_1, B_1 can be turned off during acquisition if $\mathrm{tAQ} \ll T_1$ of the peak being suppressed, to avoid interactions between the c.w. transmission and reception.

Applying c.w. RF for more than several tens of milliseconds can be problematic for performing MRS on modern MRI scanners whose RF transmitters are often limited to short intense pulses. However, because the FT of a square excitation band in frequency space is equal to a 'sinc pulse' of the form $\mathrm{sinc}(t) = \sin t/t$ in the time domain, applying a sinc-modulated RF pulse whose excitation frequency is centered on the undesired resonance can selectively excite a

square frequency band with the undesired resonance at its center. In practice, the sinc function, which is infinite with decaying side-lobes symmetrically displaced about an intense central lobe, must be truncated – usually at a zero crossing. A symmetric sinc($n\pi t/\tau$)-modulated RF pulse truncated to a total of n zero crossings (including the two ends) has a total of $\{n-1\}$ positive plus negative lobes, a central lobe of duration $2\tau/n$ (zero-to-zero crossing) and excites an FWHM BW of $\Delta\nu = n/\tau$ for $\alpha \leq 90°$.[28] $\Delta\nu$ must generally be adjusted to avoid excitation of the MOI.

In the strict sense, in order to 'saturate' the unwanted resonance, the pulse must be applied for periods longer than T_1. A simpler approach is to apply just one-to-three of these prepulses before regular MRS excitation with an FA $= \alpha°$ pulse. The FAs of the chemical-selective pulses are adjusted so that the unwanted resonance generates no transverse magnetization. For example, with just a single suppression prepulse of FA $= \{180° - \alpha°\}$, the unwanted resonance will be inverted after the $\alpha°$ pulse is applied. It thus can contribute no M_{xy}. Meanwhile, the MOI signal is left untouched.

The sinc function is only one of many modulation functions that can be used to modulate RF pulses for the purpose of selectively exciting limited portions of an NMR spectrum. For example, a symmetric pulse of duration τ modulated by a Gaussian function of form $f_G(t) \sim \exp\{-2(\pi\sigma t)^2\}$ [the FT conjugate of equation (1.19)] truncated at ~10% of its amplitude excites a Gaussian-shaped band in the frequency domain with an FWHM of about $1.14/\sqrt{\tau}$ Hz,[28] or 36 Hz for a 1 ms pulse. Even the conjugate of the sinc pulse, the simple square-modulated time-domain pulse of duration τ used extensively in earlier sections, has a finite bandwidth: a sinc-modulated frequency response with an FWHM[28] of $1.21/\tau$. This must be remembered when using them for exciting large chemical shift dispersions.

1.4.4.4 Chemical-selective Excitation of the MOIs

The converse version of the method in Section 1.4.4.3, is to avoid exciting the unwanted resonance at all. In this case, the center frequency of the selective excitation pulse, say an $\alpha°$ sinc-modulated RF excitation pulse, is shifted and its excitation width adjusted to accommodate the BW of the spectrum of interest. Portions of the spectrum lying outside of the excitation window are unexcited, and therefore suppressed accordingly. Because the region of interest is now directly excited by the chemical-selective excitation pulse and hence is modulated by its excitation spectrum, unmodulated square or Gaussian pulses are far less desirable than sinc and related tailored pulse modulations from the standpoint of introducing spectral distortion.

1.4.4.5 NMR Filtering Employing Selective Spin Coupling or Editing

The T_1 relaxation and coupling properties of nuclear spins can also be used to target and distinguish an MOI from background signals that do not participate in such coupling. Typically, the NMR signal from the MOI is observed with and without selective NMR irradiation of the moiety that is coupled to it, analogous to homonuclear decoupling in Section 1.4.3. This is primarily used for targeting moieties on specific metabolites against a background milieu of other metabolites and will be treated later under 'spectral editing' (see Chapter 31).

1.5 SIGNAL-TO-NOISE RATIO (SNR)

1.5.1 Definition and Dependencies

The SNR is arguably *the* most critical determinant of NMR success. In MRS, it is defined as the signal height of the absorption mode (in-phase) component of the circularly polarized signal, divided by the RMS noise (see Section 1.2.2.1), as detected by the NMR spectrometer. Signal height, S_p, is actually the easier of the two to measure, the main complication being the determination of the baseline offset, S_b, at the location of the peak, in the presence of rolling baseline artifacts or overlapping resonances that are all too common in vivo. The RMS noise, v_n, must be determined from a region of spectrum devoid of signal and baseline artifacts and is preferably acquired with the sample in the spectrometer using the same settings as for S_p, but with the excitation turned off. At the very least, when determining signal and noise from the same spectrum spectral artifacts must be removed otherwise the true SNR can easily be underestimated manyfold. If the mean of the noise $\overline{v_n} \neq 0$ is offset, it should be subtracted from v_n as well. Thus,

$$\mathrm{SNR} = \frac{(S_p - S_b)}{(v_n - \overline{v_n})} \tag{1.29}$$

Table 1.3. Dependence of SNR on experimental and detection system parameters

Parameter	Number of nuclei (V, ml)	B_0 strength (T)	B_0 uniformity (ppm)	Averages, N	BW	Coil size, a	Loaded coil Q_L	Noise figure NF (in dB)	Temperature, T (in K)
SNR varies as:	Linearly	${B_0}^1$ to ${B_0}^2$	~Linearly	$\sqrt{N}$	$1/\sqrt{\mathrm{BW}}$	$\sim a^{-3/2}$	$\sqrt{Q_L}$	$10^{(\mathrm{NF}/20)}$	$1/\sqrt{T}$

A rough estimate of SNR also obtains by taking 2.5 times the peak height divided by the maximum peak-to-peak variation in the noise.

The SNR depends on the MOI concentration, the strength and homogeneity of the main field B_0, NMR pulse sequence parameters such as signal averaging (signals add $\propto N$ while random noise adds $\propto\sqrt{N}$: see Section 1.3), receiver BW setting, and other instrumental factors in accordance with Table 1.3.[1,29–32]

1.5.2 Calculation of SNR

Modern numerical methods make the calculation of absolute SNR possible.[32,33] The computation relies on the 'Principle of Reciprocity', which relates the sensitivity of a detector to a small subvolume ΔV of magnetic dipole sources at some location p, to the signal detected at p when a virtual unit current is applied to the coil.[1,29] From Faraday's Law applied to $M(t) \sim \exp(i\omega_0 t)$ from the Section 1.3, the signal voltage is:

$$S(t) = \mathrm{d}\{\mathbf{M} \cdot \mathbf{B_{10}} \Delta V\}/\mathrm{d}t = \omega_0 M \cdot |B_{10}| \Delta V \quad (1.30)$$

where $|B_{10}|$ is the magnitude of the circularly polarized transverse magnetic field $\mathbf{B_{10}}$, generated by the detector excited with unit current [analogous to equation (1.7)].

The noise voltage is given by the Nyquist formula[34]:

$$v_\mathrm{n} = \sqrt{4KTR_\mathrm{L}\mathrm{BW}} \quad (1.31)$$

where R_L is the resistance of the detector loaded with the sample at $\omega_0 \cdot R_\mathrm{L}$ is usually decomposed into contributions from the sample and detector coil, $R_\mathrm{L} = R_\mathrm{coil} + R_\mathrm{sample}$. T is the temperature of the load's dominant noise source. At equilibrium, the ^{1}H nuclear magnetization of a milliliter of water in a field of B_0 tesla at 37 °C (310 K) is[1]

$$\begin{aligned} M_0 &= N_\mathrm{ml} v_0^2 h^2 I(I+1)/3\,\mathrm{KT} \\ &= 3.111 \times 10^{-9} \times B_0\,\mathrm{J \cdot T^{-1} \cdot ml^{-1}} \end{aligned} \quad (1.32)$$

Dividing equation (1.30) by (1.31), the SNR per milliliter is thus:

$$\mathrm{SNR} = \frac{\sqrt{2}\omega_0 M |B_{10}|}{\sqrt{4KTR_\mathrm{L}\mathrm{BW}}} \times 10^{-\frac{\mathrm{NF}}{20}} \quad (1.33)$$

with the $10^{-\mathrm{NF}/20}$ term added to account for losses in the NMR spectrometer, as indexed by the NMR system's noise figure (NF) measured in decibel.[31] The $\sqrt{2}$ accounts for the circular polarization of the NMR signal (see Section 1.2.2.1), and is removed for linear detectors.[32]

Solving equation (1.33) boils down to calculating $|B_{10}|$ and $\sqrt{R_\mathrm{L}}$, as the rest of the equation involves substituting constants, and any differences between M and M_0 due to the various NMR pulse sequences are easily accommodated via equations (1.8), (1.9), (1.12), (1.14), (1.16), etc. $|B_{10}|$ is fairly easily calculated from the NMR detector's known current conductor locations and Biot–Savart's law, for example.[35] Typically, R_L is determined numerically for the ideal case of negligible system noise (NF = 0) and coil noise ($R_\mathrm{coil} = 0$), based on the RF electrical properties of the sample (conductivity σ; dielectric constant ε) using:

$$R_\mathrm{sample} = \sigma \int_\mathrm{sample} |E(r)|^2 \mathrm{d}V \quad (1.34)$$

where $|E(r)|$ represents the magnitude of the RF electric field generated by unit current, which is integrated over the sample volume V. Commercial numerical electromagnetic (EM) software engines are available to perform both the $|B_{10}|$ and R_L computations by breaking up the volume into tiny elements to solve discretized versions of Maxwell's equations.[32,33]

The SNR that obtains for the 'ideal detector' with negligible system and coil noise is called the 'intrinsic signal-to-noise ratio' or 'ISNR', as it is attributable to sample losses only. This is the best possible SNR realizable for the chosen configuration of coil or detector conductors.[31] However, the application of such software engines can be extended to determine the 'ultimate intrinsic signal-to-noise ratio (UISNR)'.[36]

Basically, the locations of the current sources that generate $|B_{10}|$ are iteratively adjusted on the surface of a model sample, to numerically optimize the SNR in a region of the sample. The UISNR is the best SNR that can be obtained by any coil design.[36]

1.5.3 Detectors and B_0 Dependence

Obviously, detector performance plays a key role. Generally, it is desirable to localize the MRS signals to subvolumes, ΔV, of interest in the sample using methods such as those described in later chapters. Because the detector receives both signal and noise voltages without discrimination, an optimal detector should primarily be spatially sensitive only to the signal and the noise from ΔV and not detect extraneous noise from regions outside of ΔV. This argues for detector coils whose dimensions are matched to the location and size of the subvolumes, such as loop detectors with diameters about equal to the depth and extent of interest.[33,35]

The detector should contribute negligible thermal electrical noise to the spectrum from its own resistive losses.[29,30] The detector is invariably tuned via a resonant circuit to the NMR frequency, ν_0, in order to maximize the amplitude of the induced signal voltage that is conveyed to the NMR spectrometer's voltage preamplifier. The coil's unloaded quality factor, $Q_E = \{\omega L/R_{coil}\}$, is a measure of the coils own resistive losses, as well as the sharpness of the resonant circuit. The tuning circuit also matches the resistance of the detector at resonance, to the input impedance of the preamplifier at which its NF is minimum, using minimal-loss reactive elements (see Chapter 2).

When a biological sample – a human subject, animal, a biological sample, etc. – is placed in the coil, the quality factor, Q, decreases to $Q_L = \{\omega L/R_L\} = \{\omega L/(R_{coil} + R_{sample})\}$.[30] For the ideal detector then, $Q_L \ll Q_E$. However, caution is necessary. A low Q_L or high R_L is detrimental to SNR regardless (Table 1.3) and can also arise from unnecessary direct electrical coupling between the detector and the sample in non-ideal designs. This is often manifest as changes in the detector's resonant frequency when it is loaded with the sample, and such losses can often be ameliorated by superior detector design such as those that distribute the tuning elements throughout the detector's structure.

1.5.3.1 The Intrinsic SNR

Equation (1.33) contains several factors whose B_0 dependence must be parsed when considering the SNR benefits of higher NMR field strengths. On the signal side, replacing ω_0 in equation (1.30) by$\{\gamma\ B_0\}$ from equation (1.1) and noting $M \propto B_0$ as well [see Section 1.1.2 and equation (1.32)], we have $S(t) \propto {B_0}^2$. Then, from equation (1.31) for the noise,

$$\mathrm{SNR} \propto \frac{{B_0}^2}{\sqrt{R_L}} = \frac{{B_0}^2}{\sqrt{R_{coil} + R_{sample}}} \tag{1.35}$$

For external detectors, R_{coil} is proportional to the reciprocal of the RF skin depth,[27,28] $\delta = \{2\rho/(\mu_c\omega_0)\}^{1/2}$ for a coil made of conductor of resistivity ρ and permeability μ_c. Thus, $R_{coil} \propto \sqrt{\omega_0}$. The losses contributing to R_{sample} in equation (1.34) are primarily inductive[30,31] and vary as ${\omega_0}^2$. Therefore, after converting the R dependencies in ω_0 into B_0 dependencies, equation (1.35) becomes:

$$\mathrm{SNR} \propto \frac{{B_0}^2}{\{(1 - a_c){B_0}^2 + a_c{B_0}^{1/2}\}^{1/2}} \tag{1.36}$$

where a_c is introduced as a measure of the fraction of the noise contributed by the detector.[30,31] The case of $a_c = 0$ corresponds to the ideal zero-noise detector with SNR equal to the ISNR, which scales only linearly as B_0 (Figure 1.12).[31] If $a_c = 1$, coil noise is dominant and SNR scales as $\sim {B_0}^{7/4}$ (Figure 1.12).[29]

Caution is warranted when using equation (1.36) to predict performance at one B_0 based on the SNR measured at another. The expression is a proportionality so everything else must be the same for any comparison: this means BW, coil design, coil size, B_0 homogeneity, pulse sequence parameters, etc. In addition, coil designs optimized for one B_0 may be ill-suited for another B_0, especially if the comparison involves a large difference in B_0. For example, the change from 0.3 to 1.5 T prompted the invention of the birdcage coil.[12] In addition, as coil size is reduced to improve SNR by minimizing the noise detected from remote locations (a in Table 1.3), it becomes increasingly difficult to achieve the sample-dominant noise condition because relative losses in coil conductors, solder joints, and tuning capacitors mount.[37] Although one is rewarded by $a \sim {B_0}^{7/4}$ SNR dependence, the SNR gained from operating in the coil-noise dominant 7/4th power regime is still less than what it would be without the coil noise (Figure 1.12). An extreme case perhaps is that of tiny internal coils that employ the body as a return path.[32] These can behave like antennae in lossy

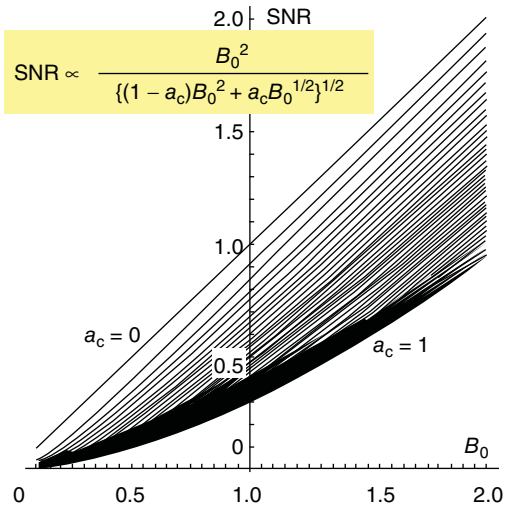

Figure 1.12. Dependence of SNR on B_0 according to the proportionality of equation (1.36), as a function of the relative contributions to the noise from the sample and the coil ($0 \leq a_c \leq 1$; 2% steps; arbitrary units)

media whose noise is dominated by sample electrical losses. In this case,[32] R_L in equation (1.35) may be essentially constant with B_0, resulting in an SNR $\propto B_0^2$ as the best that can possibly be done for the design, but less than the UISNR that would result without these losses.[38]

Because the change in Q_E and Q_L is a measure of the change in the relative load resistances in equation (1.35), the ISNR can be determined from a regular SNR measurement via:

$$\mathrm{ISNR} = \frac{\mathrm{SNR} \cdot 10^{\mathrm{NF}/20}}{(1 - Q_L/Q_E)^{1/2}} \tag{1.37}$$

with the NF term accounting for losses in the NMR spectrometer as in equation (1.33).[31] In practice (and detailed more generally in Chapter 2), NF can be measured by replacing the NMR coil by a thermally stable 50 Ω resistor at the system's preamplifier input, and acquiring a spectrum at room temperature (RT), with no RF excitation.[39] A measurement of v_{nRT} is made from the unfiltered spectrum. The resistor is dunked in liquid nitrogen at $T = 77$ K, and the noise measurement repeated to obtain v_{n77}. Basically, the larger the decrease in v_{n77}, the more sensitive the scanner is to thermal noise – in this case, the resistor's noise – and the lower the NF. NF at RT may be calculated from[1]

$$\mathrm{NF} = 10\log[1 - 77/\mathrm{RT}] - 10\log[1 - (v_{\mathrm{nRT}}/v_{\mathrm{n77}})^2] \tag{1.38}$$

the plot in Figure 1.13,[39] or the more generalized form of equation (1.13) given in Chapter 2.

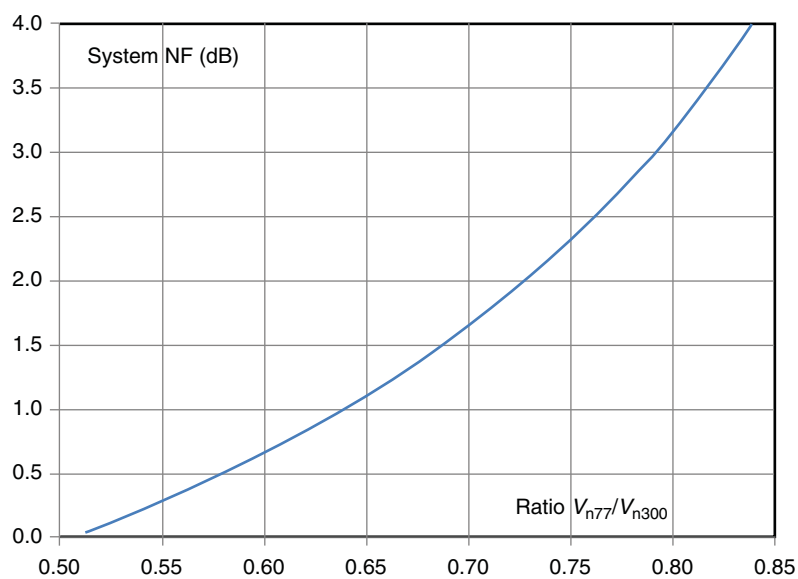

Figure 1.13. Measurement of the system noise figure (NF) from the ratio of noise voltages from a 50 Ω resistor in liquid nitrogen to that at 300 K (27 °C), at the system's preamplifier input, according to equation (1.38) for ratios of about 0.5–0.85[39]

1.5.4 SNR Limits In Vivo

The primary factor limiting SNR in vivo is the concentration of the chemical moiety, or N_{ml}. As already noted (see Section 1.1.1), ^{1}H nuclei far outnumber other nuclei in living tissue, amounting to about two-thirds of them. About two-thirds of the protons are in endogenous water moieties,[2] whereas the rest of the protons mostly reside in various organic molecules that make up the body. Of the latter, fat is probably the most abundant, accounting for perhaps 22% of the proton pool.[2] Then, there is a *sensitivity gap* between the water and fat signals and those of other MOIs detectable by ^{1}H NMR, which are present at much lower concentrations. The current limit to practical detection by NMR or MRS is about 10^{-6} of that of ^{1}H signal from water. Most endogenous metabolites that are NMR-visible are in the 1–10 mM concentration range: about $\sim 10^{-5}$ of that of ^{1}H in water. Non-^{1}H NMR is further compromised by reduced sensitivity, isotopic abundance, and SNR relative to ^{1}H (Table 1.1). One may query how can they be seen at all? The answer draws on Table 1.3. The SNR for tissue water ^{1}H is of the order 100 $\sqrt{\text{Hz}}$/μl per FID. Averaging 100 FID's from a much larger volume–say 10 ml (vs 1 μl), and reducing BW 16-fold can more than compensate for the loss (since $10^4\sqrt{\{100\times 16\}} = 4\times 10^5$).

Note that highly bound substances such as membrane lipids with short T_2s (or very broad linewidths) whose signals have decayed by the time of the acquisition window will be 'NMR invisible'. In addition, NMR or MRS can be performed on nonendogenous compounds containing NMR nuclei such as fluorine (^{19}F), or ^{13}C-enriched compounds, including those that are hyperpolarized (see Chapters 33, 39, and 40). However, our ability to see hyperpolarized nuclei will still depend on what concentration can be introduced, as well as how much hyperpolarization is retained.

What can be seen in vivo with MRS will be reviewed in forthcoming chapters and appendices 1–4 and 7, but here is a brief preview.[40]

1.5.4.1 Fat and Lipid Metabolism

Fatty acids with $-CH_2-$ resonances are sufficiently concentrated to be imaged directly by 'chemical selective' ^{1}H MRI using techniques analogous to those discussed in Sections 1.4.4.3 and 1.4.4.4. They are also visible in natural abundance ^{13}C MRS (Figure 1.11).[27] Phospholipid membrane components such as phosphorylethanolamine and phosphorylcholine are precursors to brain myelin and appear as a phosphomonoester (PM or PME) resonance in ^{31}P spectra. Breakdown products, glycerophosphorylethanolamine, and glycerophosphorylcholine appear as phosphodiester (PD or PDE) peaks in ^{31}P MRS.

1.5.4.2 Energy Metabolism

Adenosine triphosphate (ATP) is the fundamental energy currency of the body. Short-term energy is produced by conversion of ATP into adenosine diphosphate (ADP) and inorganic phosphate (Pi):

$$\text{ATP}^{\S} \Longleftrightarrow \text{ADP} + \text{Pi}^{\S} + \text{energy}$$

In brain and muscle (skeletal and heart), ATP is resupplied from phosphocreatine (PCr) via the creatine kinase (CK) reaction:

$$\text{PCr}^{\S} + \text{ADP} \Longleftrightarrow \text{ATP}^{\S} + \text{creatine}^{\P}$$

and also from

$$\text{Glycogen}^{\#} + \text{Pi}^{\S} + \text{ADP} \Longleftrightarrow \text{ATP}^{\S} + \text{lactic acid}^{\#\P}$$

Long term aerobic energy sources include:

$$\text{glucose}^{\#\P}, \text{glycogen}^{\#\P} + \text{ATP}^{\S} + \text{Pi}^{\S} + \text{O}_2 \Rightarrow \text{ATP}^{\S} + \text{H}_2\text{O} + \text{CO}_2$$

$$\text{fatty acids}^{\#\P} + \text{ADP} + \text{Pi}^{\S} + \text{O}_2 \Rightarrow \text{ATP}^{\S} + \text{H}_2\text{O} + \text{CO}_2$$

Glycolytic metabolism converts 1 mole of glucose into lactate to make 2 moles ATP, whereas its complete combustion via the citric acid cycle makes 36 moles of ATP:

$$\text{glucose}^{\#\P}, \text{pyruvate}^{\#\P} \Rightarrow \text{lactate}^{\#\P} + \text{ATP}^{\S}$$

$$\text{amino acids, carbohydrates, fats}^{\#\P}, \text{glucose}^{\#\P}, \text{pyruvate}^{\#} \Rightarrow \text{acetylcoenzyme A}$$

$$\text{acetylcoenzyme A} \Rightarrow \alpha\text{-ketoglutarate} \Rightarrow \text{glutamate}^{\#\P} \Longleftrightarrow \text{glutamine}^{\#\P}$$

$$\text{acetylcoenzyme A} \Rightarrow \text{oxaloacetate} \Longleftrightarrow \text{aspartate}^{\#\P}$$

1.5.4.3 Neuroexcitation and Inhibitory Metabolites

Glutamate, aspartate, and gamma-aminobutyric acid (GABA; derived from glutamate) are detectable by brain ^{1}H MRS, as is n-acetyl aspartate, whose specific

---

§Detectable by ^{31}P MRS.
¶Detectable by ^{1}H MRS.
$^{\#}$Detectable by ^{13}C-enriched MRS (including enhanced polarization methods).

biochemical function remains unclear even though it is often referred to as a 'neuronal marker'.

RELATED ARTICLES IN EMAGRES

Fourier Transform Spectroscopy

Spatial Localization Techniques for Human MRS

Carbohydrates and Glycoconjugates

Whole Body Studies Involving Spin-Lattice Relaxation in the Rotating Frame

Metabolite Quantification in MRS and Pattern Recognition

Development of NMR: Biological and Medical MR Spectroscopy

Recent Progress in Clinical Magnetic Resonance Spectroscopy

Magnetic Shielding and Chemical Shifts: Basics

Dipolar and Indirect Coupling: Basics

REFERENCES

1. C. N. Chen and D. I. Hoult, Biomedical Magnetic Resonance Technology, A. Hilger: Bristol, New York, 1989, 120, 196, 309.
2. W. S. Snyder, M. J. Cook, E. S. Nasset, L. R. Karhausen, G. P. Howells, and I. H. Tipton, Report of the Task Group on Reference Man, Pergamon Press: Oxford, 1984, 296, 326, 281 International Commission on Radiological Protection No. 23.
3. E. M. Purcell, H. C. Torrey, and R. V. Pound, *Phys. Rev.*, 1946, **69**, 37.
4. F. Bloch, W. W. Hansen, and M. Packard, *Phys. Rev.*, 1946, **69**, 127.
5. P. C. Lauterbur, *Nature*, 1973, **242**, 190.
6. E. L. Hahn, *Phys. Rev.*, 1950, **80**, 580.
7. N. Bloembergen, E. M. Purcell, and R. V. Pound, *Phys. Rev.*, 1948, **73**, 679.
8. A. Abragam, The Principles of Nuclear Magnetism, Oxford University Press: Oxford, UK, 1978, 292.
9. P. A. Bottomley, T. H. Foster, R. E. Argersinger, and L. M. Pfeifer, *Med. Phys.*, 1984, **11**, 425.
10. P. A. Bottomley, C. J. Hardy, R. E. Argersinger, and G. Allen-Moore, *Med. Phys.*, 1987, **14**, 1.
11. F. Bloch, *Phys. Rev.*, 1946, **70**, 460.
12. C. E. Hayes, W. A. Edelstein, J. F. Schenck, O. M. Mueller, and M. Eash, *J. Magn. Reson.*, 1985, **63**, 622.
13. G. H. Glover, C. E. Hayes, N. J. Pelc, W. A. Edelstein, O. M. Mueller, H. R. Hart, C. J. Hardy, M. O'Donnell, and W. D. Barber, *J. Magn. Reson.*, 1985, **64**, 255.
14. C. N. Chen, D. I. Hoult, and V. J. Sank, *J. Magn. Reson.*, 1983, **54**, 324.
15. H. Y. Carr and E. M. Purcell, *Phys. Rev.*, 1954, **94**, 630.
16. S. Meiboom and D. Gill, *Rev. Sci. Instrum.*, 1958, **29**, 688.
17. D. Burstein, *Conc. Magn. Reson.*, 1996, **8**, 269.
18. P. A. Bottomley and W. A. Edelstein, Method of eliminating spurious FID due to imperfect 180° pulses in NMR imaging: the primer/crusher sequence, U.S. Patent 4,484,138; (Nov. 20, 1984).
19. R. R. Ernst and W. A. Anderson, *Rev. Sci. Instrum.*, 1966, **37**, 93.
20. W. G. Proctor and F. C. Yu, *Phys. Rev.*, 1950, **77**, 717.
21. J. T. Arnold, S. S. Dharmatti, and M. E. Packard, *J. Chem. Phys.*, 1951, **19**, 507.
22. W. E. Lamb, *Phys. Rev.*, 1941, **60**, 817.
23. N. F. Ramsay, *Phys. Rev.*, 1950, **78**, 699.
24. H. S. Gutowsky, D. W. McCall, and C. P. Slichter, *Phys. Rev.*, 1951, **84**, 589.
25. A. W. Overhauser, *Phys. Rev.*, 1953, **92**, 411.
26. T. R. Carver and C. P. Slichter, *Phys. Rev.*, 1953, **92**, 212.
27. P. A. Bottomley, C. J. Hardy, P. B. Roemer, and O. M. Mueller, *Magn. Reson. Med.*, 1989, **12**, 348.
28. M. A. Bernstein, K. F. King, and X. J. Zhou, Handbook of MRI Pulse Sequences, Elsevier: London, 2004, 37.
29. D. I. Hoult and R. E. Richards, *J. Magn. Reson.*, 1976, **24**, 71.
30. D. I. Hoult and P. C. Lauterbur, *J. Magn. Reson.*, 1979, **34**, 425.
31. W. A. Edelstein, G. H. Glover, C. J. Hardy, and R. W. Redington, *Magn. Reson. Med.*, 1986, **3**, 604.
32. A. M. El-Sharkawy, D. Qian, and P. A. Bottomley, *Med. Phys.*, 2008, **35**, 1995.
33. J. Wang, A. Reykowski, and J. Dickas, *IEEE Trans. Biomed. Eng.*, 1995, **42**, 908.

34. H. Nyquist, *Phys. Rev.*, 1928, **32**, 110.

35. P. A. Bottomley, C. H. Lugo-Olivieri, and R. Giaquinto, *Magn. Reson. Med.*, 1997, **37**, 591.

36. O. Ocali and E. Atalar, *Magn. Reson. Med.*, 1998, **39**, 462.

37. A. Kumar, W. A. Edelstein, and P. A. Bottomley, *Magn. Reson. Med.*, 2009, **61**, 1201.

38. H. Celik, Y. Eryaman, A. Altintas, I. A. Abdel-Hafez, and E. Atalar, *Magn. Reson. Med.*, 2004, **52**, 640.

39. P. A. Bottomley, in Medical Magnetic Resonance Imaging and Spectroscopy, a Primer, eds T. F. Budinger and A. R. Margulis, Society for Magnetic Resonance in Medicine: Berkeley, CA, 1986, 81.

40. P. A. Bottomley, *Radiology*, 1989, **170**, 1.

Chapter 2

Magnetic Resonance Spectroscopy Instrumentation

David Hoult

David Hoult Consulting Ltd., Winnipeg, Manitoba, Canada

2.1 INTRODUCTION

Instrumentation for performing biological nuclear magnetic resonance (NMR) spectroscopy (MRS) involves advanced technologies in the disciplines of cryogenics, electromagnetics, physics, mechanical engineering, radio-frequency (RF) electronics, digital interfacing, and computing. MR has challenged the best practitioners in each discipline and continues to do so in a way that is surprising for a technique that arose in the mid-twentieth century. In consequence, any author attempting to give an overview of that instrumentation can only give a hint as to the complexities that underlie much of it and so further reading material may be found at the end of the chapter. The main components of a biological MR system are shown in Figure 2.1 and we briefly examine their roles and how they determine the efficacy of almost any experiment. A basic knowledge of NMR is assumed (see Chapter 1). Other chapters contain additional details where pertinent. There may occasionally be electrical engineering terms with which some readers are unfamiliar. Fortunately, engineers have thoroughly embraced the Internet, and definitions should easily be found.

Handbook of Magnetic Resonance Spectroscopy In Vivo: MRS Theory, Practice and Applications.
Edited by Paul A. Bottomley and John R. Griffiths
 ISBN: 978-1-118-99766-6
Also published in eMagRes (online edition)
DOI: 10.1002/9780470034590.emrstm1450

2.2 THE MAGNETIC FIELD

2.2.1 Field Characteristics

2.2.1.1 Stability

Since the earliest days of NMR, there have been three overarching concerns regarding the main magnetic field B_0 – its strength, stability, and uniformity. Even the most naïve approach to signal strength analysis indicates that the bigger the field strength is, the bigger will be the signal, so the urge to build stronger and better magnets has ever been present, for in the grand scheme of spectroscopic techniques, NMR is very insensitive. In 1964, however, the introduction of the superconducting magnet by the Varian company altered forever the practice of magnetic resonance, for this innovation at a stroke doubled the available field strength to 4.7 T. The magnet was made with many turns of copper wire containing strands of a

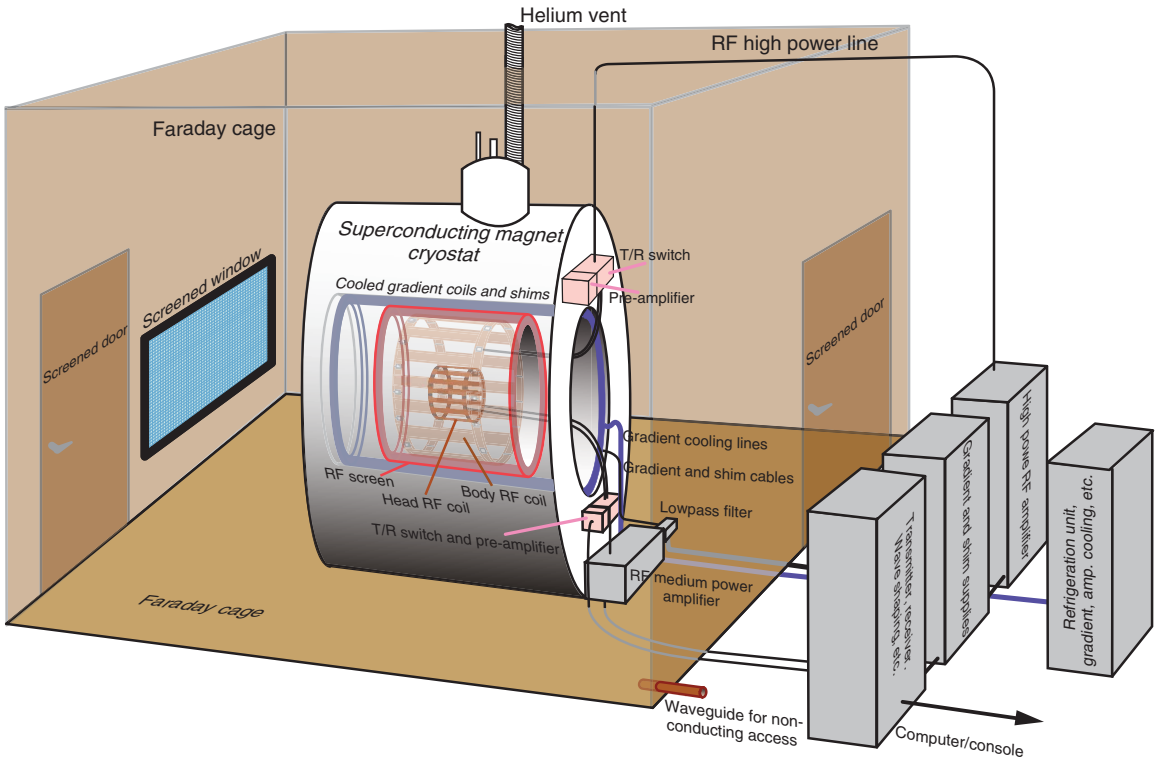

Figure 2.1. A conceptual drawing of a system for performing MR spectroscopy in animals and humans. The exact implementation naturally depends on the manufacturer and the work to be performed: some components in the figure may be redundant and/or additional components may be needed

niobium-tin alloy that sat in a cryostat or Dewar vessel holding liquid helium (4.2 K) and liquid nitrogen (77 K), and that accommodated 5 mm sample tubes. While it would take many more years for cryotechnology to deliver a magnet suitable for humans rather than test tubes, this advance was the precursor of nearly all future NMR systems. Once the magnet was energized, the dependence on a power supply was removed and this in turn removed the main source of field fluctuations, though they can still exist as a consequence of building vibration and rapid changes of field gradients.

It was soon discovered, however, that the fields of superconducting magnets were susceptible to changes of cryogen levels, the movement of nearby iron objects – elevators, buses, trains, etc. – and that imperfect superconductivity (usually in wire splices) also caused the field slowly to decay. Thus, a device that kept the field and Larmor frequency in unison over longer periods of time (seconds to days) was needed, and this was the 'field-frequency' lock.[1] Typically, the Larmor frequency of a secondary nucleus (usually deuterium, ^{2}H) was monitored by NMR, and if it departed from resonance, the field was corrected accordingly. This process is not quite as simple as it sounds, for it also implies that the frequency source used for the deuterium NMR experiment must precisely track that used for the main experiment: the two sources must both be derived from a common, high-stability master oscillator. It too can drift in frequency, so a field-frequency lock actually ensures that the field and frequencies drift in tandem. (A typical fractional stability of a crystal oscillator in a temperature-controlled oven is of the order of 10^{-9} per hour.) Note that while the original implementation was to restore the field strength, an alternative is to alter the frequencies. However, excessive frequency change ($\gtrsim$0.5 MHz) demands a change of 'probe' tuning (a probe is a transmitting or receiving coil with capacitors attached – see Chapter 3).

If the main NMR signal has a sufficiently large spectral component (e.g. water), a variant on the

field-frequency lock concept is occasional monitoring of the signal's frequency, followed by correction of field or frequency as necessary. Of course, if it is certain during the course of an experiment (usually a short one of a few minutes) that any field/frequency drift is negligible, locking/tracking can be dispensed with. In this regard, an advance in magnet technology has helped considerably.

The fringe fields surrounding large magnets are at best a nuisance and at worst a hazard, and so manufacturers have contrived to reduce these fields greatly, a practice commonly referred to as 'self-shielding'. However, if there is a magnetic disturbance at some distant point P, it can be shown that the resulting change in the magnet *current* is proportional to the fringe field at P. If this fringe field is small, then the effect on the magnet's current is small and the corresponding change in the field at the magnet's center is also small. Of course, the *total* change in field at the magnet center is the sum of the change due to the current and the field due directly to the disturbance itself, and after some early mistakes in this regard, magnets are generally designed so that the two effects are in opposition. Unfortunately, stability requirements are often greater for spectroscopy than for imaging, so when performing in vivo spectroscopic measurements on an imaging system, field stability should not be taken entirely for granted. If it is a problem, working at night sometimes helps, as external disturbances and building vibration tend to be less (see Chapter 3).

2.2.1.2 Homogeneity

Since the realization in 1951 that chemical spectra could be observed, a major concern has always been field homogeneity. A spectroscopic line originating from a chemical compound within a volume of interest ΔV has a natural linewidth δf determined by its molecular environment – typically in the range 3–300 Hz for biological samples. However, if the variation in B_0 field strength over ΔV is such that the variation in Larmor frequency is comparable to or greater than δf, the aggregate spectral line is broadened and its integral, a measure of the amount of compound, has reduced accuracy. Worse, adjacent spectral lines may not be resolved. The implication in a 4.7 T field is that a magnetic field inhomogeneity (error) of better than ~0.1 ppm is needed for 10 Hz resolution. (The exact specification depends on how the field error over the sample volume is described: peak-to-peak, root mean square, etc. Beware of the hiding of mediocre performance behind statistics.) Traditionally, the overarching sources of inhomogeneity in the magnetic field have been unavoidable errors in magnet construction coupled with structural distortions owing to gravity and the magnetic forces between windings. Before the advent of superconducting magnets, initial attempts to correct the problems involved the use of small pieces of metal (shims) behind and on electromagnet pole faces, and so the term 'shimming the magnet' was born as a descriptor for improving the field homogeneity.

In 1958, Marcel Golay proposed a better method that was mathematically based. First, magnetic fields are traditionally assigned to the z direction in a Cartesian frame and the divergence of field associated with even a very large inhomogeneity (e.g., one part per thousand) produces only tiny fields B_x and B_y in the x and y directions. Now the MR system responds to the *magnitude* B_0 of the field, so

$$\begin{aligned} B_0 &= \sqrt{B_x^2 + B_y^2 + B_z^2} \\ &= B_z\left(1 + \frac{B_x^2}{2B_z^2} + \frac{B_y^2}{2B_z^2} + \cdots\right) \cong B_z \end{aligned} \quad (2.1)$$

and for all practical purposes, B_0 and B_z are synonymous. Second, the magnetic field in the air inside an empty magnet bore can be shown to obey Laplace's equation

$$\nabla^2 B_z \equiv \nabla^2 B_0 = 0 \quad (2.2)$$

Golay realized that the solutions of this equation formed an orthogonal basis for analyzing inhomogeneity: the field could be expressed as a sum of solutions. Given the circular symmetry of both electromagnet pole faces and superconducting magnet bores, the use of a cylindrical coordinate system would seem to be an obvious choice; however, a drawback is that the boundaries then determine the solutions – the latter change with sample size. Accordingly, Golay worked in spherical polar coordinates (r, θ, φ) and proposed that the field be analyzed in spherical harmonics U_{nm} and V_{nm}, namely

$$\begin{aligned} B_0 &= \sum_{n=0}^{\infty}\sum_{m=0}^{n} F_{nm}U_{nm} + G_{nm}V_{nm}; \\ U_{nm} &= r^n P_{nm}(\cos\theta)\cos m\varphi \\ V_{nm} &= r^n P_{nm}(\cos\theta)\sin m\varphi \end{aligned} \quad (2.3)$$

where F_{nm} and G_{nm} are constants, integer n is the order of the field, m is the degree ($m \le n$), and the P_{nm} are the associated Legendre polynomials in $\cos\theta$. In practice,

the order n typically needs to run to no more than 4 or 5 to ensure an excellent description of the field. The form of the solution is unchanged with sample size, but the spherical harmonics are only orthogonal for a spherical sample *centered on the origin*. This methodology at first sight appears formidable; however, in practice, it is not, as n need not be large and the associated Legendre polynomials are then relatively simple. The harmonics are sometimes expressed in Cartesian coordinates (for example, $U_{22} = 3[x^2 - y^2]$), but this notation obscures the symmetries inherent in the spherical description.

Golay continued by proposing the winding of 'shim coils', each of which would produce a relatively pure spherically harmonic field of order n and degree m, up to some limiting value $n_{\max}$. By appropriate adjustment of the currents in the coils, the field of equation (2.3) could then be 'shimmed' by cancelling the various spherical harmonics comprising the inhomogeneity. (As $P_{00} = 1$, the 'zeroth-order' field U_{00} is the main homogeneous field.) Golay coils originally comprised arcs and legs of current having specific coordinates but today, distributed designs (c.f. Figure 2.3) that aim to minimize power dissipation are also used. Because dissipation and the effects of winding errors increase dramatically with increasing order, it is rare to find coils with order $n > 4$.

To find the correct coil currents, there are broadly two methods: (i) map the inhomogeneous field by imaging methods or with the aid of a movable tiny NMR sample, analyze the map in spherical harmonics and knowing the characteristics of the shim coils, apply the appropriate currents; (ii) use a metric of the field homogeneity, such as the signal from a free induction decay or the height of a spectral line from a bulk sample, and maximize the metric by systematic adjustment of the shim coil currents. The latter method requires skill and experience if applied manually (as well as a signal with good sensitivity, which with biological samples implies ^{1}H), as it is possible to be trapped in local maxima that do not represent the best homogeneity attainable. It is therefore common nowadays to delegate such shimming to the computer, which can employ a global maximization algorithm (Nelder–Mead, simulated annealing, etc.) to reduce (but not eliminate) the risk of such entrapment.

Another method of shimming involves the use of optimally placed pieces of steel on the magnet bore wall or in the cryostat. While this so-called 'passive shimming' technique is quite potent, it is static and difficult to change. Golay's approach is therefore preferred for fine adjustable shimming, as it is flexible and can accommodate minor changes in the homogeneity, no matter the cause. It has, however, two serious drawbacks when we consider in vivo localized spectroscopy: (i) the spherical harmonics are orthogonal only over a spherical region centered on the origin, but the volume of interest in a person or animal is typically not spherical and not at the origin; (ii) Laplace's equation (2.2) is invalid if the magnetic susceptibility χ of the sample is dependent on spatial position $\mathbf{r}$ and thereby causes a significant spatial variation of field strength in comparison to the linewidth.

Consider first the question of position. Let the center (or origin) of the volume of interest be O′, some distance removed from the shim set's origin O. Neglecting variations in χ, the magnetic field in the vicinity of O′ can always be analyzed in spherical harmonics, but the further O′ is from O, the more the coefficients F'_{nm} and G'_{nm} will differ from F_{nm} and G_{nm}. Worse, the field from a shim coil, a relatively pure harmonic when measured about origin O, will in general be contaminated with all harmonics of orders and degrees less than n and m respectively when analyzed about origin O′: the further O′ is from O, the greater will be the contamination. The resulting lack of orthogonality makes it virtually certain that local, rather than global, maxima will be attained with manual shimming; the risk thereof with algorithmic shimming is also increased. A simple one-dimensional example helps in clarifying this statement, as shown in Figure 2.2. Shimming manually with first the U_{10} (z) shim, the inhomogeneity is reduced over the region of interest to a minimum of 2.25 ppm, as shown in Figure 2.2b, blue line. (Note the large mean field change in going from Figure 2.2a to b, a prime warning sign of orthogonality problems.) Next, we turn to the U_{20} (z^2) shim, but it cannot improve the inhomogeneity, as is also true of the U_{30} (z^3) shim. We have been ensnared by a local maximum because in the region about $z = 3$, both z^2 and z^3 shims produce respectively dominant 9 z and 27 z variations. (The correct shim was actually $-1.0\ z^3$.) For a number of years, it was therefore conventional wisdom that one should only use the first-order shims for in vivo spectroscopy. However, if the coordinates of the center of the region of interest are known and the shims are computer controlled, the computer can reorthogonalize the shim system: the user adjusts, for example, z^3, but the computer is actually adjusting z and z^2 as well, for $(z-3)^3 = -27 + 27z - 9z^2 + z^3$. Even with algorithmic shimming, reorthogonalisation speeds the shimming

process. Notwithstanding, it is always best to position the volume of interest as close to the origin as possible; if nothing else to ensure that shims do not encounter their limits of current.

When the cause of inhomogeneity is the sample itself, we tend to be limited in what we may accomplish. The relevant differential equation is of the form [c.f. equation (2.2)]

$$(1 - \chi[\mathbf{r}])\nabla^2\mathbf{B}[\mathbf{r}] + \mathbf{O}[\mathbf{r}] = 0 \qquad (2.4)$$

where the remainder **O** is complicated. This equation is generally insoluble. A constant **B** field of amplitude B_0 reduces the term in **B** in equation (2.4) to zero, but it may be shown that the remainder is then given by

$$\mathbf{O}[\mathbf{r}] = B_0 \left[\frac{\partial^2\chi}{\partial x \partial z}, \frac{\partial^2\chi}{\partial y \partial z}, -\frac{\partial^2\chi}{\partial x^2} - \frac{\partial^2\chi}{\partial y^2} \right]$$

As this vector is not zero, we conclude that equation (2.4) cannot be satisfied by a homogeneous field and therefore, in general, a homogeneous field cannot be obtained. The volume susceptibility of organic material is usually of the order of -10^{-5}, whereas that of air is close to zero. It follows that when a region of interest includes an air-filled cavity, it can suffer considerable inhomogeneity. Even if the tissue is itself homogeneous but is *close* to an air-filled cavity (e.g., the sinuses), the field in the tissue may comprise orders higher than those for which shims are available. In conclusion, while magnet design is incomparably better than in the early days of NMR, in vivo spectroscopy presents challenges for which progress is difficult.

2.2.2 Gradients

The use of transient magnetic field gradients, which temporarily cause field B_0 to vary linearly with distance x, y, or z, is fundamental to both imaging and localized spectroscopy and at first sight, their production appears to be simple: they merely require very powerful first-order Golay coils. Referring to equation (2.3), as $P_{10}(\cos\theta) = \cos\theta$ and $P_{11}(\cos\theta) = \sin\theta$, $U_{10} = z$, $U_{11} = x$ and $V_{11} = y$. However, numerous problems arise because the gradients are both powerful and transient. We require them for times very much less than T_2 and so they must turn on and off quickly; when present, they must be stable and accurately known; once off, the main field should have no memory of their former presence.

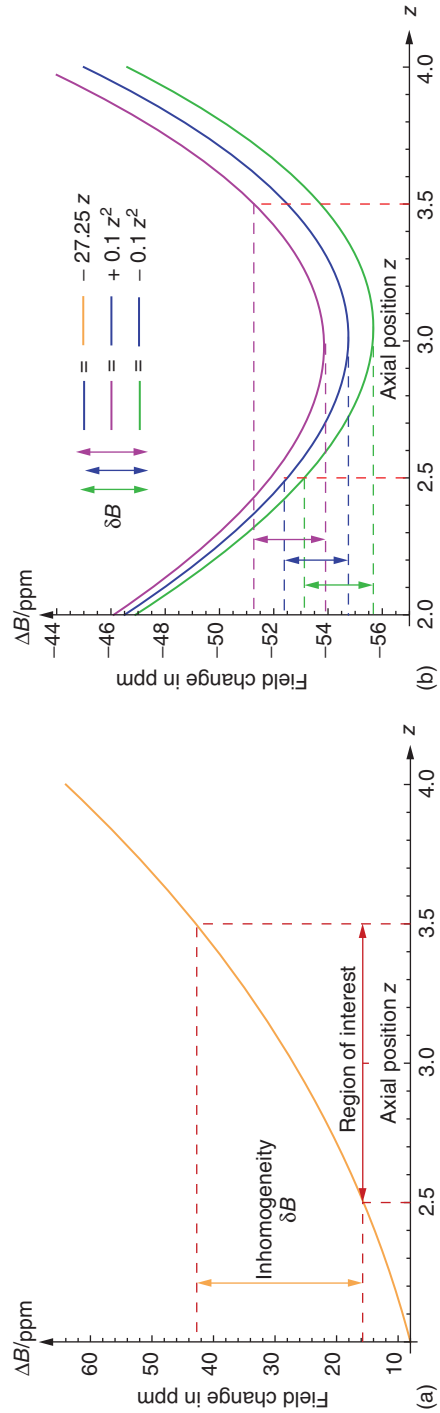

Figure 2.2. One-dimensional example of entrapment in a local maximum. In (a) a field variation over a region of interest remote from the origin is shown. In (b) the field variation obtained by optimally adjusting the z shim is shown (blue line). Counterintuitively, adjustment of the z^2 shim (green and magenta lines) degrades the homogeneity because the region of interest is not centered on the origin

These problems can roughly be divided into two categories: the effects of the gradients on the magnet and shim coils and *vice versa* and the design of suitable power supplies.

Any simple gradient coil has mutual inductance M with conductors in close proximity, and conductors abound in the magnet windings, the cryostat, shields, the shim coils, the other gradients, and the RF transmitting and receiving coils. When the current I through a gradient coil changes, an electromotive force $E = M\,\mathrm{d}I/\mathrm{d}t$ is induced in a nearby conductor and unless steps are taken to stop it, current flows: this immediately changes the main magnetic field. The nearest conductors such as the cryostat are not superconducting, so the so-called *eddy currents* eventually die away (typically exponentially), the times taken being dependent on the conductors' positions, resistivities, and geometry.

Whenever two conductors have currents flowing, there is a mechanical force between them (in general, both linear and torque) and if one of the currents changes, so does the force. Rapid change of current thus creates an impulse that can cause vibration of the magnet, of its cryostat (a bell carrying eddy currents) and of the gradient coil assembly, and quite apart from the ear-splitting noise this can make, *oscillatory* currents can be induced that once again change the main magnetic field. The depressing conclusion is that following a change of gradient, the main magnetic field B_0 can vary as

$$\delta B_0 = \sum_{n=0}^{\infty}\sum_{m=0}^{n}\sum_{p=0} F_{nmp}\left(\exp\left[i\omega_{nmp} - \frac{1}{\tau_{nmp}}\right]t\right)U_{nm} + G_{nmp}\left(\exp\left[i\omega_{nmp} - \frac{1}{\tau_{nmp}}\right]t\right)V_{nm} \qquad (2.5)$$

where F_{nmp} and G_{nmp} are the amplitudes, the frequencies ω_{nmp} include zero, and the time constants τ_{nmp} can range from microseconds to seconds. Note that in general, the frequencies and time constants are not necessarily the same for different orders n and degrees m and that a main field offset U_{00} is included in the equation. Mathematically, this type of equation is formally known as a *complex mess*.

What tools can be brought to bear to reduce the F and G in equation (2.5) to acceptable sizes? Probably the most important tool is gradient shielding. Imagine a gradient coil inside an infinitely long superconducting cylinder. When the gradient is switched on, persistent eddy currents flow in the cylinder in a manner that prevents magnetic fields escaping. There is then no mutual inductance to exterior circuits. Of course, the superconducting eddy currents distort the interior gradient field, but we can redesign the coil to correct for this defect. We then have a gradient coil free of coupling to the outside world. Implementation of an actual superconducting cylinder presents major difficulties (what happens when the magnet is energized?), but we may mimic the persistent eddy currents by replacing them with current in wires of appropriate winding density as shown in Figure 2.3 (blue lines): where eddy currents are strong, the wires are close together; where eddy currents are weak, the wires are far apart. The scheme is imperfect as a continuous surface distribution of eddy currents cannot be exactly reproduced with discrete wires and further, the (nonconducting) cylindrical former upon which the wires are laid cannot be infinitely long. Nevertheless, the introduction of shielded gradients was an important advance and it reduced the coefficients in equation (2.5) substantially.

Other tools include gradient designs that have zero net torque, the use of a very thick copper magnet bore liner to shield the cryostat to very low frequencies (not quite a superconducting cylinder); the use of mechanical engineering techniques and building materials that reduce the ringing of acoustic resonances, the use of vacuum technology to contain acoustic noise and the shaping of gradient pulses to reduce high-frequency components, etc. Even with the application of all these tools, however, some of the coefficients in equation (2.5) may still be worrisome and we briefly examine them further below.

We must also consider the manifold interactions between the gradient coils used for imaging and localized spectroscopy, and shim coils. Fortunately, symmetry comes to our aid. Thus, the interactions between the gradient coils themselves are *nominally* zero, as are the interactions with higher degree ($m > 1$) shims. We may also eliminate the strong interactions with first-order shim coils by eliminating the shims! A small, variable direct current through the gradient coils then replaces them. There are potentially strong interactions between the z gradient and the z^3 shim ($n = 3$, $m = 0$) and between the z^2 shim and the magnet, but these should be removed by design. There then remain residual interactions and at this point, electronics can take over. The *generic* circuit diagram for both a shim and a gradient coil is the same, and it is shown in Figure 2.4a – only the component values differ. The coils, with currents I_{nm}, each have a self-inductance L_{nm}, a resistance r_{nm}, a parasitic capacitance C_{nm} that causes resonance at a high sonic

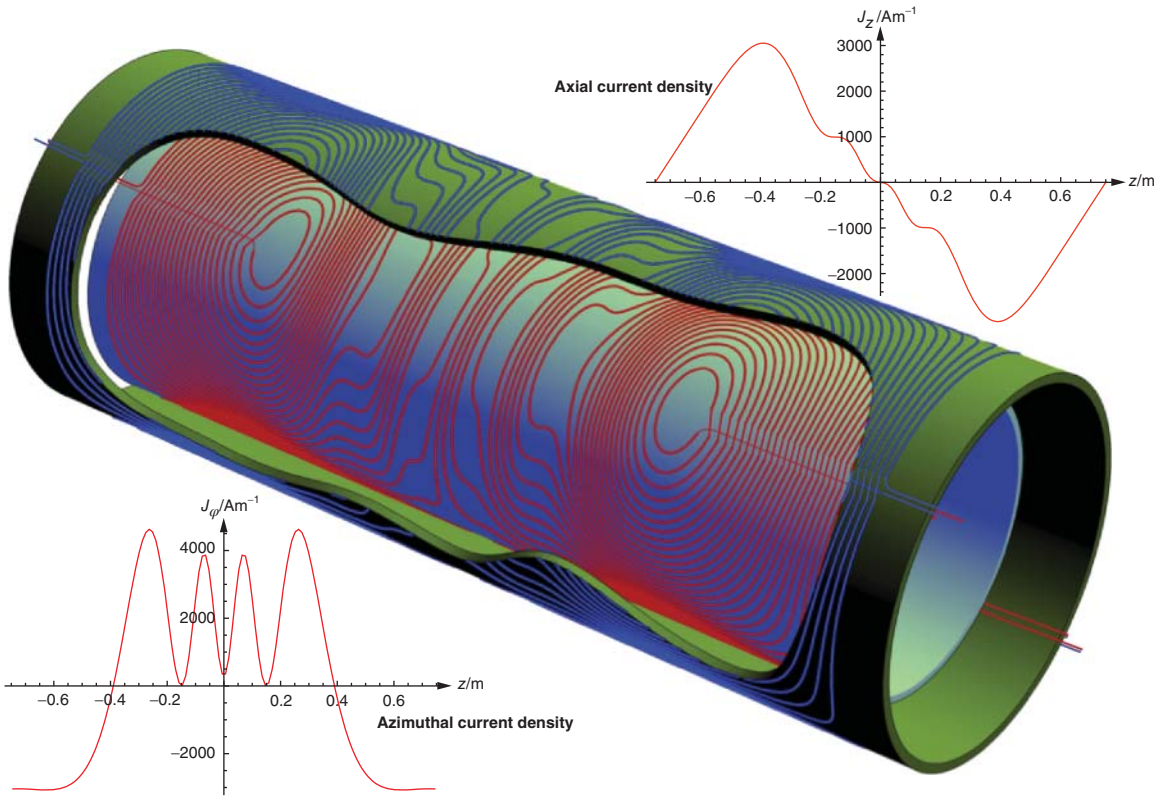

Figure 2.3. A shielded gradient coil assembly that uses distributed inner windings (red) to improve gradient purity and an outer, second set of windings (blue) to greatly reduce fields outside the assembly. Note that partial connection in parallel can reduce inductance. Similar distributed single-layer windings can also be used for shim coils

or ultrasonic frequency, a parasitic impedance Z_{pnm} associated with external residual couplings (e.g., to the magnet), and, during gradient switching, a series emf, $E_{nm} = L_{nm}\ \mathrm{d}I_{nm}/\mathrm{d}t$ associated with self-inductance or a series emf, $E_{gnm} = M_{gnm}\ \mathrm{d}I_g/\mathrm{d}t$ associated with mutual inductance M_{gnm}, where the index g references the gradient coil whose current is being switched. Clearly, emf's E can temporarily change the desired flow of current, the change depending on the source impedance Z_{snm}. Thus, it is important to make impedance Z_{snm} as large as possible, and the tool we use is negative feedback to create a current source with very high dynamic output impedance.

The concept of a constant current source is encapsulated in Figure 2.4b. Obviously, to work correctly, the source power supplies must have voltages $\pm V_s$ somewhat greater than the extrema of E, and to avoid instability or oscillation, the feedback factor $\beta(\omega)$, a function of frequency, must be as large as possible over as large a bandwidth as possible but reduce to <1 at the frequency at which its phase has changed by 180° (the Bode stability criterion) – in practice, 135° is used to give a margin of safety. With increasing voltage, amplifiers rapidly increase in expense and the risk of arcing in the gradient coils magnifies, so it is important to maximize the gradient coil efficiency so that *for a constant desired gradient strength*, the inductance L is minimized. The time Δt in which a gradient current can be changed by ΔI then varies as $\Delta I\ L/V_s$. For shims, on the other hand, which carry current constantly, it may be more important to minimize resistance and thereby heat deposition in the magnet bore. (Design techniques for both cases exist.) If shim power supply voltages, determined by the size of E_{gnm}, are excessive, it also may be necessary

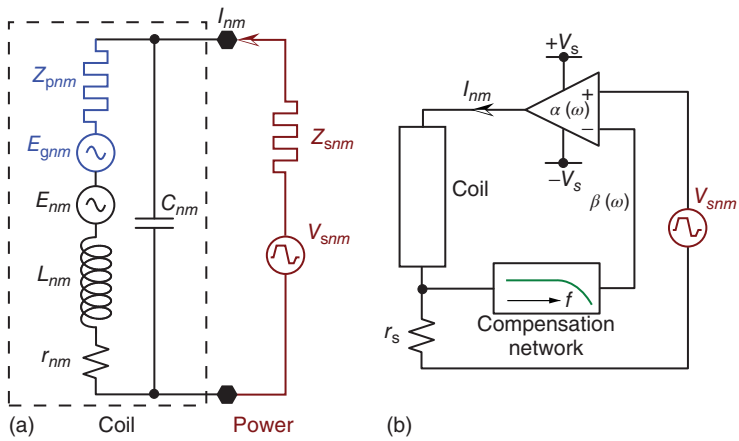

Figure 2.4. In (a), the circuit elements of a shim or gradient coil are shown with parasitic impedance and voltage due to exterior couplings (blue). The coil has a power supply with voltage V_{snm} and internal impedance Z_{snm} (red) but the current is not entirely independent of induced voltages E. To keep the coil current I_{nm} proportional to voltage V_{snm}, Z_{snm} must be very large, and so a constant current source is used, as shown in (b). For an amplifier with a very large gain α, the voltage V_{snm} at the positive input essentially equals that at the negative input. The latter is $I_{nm}r_s$, where r_s is a small sensing resistance, and therefore $I_{nm} \simeq V_{snm}/r_s$

to introduce compensatory mutual inductance to cancel M_{gnm}. Minimization of L_{nm} has the added benefit of increasing the gradient coil self-resonant frequency $\omega_{nm} = (L_{nm}C_{nm})^{-1/2}$, which in turn allows the constant current source to function satisfactorily at higher frequencies.

With an ensemble of multiple coils and amplifiers with multiple interactions, there is always the risk of ensemble oscillation. Mercifully, this rarely occurs and it can usually be cured by a reduction of bandwidth. A huge additional benefit of negative feedback is that it ensures great linearity in the relationship between coil current I_{nm} and the drive voltage V_{snm} from the pulse programmer, provided the sensing resistor r_s in Figure 2.4b does not change in value as it heats. However, a linear relationship between voltage and current does not necessarily imply a time-independent linear relationship between voltage and gradient strength, as is hopefully clear by now.

When all the above tools have been used, there remain the residual field fluctuations of equation (2.5) and their effects on spectral line shape can sometimes be observed, so the user should not entirely forget about them. If they are important, a last resort is to calibrate the time dependence of those orders and degrees for which there are shim coils (the gradient coils themselves are included in this statement). Given that the fluctuations are proportional in amplitude to the gradient change, there then exists the possibility of cancelling them by injection of compensating currents into shims/gradients for which a dedicated micro-controller may be needed. These residuals are more important in spectroscopic applications than in imaging and can be responsible for oddly shaped spectral lines. Finally, there is one important component of equation (2.5) for which there is often no shim coil: U_{00}, a spatially invariant field. The latter commonly has a low-frequency, transient oscillatory component associated with acoustic ringing. If a U_{00} coil (a 'field-offset coil') is present, then it may be considered a shim coil and the above analysis pertains. If, however, it is absent (and magnet bore space is expensive), there remains the possibility of compensatory modulation of the receiver detection frequency instead; for example, by control of the signal-sampling rate. Typically, a user will only discover this piece of sophistry if an auxiliary receiver is attached to the MR instrument for some reason, in which case it can cause much head scratching!

In conclusion, it is obvious from equation (2.5) that residual transitory effects associated with gradient switching are generally smallest at the origin of the magnet/gradient/shim system. Thus, just as when considering homogeneity, the closer the region of

interest can be to the origin, the more likely it is that the best results will be obtained.

2.3 RADIO-FREQUENCY ENGINEERING

2.3.1 Core Components

We now consider a collection of RF electronic devices, grouped conceptually about the NMR sample, that form a natural ensemble (Figure 2.1) with five principal tasks to perform: (i) The generation in a power amplifier of high-power (typically kW) precise RF pulses at about the Larmor frequency; (ii) The excitation of the NMR sample with that power by the creation, with a transmitting coil, of RF currents that generate a rotating magnetic field B_1; (iii) The detection of precessional magnetization in a receiving coil, predominantly by Faraday induction of a small RF voltage ξ (nV to mV); (iv) Amplification in a pre-amplifier of that voltage, with the addition of as little extra noise as possible (low 'noise figure'), so that it can be safely passed without the loss of signal-to-noise ratio to the receiver and computer; (v) Screening from external interference with a Faraday cage that also prevents the transmission of interference at the Larmor frequency to the outside world.

There are several possible permutations and combinations of the above devices: the Faraday cage or screen may be buried in the walls and doors of the magnet room or may be an integral part of the magnet; the transmitter and receiving coils may be one and the same or they may be separate; there may be multiple receiving coils in simultaneous use, each with its own pre-amplifier; there may even be multiple transmitter coils, each with its own power amplifier; excitation of more than one nuclear species at a time (e.g., ^{31}P and ^{1}H) may be possible, etc. The chosen arrangement depends entirely on the experiment and its demands (see Chapter 3). However, in all instances, there are fundamental design constraints that must be considered: the power amplifier must have good linearity so that the phase and amplitude variations of the B_1 transmitting field are as expected; the transmitting coil must be able to handle the applied power without arcing or burning out; RF power must not be wasted as it is expensive; if something goes wrong, it must be detected and the power amplifier quickly shut down; the transmitter power must not destroy the pre-amplifier; during signal reception, the power amplifier must be well and truly turned off so that it does not degrade the signal with extra noise; if multiple coils are used, they should not interact and degrade one another's performance; the first transistor in a pre-amplifier should be noise-matched to its receiving coil so that it adds minimal extra noise to the signal, etc. This is a large and difficult list and in the space available, we may only examine it briefly. Not surprisingly, any aspect of the above list may impinge on the others.

2.3.1.1 Power Amplifiers

The manufacture of RF power amplifiers is a highly specialized trade. In the past, it was common for huge vacuum tubes (valves) to be employed that could generate the necessary kilowatts, and there is still a place for them as they are amazingly robust and can handle considerable abuse when reflected RF power is deposited in them rather than in the load (the transmitter coil). However, they suffer from a serious drawback – they do not function in a magnetic field greater than roughly 50 mT and must therefore be kept well away from the magnet. This creates the problem of how to transport the RF power from the remote transmitter to the interior of the magnet without radiation of radio waves, and to do this a coaxial cable is used; the characteristic impedance is typically 50 Ω. Thus, power amplifiers are normally designed to deliver their maximum power into a load of 50 Ω. Note that this does *not* imply that the output impedance of the device is 50 Ω, quite the contrary. (See below for a discussion of how to employ this fact gainfully.) While such power matching is efficient, a design that implements it is often constrained by maximum safe working voltages. Thus, matching is sacrificed for greater available output power. It should be noted that efficiency is also sacrificed when long coaxial cables are needed, as they have resistance.

Power transistors (typically metal oxide field effect transistors or MOSFETs), by contrast, *can* function in strong fields, but typically only deliver hundreds of watts. In recent years, there has been a move to place multiple MOSFET amplifiers near the magnet and combine their outputs to obtain the desired power, either in Wilkinson or quadrature hybrid couplers. This has required innovative power line design, as a standard procedure to prevent RF power escaping from an amplifier is to use ferrite-based power line filters. Ferrites, of course, saturate in a magnetic field and cease to have a large differential permeability. Even more than tubes, MOSFET power amplifiers sacrifice power matching for greater maximum power output, and they

are also more likely to breakdown or burn out when confronted with loads that are not 50 Ω. There *are* design methods that help protect amplifiers against this possibility: for example, ferrite lumped-element circulators can divert reflected power to a 50 Ω load. In this instance, the ferrite needs a saturating magnetic field, which can conveniently be provided by the MR magnet.

There is a trade-off in amplifier design between power efficiency and linearity, and a common compromise is so-called 'class-AB' push–pull amplification. A class-AB amplifier normally has two power transistors, one for the positive portion of a cycle of RF signal and the other for the negative portion. The transition, or crossover, from one transistor to the other is arranged to be smooth so as to reduce crossover distortion, but the latter cannot be removed entirely, and so the amplifier generates harmonics of the Larmor frequency. A more serious generator of harmonics, however, is the two transistors' 'running out of steam' at high power as they approach saturation. This flattens the top and bottom of a cycle and introduces odd-order harmonics as well as reducing the output at the fundamental frequency. The consequence is that the graph of output voltage versus input voltage falls away from a straight line at higher values, and this nonlinearity can compromise the efficacy of shaped or selective pulses. More subtly, the phase of the RF output may also change with increasing power. While RF negative feedback techniques (e.g., Cartesian feedback[2]) exist to correct these defects, they are difficult to use and so a simpler approach is the use of predistortion: once the amplifier's characteristics are known, the microprocessor that shapes the amplifier's input waveform can compensate for nonlinearity. The main drawback to this approach is that the amplifier's characteristics change during warm-up and may also drift over a period of months. Recalibration is usually possible if poor pulse performance is suspected.

At the highest magnetic fields (7–11 T), the use of multiple transmission coils is a topic under active research at the time of writing as, in principle, sample power deposition for ^{1}H can be reduced and a more homogeneous B_1 field obtained. However, the coils tend to have considerable mutual impedance, and so driving one coil causes appreciable current to flow in its nearest neighbors, thereby corrupting the desired B_1 field. The fact that the output impedances of RF power amplifiers are not 50 Ω can help decouple coils to a limited extent (∼ −11 to −16 dB), as discussed in detail below for the corresponding case of receiver coil interaction, and Cartesian feedback can create constant current sources (c.f. gradient coil power supplies) resulting in excellent isolation (∼40 dB). However, as mentioned earlier, the latter technique is both expensive and difficult, so current approaches tend to focus on calibrating the interactions and then orthogonalizing the interaction matrix (c.f. the discussion on translated shims above).

2.3.1.2 Taming RF Power

The issues of protecting the pre-amplifier from transmitter power and noise are intimately connected in that both rely on the same philosophy – the use of PIN diodes, controlled by the passage of direct current, that act as RF switches. For primary protection purposes, these devices have almost entirely replaced ordinary high-speed diodes connected in anti-parallel ('crossed diodes'), as they do not have a threshold for operation and generate less distortion. PIN diodes (*p*ositively doped, *i*ntrinsic and *n*egatively doped semiconductors) are capable of storing charge Q_I in their intrinsic layer when a direct current I_{DC} flows. The charge can then be extracted over a short time by a reverse voltage and replenished by a forward voltage; in other words, the diode can conduct RF current. As charge Q_I is the integral of current, it follows that the higher the frequency (and hence the shorter the period), the more RF current can be drawn. If the current limit is exceeded, the diode is starved of charge, its RF resistance increases and it may burn out. Conversely, PIN diodes have a minimum recommended frequency; at much lower frequencies, they behave as ordinary diodes. As with all electronic components, the correct diode has to be chosen for the job at hand. The effective 'on' resistance is typically $\sim 0.01/I_{DC}$ Ω plus a parasitic inductance (∼1–2 nH), where I_{DC} is in the range 10–100 mA; the 'off' impedance is usually dominated by the diode's parallel capacitance of typically ∼1 pF. In advanced designs, both inductance and capacitance may be tuned out.

PIN diodes are normally operated in the 'on' mode in the presence of RF power because when off, a reverse voltage V_R large enough to prevent significant RF conduction must be applied. Voltage V_R may need to be as a large as the RF signal amplitude, depending on frequency, and switching large direct voltages rapidly is then cumbersome and costly. Figure 2.5 shows the genesis of series and parallel switches that isolate the RF power from the direct current source and *vice versa*. These switches do *not* use the ferrites typically found

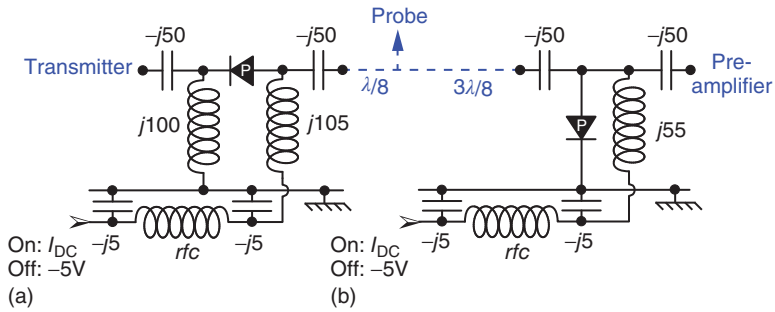

Figure 2.5. Elementary building blocks for PIN diode switches. When on (direct current I_{DC} flowing), circuit (a) is designed to pass high power while preserving 50 Ω continuity; circuit (b) is designed to short-circuit power to protect a device to its right, but to preserve 50 Ω continuity when off. Conversion of reactance to high (or low) impedance can be accomplished with appropriate filters or lines of the correct length, as shown in blue. With such additions, a variety of switches for the various MR permutations can be constructed

in manufacturers' literature for PIN diode switches,[3] and so are suitable for use in the fringe field of the magnet. They rely on T-section filters; when allowing RF current at the Larmor frequency to pass, they can be shown to maintain 50 Ω continuity and so are compatible with coaxial cable. As an example of use, albeit not recommended due to excessive line length, the circuits could be joined and a probe's cable also connected to the joint, as shown in the figure. The reader can doubtless think of many other configurations and modifications. With higher powers and frequencies, switches may need to be concatenated to achieve the desired protection or noise rejection, but the relevant specifications for any switch are insertion loss and isolation, both usually measured in decibel. To achieve excellent results, all lines, capacitors, and inductors must have the least loss possible and, in general, the fewer components the better. Note that the filters in the direct current supply lines may ring at a low frequency if the current/voltage source does not provide damping. Finally, a potential problem with the abandonment of ferrites with their broadband capability is that switches may not protect the pre-amplifier against harmonics created by the power amplifier. This possibility should always be borne in mind if pre-amplifiers burn out for no apparent reason. It should, however, have been guarded against with filtering in the power amplifier.

2.3.1.3 The Faraday Cage

A Faraday cage is a conductive closed box, usually made of copper foil or sheet, that encases at a minimum the probe and sample, and maximally, the magnet, patient table, power amplifier, and pre-amplifier, as shown in Figure 2.1. The underlying principle is that radio waves, electric fields, and high-frequency magnetic fields cannot pass through the copper. Any magnetic resonance system operates at radio frequencies; in other words, at frequencies that could be used if we so desired to transmit and receive radio waves. However, we emphatically do not want to do so, hence the cage. The problem with this concept is that we wish to pass cables and maybe light, perfusion lines, and other exotica through the cage, thereby potentially destroying its efficacy. When a cage ceases to function properly, as manifest by unexplained spectral phenomena such as localized noise, unexpected and variable spectral lines, etc., or complaints of interference from neighbors, it is almost certain that the integrity of the screen has been breached by the passage of something in an unapproved manner; for example, a cable. That cable then acts as an antenna outside the screen and carries power from the local FM radio transmitter inside, and *vice versa*. If such leakage is suspected, it can sometimes be detected with a portable radio inside the cage. (Beware magnetic batteries!) Absolutely no signal should be detectable at any wavelength or frequency.

To pass RF coaxial cables through the screen is usually quite simple. It is the cable's outer shield that acts as an antenna and picks up radio waves and so it is the *shield* that must not pass through a hole in the cage. Rather, the cage is rigorously connected to the shield, usually with the aid of a metal panel on which is mounted a 'bulkhead connector' – a double connector for cables that is designed for just this purpose. Once exposed, for example, at the probe, the cable's center conductor can potentially radiate interference but it is

supposed to originate in a device, such as the power amplifier, that is itself shielded. It may be helpful to imagine the cage and every external device with a penetrating RF cable as having a conducting outer surface of complicated but *unbroken* topology.

Passing *unshielded* cables such as those for shims and gradients is a little more difficult. Each cable must pass through a lowpass filter that severely attenuates radio frequencies but does not affect switching times. The filter comprises π-sections whose arms are inductors and whose legs are capacitors directly connected to the screen. Each filter is usually in its own shielding box. Rarely, a defective filter may be the cause of a failure of shield integrity. For passing nonconducting lines such as fiber-optic cable through a screen, a waveguide is used. This is a copper tube, of length about 10 times its diameter D, that passes through the screen and is soldered in place with no gaps round the circumference. Radio waves of wavelength greater than $1.7D$ are rapidly attenuated and effectively cannot pass.[4] A classic error is to pass a conductor or cable through a waveguide. In this context, remember that tubes carrying saline are conductors. To pass light into a room for projection of images, a waveguide can be used, or if this is too restrictive, a window that is essentially an aquarium filled with saturated salt solution. The challenge is to connect the conducting solution to the screen without leakage and corrosion. Yet another technique is to use glass over which a fine copper mesh has been placed. The wires are, of course, connected to the screen. However, this method, which is also used for patient viewing in MRI suites, can reduce screening efficacy a little.

2.3.1.4 The Pre-amplifier

During signal reception, the receiving coil has an induced NMR signal voltage ξ, together with an induced random noise voltage caused by the Brownian motion of the sample's electrolytes. The random motion of the coil's electrons also generates a little noise, and neglecting temperature differences, a measure of the total noise N is the effective coil resistance r_c. Noise N is usually $\sim 0.1\,\text{nV}/\sqrt{\text{Hz}}$, so in a bandwidth of 1 MHz, it is $\sim 0.1\,\mu\text{V}$, a rather small voltage. Now signal and noise are ultimately passed through a receiver to an analogue-to-digital (A/D) converter so that they may be processed in a computer, and we do not want the signal to be degraded in any way before the conversion. Degradation takes two principal forms: the addition of extra noise and distortion or signal clipping that may give anomalous results such as small spurious spectral lines and dips beneath large lines. The pre-amplifier is the first piece of active electronics encountered by ξ and N, and its job is to amplify them by a factor α so that αN is much greater than any subsequent additional receiver noise N_{rec}. If α is too big, however, a particularly large signal may overload the receiver, causing distortion. Thus, a compromise usually sets α in the range 20–30 (26–30 dB).

In the process of signal reception, the pre-amplifier itself must add minimal extra noise, and it is worth examining how this is accomplished. A simple noise-equivalent circuit for a transistor is shown in Figure 2.6. It comprises voltage and current noise sources, N_a and I_a, respectively, which, to a good approximation, are uncorrelated with one another and with the noise N from the receiving coil. The transistor also has an input impedance Z_a that is considered noiseless – any noise is subsumed in the noise sources. Now assume that our received signal and noise are somehow transformed in size losslessly such that their source resistance r_c, the receiving coil resistance, becomes a new resistance R_c, as shown. (How this is performed lies in the domain of receiving coil or probe design – see Chapter 3; suffice it to say that the aid of low-loss capacitors is vital.) The signal and noise, by conservation of energy, are increased by a factor of $\sqrt{R_c/r_c}$ to ξ' and N'. Remembering that uncorrelated random functions add quadratically, the total noise N_{tot} at the input to the transistor is given by

$$N_{\text{tot}}^2 = \beta^2\left(N^2\frac{R_c}{r_c} + N_a^2 + I_a^2R_c^2\right); \quad \beta = \frac{Z_a}{Z_a + R_c} \tag{2.6}$$

whereas the signal at this point is

$$\xi' = \beta\xi\sqrt{\frac{R_c}{r_c}} \tag{2.7}$$

Let us now maximize the signal-to-noise ratio $\Psi = \xi'/N_{\text{tot}}$ by varying the transformation. Setting the differential of Ψ with respect to R_c equal to zero, we obtain for the optimal value of R_c

$$R_{\text{opt}} = \frac{N_a}{I_a} \tag{2.8}$$

This is an important equation. It states that a primary condition for obtaining the best noise performance from a transistor is that the signal source must have its source resistance r_c transformed to a resistance R_{opt}. Equally importantly, note that R_{opt} has nothing to do with the input impedance Z_a – they are generally

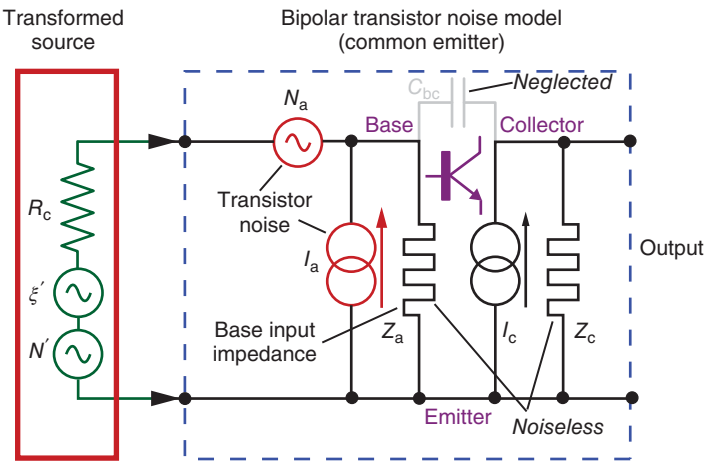

Figure 2.6. A simple transistor-noise model with noise matching. By appropriately transforming the source resistance, signal, and noise to new values, the noise added by the transistor may be minimized

completely different in value. R_{opt} is under the control of the transistor manufacturer, whose datasheet must state either R_{opt} or E_a and I_a *at the frequency of interest* for it to be useful. Representative values of R_{opt} in the region of 100 MHz are 1000 Ω for a field effect transistor and 100 Ω for a bipolar transistor, but the datasheet or some other reliable source should always be consulted in this regard. Input impedances Z_a are typically much greater.

2.3.1.5 Noise Figure

When we look at how much extra noise the pre-amplifier has added, a measure is the ratio

$$F' = \frac{N_{tot}}{N'} = \left(\frac{N'^2 + 2N_a^2}{N'^2}\right)^{1/2} \tag{2.9}$$

where we have used equation (2.6) and substituted for I_a from equation (2.8). The quantity F' is known as the *noise factor* of the transistor (the square is also used), but it is more common for the noise figure in decibels, $F = 20 \log_{10} F'$, to be quoted. An excellent noise figure is 0.3 dB, which translates to $F' = 1.035$. While a transistor manufacturer may quote such a figure, in practice, it is extremely difficult to maintain when switches and other circuits involving lines, inductors, and capacitors are part of the transistor's signal source. In particular, inductors with quality factors $Q = \omega L/R$ greater than 200 are difficult to construct and the introduction of their resistance R generates extra noise N_R, as given by Nyquist's famous formula

$$N_R = \sqrt{4kTR\Delta f} \tag{2.10}$$

Here, k is Boltzmann's constant, T the resistance's absolute temperature, and Δf the bandwidth in hertz of the measuring equipment. The noise figure is usually defined for a standard source temperature of 290 K. Equation (2.10) also applies, of course, to r_c and R_c.

In a system that uses 50 Ω cable, it is inconvenient to have a pre-amplifier that gives its best noise performance from some other impedance R_{opt}. It is therefore common practice to hide inside a commercial pre-amplifier a filter, comprising a high Q-factor inductor and capacitors, that *at the Larmor* frequency transforms 50 Ω to R_{opt} with as little loss as possible. Crossed diodes to 'ground' may be included as part of one of the capacitances so as to give the transistor a modicum of protection from destructive voltages (Figure 2.7). Alternatively, a transistor (or several transistors in parallel) having $R_{opt} = 50\,\Omega$ may be chosen. The pre-amplifier is then a broadband device. In both cases, however, just because there is an appellation '50 Ω pre-amplifier', it does not mean that the device's input impedance is 50 Ω. In general, it is not; rather it is Z_a reverse-transformed by any filter.

It is particularly easy to measure the noise figure of a '50 Ω pre-amplifier' if it is attached to an MR console that can measure root-mean-square (RMS) noise. (To be accurate, it is the noise figure of the entire system that is measured, which is arguably even more

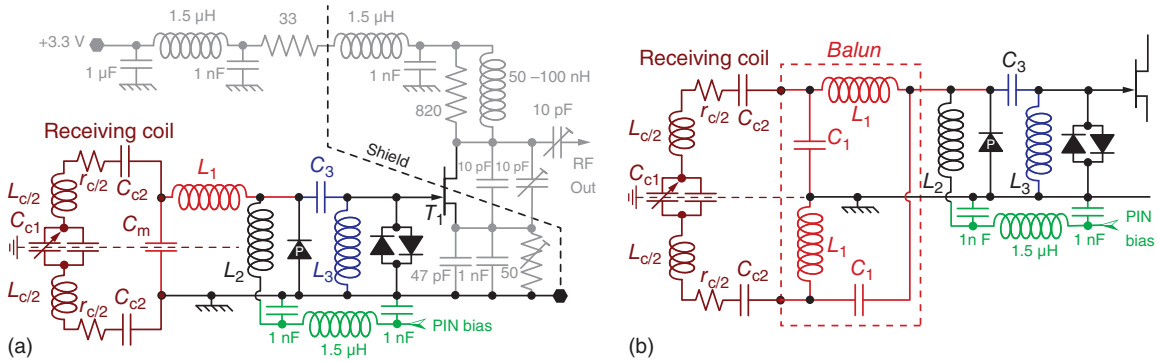

Figure 2.7. (a) A generic schematic of a low-noise FET pre-amplifier suitable for 100–400 MHz is shown. (b) Replacing coil-matching capacitor C_m with a balun creates an amplifier with a differential input. Component values depend on the frequency and the receiving coil's characteristics. Suitable gallium arsenide (GaAs) transistors are available from a variety of manufacturers but are only usually characterized for the low-GHz-frequency range

useful.) All that is needed is liquid nitrogen, a short cable terminated in a *well-shielded* 50 Ω RF resistor at room temperature T and another terminated similarly in 50 Ω but at 77 K. (In general, the two resistors will not have the same values at the same temperature. A network analyzer may be used to check the values.) Let the noise measured on the console with the room-temperature resistor be N_T while that measured with the liquid-nitrogen resistor is N_{77}. Then if α is now the overall gain from the pre-amplifier to the measured noise, from equations (2.6) and (2.10)

$$N_T^2 = \alpha^2\beta^2\left(N_S^2\frac{T}{290} + 2N_a^2\right);$$
$$N_{77}^2 = \alpha^2\beta^2\left(N_S^2\frac{77}{290} + 2N_a^2\right) \qquad (2.11)$$

where N_S is the noise from a standard-temperature resistor.

From the definition of noise factor in equation (2.9),

$$F'^2 = 1 + \frac{2N_a^2}{N_S^2} \qquad (2.12)$$

and solving equations (2.11) and (2.12) for the noise figure F at 290 K, we obtain

$$F = 10\ \log_{10}\left(\frac{213 - [290 - T]\,N_{77}^2/N_T^2}{290[1 - N_{77}^2/N_T^2]}\right) \qquad (2.13)$$

For example, if the measured noise at 23 °C was 1.22 units and that at 77 K was 0.712 units, the noise figure of the system would be 0.51 dB.

2.3.1.6 Pre-amplifier Input Impedance Effects

It has been emphasized earlier that the pre-amplifier input impedance Z_a is generally very different from the optimum source resistance R_{opt} and also that the effective resistance r_c of a receiving coil has to be transformed with as little loss as possible to resistance R_{opt}. High-Q capacitors, inductors, PIN diode switches, and low-loss coaxial lines may all be involved, in sum or in part as needed, to effect this forward transformation, the exact details depending on the experiment. However, the corollary is that Z_a suffers a reverse transformation, producing in the process a new impedance Z_b *in series* with the receiving coil. By introducing an excess number of variables in the forward transformation (usually at the expense of a little sensitivity), Z_b can be manipulated within broad limits while maintaining the transformation $r_c \to R_{opt}$. Uses of these excess degrees of freedom include speeding the ring-down of a low-frequency probe after a pulse and blocking the flow of current in the probe during signal reception while maintaining sensitivity. Such blocking, obtained by maximizing Z_b so that $Z_b \gg r_c$, is useful for: suppressing radiation damping, an effect discovered over 40 years ago by scientists at the Perkin-Elmer Corporation but never published; minimizing change of signal strength when a conducting sample changes size (e.g., a perfused heart);[5] and reducing induced voltages when there is more than one coil and there is mutual induction M_{pq} between them,[6] a situation that is increasingly common as B_0 field strengths increase. Such intercoil coupling can correlate signals and noise and reduce the efficacy of an array of coils.

(Comparison with the use of constant current supplies for shim and gradient coils is apt.) The voltage V_q induced in coil q by signal voltage ξ_p in coil p is then approximately $j\omega M_{pq}\xi_p / (Z_b + r_c)$ rather than the much larger $j\omega M_{pq}\xi_p / r_c$. (It is assumed here, as is usually the case, that the receiving coil's inductance is approximately cancelled by capacitance.) The ratio of these two voltages, or synonymously that of the currents in coil p, depends mainly on the ratio of R_{opt} to the real part of Z_a as mediated by the transformation circuitry, and is typically in the range −17 to −25 dB: −40 dB would be ideal.

When multiple receiving coils are used, the intermediary of 50 Ω cable is usually dispensed with and a pre-amplifier placed directly on each coil. Consider the circuit of Figure 2.7a, which combines low-noise pre-amplification, PIN diode protection from large induced voltages during transmission, and both PIN diode and transistor current blocking. Ignoring inductor losses for the moment, the primary characteristic of the circuit is that inductor L_1 (red) has the same reactance X_1 as the coil matching capacitance C_m. Thus, when the PIN diode is turned on and has very low impedance, L_1 and C_m parallel-resonate, thereby creating a high blocking impedance in series with the receiver coil. When the diode is off, it follows that a high blocking impedance Z_b can be maintained if capacitor C_3 and inductor L_3 (blue) also resonate, albeit in series (the transistor's input impedance is assumed to be very large). In both cases, the value of (large) biasing inductor L_2 has little effect as it feeds a low impedance. It can then be shown that the condition

$$L_1 \cong L_3\sqrt{\frac{r_c}{R_{opt}}} \tag{2.14}$$

must be obeyed for good noise performance.

To find the value of L_3, and indeed to optimize the circuit, we must consider resistive loss and the Q-factors of the inductors. The author favors toroids wound on small Teflon formers as Q-factors well over 100 can be obtained and they have negligible coupling. Once an average Q-factor is known, the circuit values are optimized by numerical minimization of a metric that includes insertion loss and the reciprocals of the two blocking factors. In general, insertion loss and current blocking trade against each other, but with care, it is possible to obtain an insertion loss of <−0.1 dB and blockings approaching −30 dB. It is usually found that equation (2.14) is obeyed but that L_3 and C_3 may not exactly resonate. In passing, note the use of (nonmagnetic) crossed diodes for extra transistor protection – all other components must be nonmagnetic too. Other design techniques include the use of self-rectification to power the PIN diode from the induced coil voltage during transmission, and the provision of power and/or PIN diode bias down the same cable used to send the signal to the receiver.

Finally, we note an esoteric and poorly understood fact about current blocking that becomes increasingly important at higher Larmor frequencies. When the length of conductor in a receiving coil begins to approach a wavelength, stray or parasitic capacitances to the surroundings (including other coils) can no longer be ignored and so symmetric operation, both physically and electrically, is employed in an attempt to minimize their effects. Now current blocking often effectively replaces a matching capacitance such as C_m in Figure 2.7a with large impedance Z_b that is resistive when maximized. Then, symmetry is only maintained if the mid-point of Z_b is on the coil axis of symmetry (the brown dashed line) *and that axis coincides with zero potential* ('ground') for the pre-amplifier. This is clearly not the case in the figure, but Figure 2.7b shows a circuit that fulfils this goal. The balun, in which C_1 and L_1 resonate, effectively replaces the matching capacitor C_m of Figure 2.7a. Once again, when the PIN diode is on, or if L_3 and C_3 are resonant, a high blocking impedance is placed in series with the receiving coil. The value of L_1 is again given by equation (2.14) and numerical optimization should still be employed to obtain insertion loss and blocking comparable with that of Figure 2.7a. Further discussion of the fascinating topic of balance is beyond the scope of the chapter.

2.3.2 The Receiver

2.3.2.1 Dynamic Range and Filtering

The signal and noise from the pre-amplifier pass out of the Faraday cage and into the receiver, whose job it is to prepare them for digitization and thence passage to the computer. The largest signals encountered in spectroscopy are from ^{1}H, and high-resolution proton spectroscopists are well accustomed to having to saturate the water solvent signal, as it can overload the receiver. However, biological ^{1}H signals are often from fat as well as water (see Chapter 1), and while in the *frequency* domain, the fat spectrum is much smaller than that of water, thanks to greater linewidths, in the *time* domain, the initial height of

the rapidly decaying fat FID may also overload the receiver, albeit only for a short time. It follows that the receiver must be designed to handle large signals (say ~0.2 V), unless it can be guaranteed that ^{1}H experiments will never be performed. Of course, the *smallest* observable frequency-domain signal may be buried in the noise in the time domain. The RMS noise from the pre-amplifier is typically $\sim 20\sqrt{\Delta f}$ nV, where the bandwidth Δf may be many megahertz.

The ratio in the time-domain of the largest signal to the noise is the signal dynamic range S_{DR}, and to a limited extent, this is under engineering control because it involves the noise with its square root dependence on bandwidth. However, the A/D converter plays a key role in this regard. If buried signals are not to be lost, the converter must sample the noise adequately and it may be shown that its resolution (1 bit) should be smaller than approximately twice the RMS noise voltage. In contrast, the *maximum* signal the A/D converter can handle is determined by its total number of bits B. Remembering that it must sample both positive and negative voltages, the A/D converter's dynamic range A_{DR} is then $\sim 2^B$. At audio frequencies, it is possible to obtain A/D converter's with very high resolution: B can be 18 or even 24 bits. However, with increasing frequency, the resolution diminishes, until, in the region of 300 MHz, the *effective* number of bits may only be 8 or 9 unless a fortune is paid. Note the use of the adjective *effective*: an A/D converter may be advertised as having B bits resolution, but with increasing sampling frequency, the resolution diminishes. To combat this problem, undersampling is sometimes used; in other words, a signal at the Larmor frequency f is sampled at a much lower frequency f_S. Provided the sampling aperture is much less than the Larmor period, this strategy combats the loss of bits quite well, but may actually be counterproductive in improving dynamic range. The reason is that the bandwidth of the noise must be less than $f_S/2$ (the Nyquist sampling theorem) if noise is not to be aliased and sensitivity sacrificed. However, loss of bandwidth diminishes noise and thereby increases dynamic range, so more bits are needed!

Clearly, the trade-off between undersampling and dynamic range depends on the technology of analogue-to-digital conversion, which, as with all digital electronics, advances rapidly. However, at the time of writing, to be able to handle the MR experiment's dynamic range, it is common for frequency changing to be employed, wherein the frequency of the MR signal is reduced in a mixer. An example of how this can be done is shown in Figure 2.8a for a Larmor frequency of $f_0 = 300$ MHz. There, in a mixer and letting $\omega = 2\pi f$, the signal $A\cos(\omega_0 t)e^{-t/T_2}$ from the pre-amplifier is multiplied with a 279 MHz signal $\cos(\omega_1 t)$ from a frequency synthesizer. By simple trigonometry, sum and difference frequencies are generated and the signal $A/2\cos([\omega_0 - \omega_1]t)e^{-t/T_2}$ at 21 MHz is extracted with a 21 MHz filter. The latter restricts the bandwidth of the noise to 2 MHz and so gives a possible signal dynamic range of ~70 dB. The signal is then undersampled with an A/D converter at a rate of 4 MS/s (million samples per second, $f_s = 4$ MHz); several suitable and inexpensive 14-bit devices exist. As shown in Figure 2.8b, the resulting

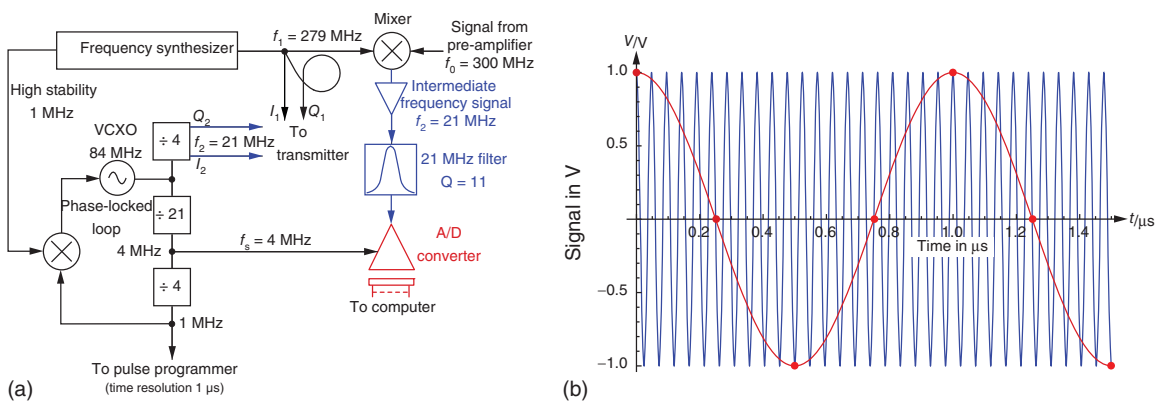

Figure 2.8. An example of frequency changing and undersampling for improvement of digital dynamic range. In (a) an intermediate frequency of 21 MHz is used but the signal is sampled at 4 MHz. The sampling (red points) is shown in (b) and the sampled signal clearly has a frequency of 1 MHz. After Fourier transformation, the MR spectrum is in the middle of the 2 MHz frequency range

digitized signal clearly has a frequency of 1 MHz and in a simple approach, following Fourier transformation, the MR spectrum can be extracted from the small region it occupies in the midst of the 2 MHz spectral range. Other approaches include before Fourier transformation, digital reduction of the sampling frequency with signal processing hardware that maintains S/N ratio, a process known as *decimation*. Note that the figure also shows generation of a 1 MHz signal for the pulse programmer. This ensures that in a repetition of an experiment, the digitized MR signal always has the same phase.

2.3.3 Pulse Generation

Figure 2.8a also shows four signals that aid in the creation of the transmitter pulse, all of which are locked to a highly stable, master 1 MHz oscillator in a frequency synthesizer. Let the 279 MHz signals be $I_1 = \cos(\omega_1 t)$ and $Q_1 = \sin(\omega_1 t)$ and the 21 MHz signals have components $I_2 = \cos(\omega_2 t)$ and $Q_2 = \sin(\omega_2 t)$. While the generation of various pulse *shapes* and *phases* at given times lies in the domains of the computer, a micro-controller and digital-to-analogue converters (DACs), those pulses have to modulate the transmitter signal at the Larmor frequency and the four signals aid in that process. Let a complex pulse be expressed in the form $P(t) = R(t) + iS(t)$ where R and S are the outputs of two DACs. We combine these signals in so-called 'single-sideband mixers' such that the output is

$$\begin{aligned} V(t) &= R[\cos(\omega_2 t)\cos(\omega_1 t) - \sin(\omega_2 t)\sin(\omega_1 t)] \\ &\quad - S[\cos(\omega_2 t)\sin(\omega_1 t) + \sin(\omega_2 t)\cos(\omega_1 t)] \\ &= R\cos(\omega_2 + \omega_1)t - S\sin(\omega_2 + \omega_1)t \\ &\equiv \mathrm{Re}[P(t)\exp(i\omega_0 t)] \end{aligned} \tag{2.15}$$

The RF pulse $V(t)$ is then passed to the power amplifier. Part, or even all, of equation (2.15) may be constructed digitally.

2.4 CONCLUSION

Once the signal is safely in a computer, the burden of data handling shifts to the computer engineer and mathematician; the analysis of signal, the presentation of results, the storage of data, and the generation of pulses are all interesting topics but outside the scope of this brief survey. There are numerous esoteric design issues that have not been covered, particularly concerning the generation of the low-level transmitter signal and its phase relationships to the received signal sampling frequency and any mixing frequency. Those relationships must be highly stable with very small random variation (low phase noise) so that there is reproducibility between successive free induction decays or echoes. Nevertheless, the issues briefly discussed in the past few pages hopefully serve as an introduction to a fascinating, diverse, and complex discipline that continues to evolve and that is worthy of far deeper study by spectroscopists if they wish to use their expensive equipment optimally. The following reading list may help.

RELATED ARTICLES IN EMAGRES

Resistive and Permanent Magnets for Whole Body MRI

Cryogenic Magnets for Whole-Body Magnetic Resonance Systems

Weaver, Harry E.: Historical Comments on the Early Years of Superconducting NMR

Shimming of Superconducting Magnets

Shimming for High-Resolution NMR Spectroscopy

Hurd, Ralph E.: A Brief History of Gradients in NMR

Whole Body MRI: Local and Inserted Gradient Coils

Safety and Sensory Aspects of Main and Gradient Fields in MRI

Dadok, Josef: High-Field NMR Instrumentation

Multifrequency Coils for Whole Body Studies

Impedance Matching and Baluns

Receiver Design for MR

Radiofrequency Power Amplifiers for NMR and MRI

REFERENCES

1. D. I. Hoult, R. E. Richards, and P. Styles, *J. Magn. Reson.*, 1978, **39**, 351.

2. D. I. Hoult, D. Foreman, G. Kolansky, and D. Kripiakevich, *MAGMA*, 2008, **21**, 15.

3. Microsemi Corporation, The PIN Diode Circuit Designer's Handbook, Microsemi Corporation: Watertown, MA, 1998.

4. D. M. Pozar, Microwave Engineering, Wiley: Hoboken, NJ, 2005.

5. D. I. Hoult and R. Deslauriers, *Magn. Reson. Med.*, 1990, **16**, 41.

6. P. B. Roemer, W. A. Edelstein, C. E. Hayes, S. P. Sousa, and O. M. Mueller, *Magn. Reson. Med.*, 1990, **16**, 192.

FURTHER READING

C.-N. Chen and D. I. Hoult, Biomedical Magnetic Resonance Technology, Adam Hilger: Bristol, 1989. This book is out of date but still useful.

D. L. Eggleston, Basic Electronics for Scientists and Engineers, Cambridge University Press: Cambridge, 2011. An introductory book at the undergraduate level.

P. Horowitz and W. Hill, The Art of Electronics, 2nd edn, Cambridge University Press: Cambridge, 1989.

P. Horowitz and W. Hill, The Art of Electronics, 3rd edn, 2015. The definitive but rather overwhelming text. The third edition is eagerly awaited.

Chapter 3
Detection Coils for MRS

J. Thomas Vaughan[1], Russell Lagore[2], and Jinfeng Tian[2]

[1]*Columbia University, New York, NY, USA*
[2]*University of Minnesota, Minneapolis, MN, USA*

3.1 INTRODUCTION

Radio-frequency (RF) transmit and detection coils for magnetic resonance spectroscopy (MRS) are transducers that inductively couple RF energy to excite and then receive the NMR signal from a desired sample that is typically located adjacent to or within the volume of the coil(s).[1] Because both the excited and received RF signals are magnetic fields that share the same spatial direction and frequency, the transmit and receive coils can be one and the same, or alternatively, two separate coils that are decoupled from each other during transmission and reception. Both configurations are common in MRS. In any case, the coils are placed about a sample, or a sample is placed within the coil(s), both within the homogeneous center of a superconducting magnet whose main field, B_0, is directed along the cylindrical axis, as shown in Figure 3.1.

An electrical RF detection circuit, sometimes called a *tank circuit*, is connected to the RF coil, which stores the energy in an electromagnetic (EM) field, mostly within a wavelength (λ) of the coil confines. This energy oscillates at the RF between the electrical field in the capacitance of the circuit and the magnetic field in the inductance of the circuit and coil. It is the RF magnetic induction field of the coil that couples to the nuclear magnetic spins of the sample being measured. Because this occurs most efficiently at the Larmor frequency, $\boldsymbol{\nu_0}$, of the atomic nuclei under study, the inductive and capacitive reactance of the coil(s) are chosen to tune the frequency of the coil to match it. Ohmic and conductance losses in the circuit, the coil and the quasi-conducting sample and dielectrics result in noise and heat that degrade the signal-to-noise ratio (SNR) of the NMR signal, heating the circuit, and the sample.

Physically, in the vertical-bore magnet in Figure 3.1(a), the RF coil is mounted in a non-magnetic cylindrical probe and inserted into the bore of the magnet. In a horizontal-bore magnet (Figure 3.1b) the RF coil may be mounted around the inside periphery of the magnet bore (e.g., to form a 'body coil') or be attached to the patient bed on a moving table that introduces the sample and coil into the magnet as shown in Figure 3.1(b) or even attached to the patient directly. The coil, which is often a cylindrical cage-type circuit structure, may

Handbook of Magnetic Resonance Spectroscopy In Vivo: MRS Theory, Practice and Applications.
Edited by Paul A. Bottomley and John R. Griffiths
 ISBN: 978-1-118-99766-6
Also published in eMagRes (online edition)
DOI: 10.1002/9780470034590.emrstm1465

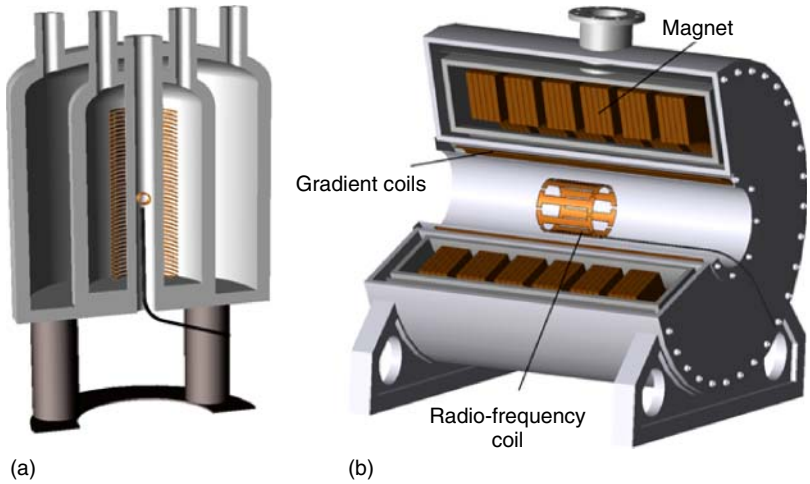

Figure 3.1. Cross sections of two typical superconducting MRS magnets. Vertical bore MRS magnets (a) are found in pharmaceutical and chemistry laboratories used for use with small animal models, excised tissue samples, and solutions. A small MRS detection coil is placed in its center. The coaxial cable connected to this coil, exits the magnet bore and interfaces with the MRS system's transceiver. Horizontal bore magnets (b) are used for preclinical and clinical MRS. While scaled to different sizes, the coils used in each system are of similar designs to those covered in this chapter

be surrounded on its outside, by a Faraday shield as shown in Figure 3.2. This shield can be part of the probe, or it can be integrated into the bore of the magnet, between the body coil and magnet bore, for example. The Faraday cage is designed through the use of appropriate materials, circuit pattern, and/or geometry to efficiently shield the RF coil from losses induced by the presence of the gradient, shim, and magnet coils within the magnet bore, while allowing the lower frequency gradient magnetic field pulses necessary for spatial localization, to permeate the central bore and enter the sample under study.

This chapter is dedicated to RF detection coils for MRS, although the same coils are often used for transmission as well, as noted throughout. While there can be as many RF coil designs as there are applications for them, 23 of the more common designs are presented. Background, description, circuit drawings, field plots, application notes, and references accompany each design. The intent is to provide the reader with enough information to select appropriate coils for their applications and to direct the coil user to additional literature on building, optimizing, and/or obtaining suitable coils for their desired application. For convenience of classification, RF detection coils for MRS might be divided into two design categories that originate with the two Nobel fathers of NMR, Felix Bloch's wire coils[2,3] and Ed Purcell's 'transmission line' coils.[4]

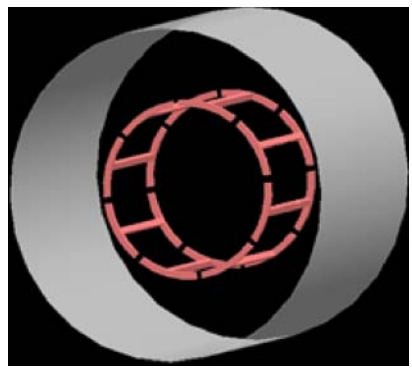

Figure 3.2. NMR detection coil (center, red) within a cylindrical Faraday shield (gray)

3.1.1 Wire Coils

'Wire' is a lay term for coils made of lumped elements or discrete capacitors in resonance with discrete wire or foil inductors. The simplest of these is exemplified by single or multiple looped wire-wound solenoids. These are easy to build and use and are often the most effective designs, especially in applications for which the coil circuit is shorter than $\lambda/10$ at $\boldsymbol{\nu_0}$, where ohmic and radiative losses are negligible and coil currents are uniform and well behaved. These wire designs include

Felix Bloch's first crossed pairs,[3] single-loop solenoid 'surface coils',[5] Helmholtz pairs,[6] and loop arrays.[7]

'Birdcage' coils are another lumped element design typically consisting of a ladder network of rungs wrapped around a cylindrical or ellipsoidal volume former, with the side rails of the ladder joined to form 'end rings'.[8,9] In these designs, the lumped elements, while remaining discrete, are physically distributed around the coil's structure on the rungs and/or end rings. Unlike the simple lumped element wire coils, birdcage coils are most effective when they are electrically adjusted such that the RF completes a full wavelength as it propagates around the ladder network. Such birdcage coils can then be tapped at dual locations physically separated by $\lambda/4$ to provide truly circularly polarized RF sensitivity, known as *quadrature* excitation and detection. This is especially useful for providing uniform fields with maximum SNR over large sample volumes within the bore of cylindrical, superconducting electromagnets. Birdcage designs range from the Alderman–Grant resonator, birdcages, millipede coils, and litz designs.[8,10–13] These ubiquitous coils are readily available commercially and are relatively easy to build.

3.1.2 Transmission Line Coils

Transmission line (transverse electromagnetic, TEM) coils are the distributed circuit analogs of lumped element coils. Their inductance and capacitance, as well as their conductance and resistance, are uniformly distributed around the coil circuit. Transmission lines, consisting of two or more parallel conductors within close proximity, are often the best way to achieve this distributed circuit. Examples of transmission lines are cavities, waveguides, slotted tubes, coaxial lines, microstrips, and stripline structures.[14–19] Robert Pound and Ed Purcell's first coil was based on a re-entrant 'klystron' cavity.[4] Coils built by transmission line principles tend to have a lower inductance and are less radiative. They are therefore better suited to higher resonance frequencies or B_0 and larger sample volumes wherein the coil circuit including the sample cannot be tuned to a single wavelength or less, at $\boldsymbol{\nu_0}$.

3.1.3 Antennas

While coils can be thought of as storing magnetic energy in the near-field, antennas are designed for EM radiation in the 'far field', at distances $>\lambda$. This condition is rarely realized within high-resolution or small-bore horizontal MRS magnets today. However, MRS detection is conceivable in human bore-sized magnets that nowadays can be up to 10.5 T where far-field conditions would apply inside the body. Therefore, antennas are discussed here as well. The simple dipole antenna and dipole arrays are examples.[20]

3.2 SURFACE COILS

3.2.1 Single Loop Coils

The simplest coil circuit can be depicted as an 'RLC loop' as shown in Figure 3.3. Here, R is the electrical resistance (in Ω) of the wire, L is the inductance of the wire loop (in Henries, H), and C is the capacitance (in Farads, F). In this simple coil, L is typically determined by the diameter and number of turns in the loop. The coil diameter should be matched to the size of the sample volume of interest: single loop surface coils are sensitive to approximately a hemisphere of tissue extending from the plane of the coil on the sample surface to a depth of between about one coil radius and a coil diameter. The loop design may surround the sample or be placed against its surface, hence its common name, 'surface coil'. To afford the most efficient energy transfer (and to serve as a band-pass filter), the coil is tuned to resonate at $\boldsymbol{\nu_0}$ for the nucleus being studied by adjusting the value of C in the coil circuit such that $\boldsymbol{\nu_0} = 1/(2\pi\sqrt{[LC]})$. This coil can be used in transmit-only mode, receive-only mode, or with a transmit-receive

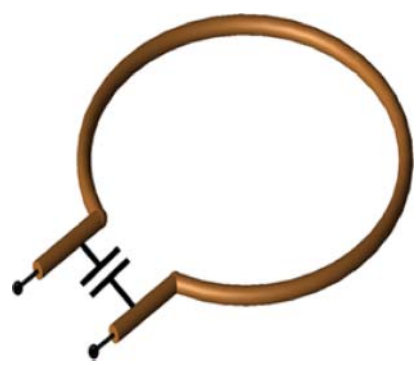

Figure 3.3. Single loop wire solenoid, 'surface coil' with a tuning capacitor connected across its terminals

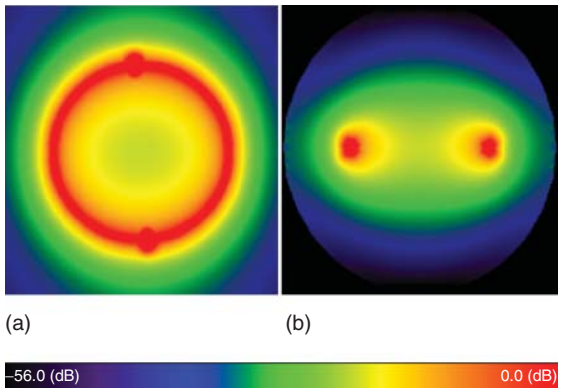

Figure 3.4. The B_1 field in (a) transaxial and (b) axial central planes for the single loop coil in Figure 3.3. Log contour scale is included for this coil

(T/R) switch for both transmission and reception – a transceiver. Two central spatial planes to which the transverse RF magnetic (B_1) field of this coil inductively couples are depicted in Figure 3.4. The red color indicates higher intensity and the yellow and green, lower intensity in these log scale contour plots. An RF current loop like this is also considered to be an RF magnetic dipole because it generates an RF field directed from one 'pole' on one side of the coil through the coil center to another pole on the opposite side of the coil.

Construction of these single loop coils is quite simple, requiring typically less than a meter of, say, ~18 gauge transformer wire or 3-mm copper refrigerator tubing formed into a sample-sized loop and a non-magnetic capacitor with a value typically in the range 10–200 pF (often with a parallel variable capacitor for trimming) soldered into the parallel position shown in Figure 3.3. This capacitor is used to tune the inductive loop resonance to $\boldsymbol{\nu_0}$. Figure 3.5 shows a typical, double-balanced, impedance matching circuit used to match the RF coil when it is loaded by the sample, to a 50-Ω impedance coaxial cable for connection to the MRS scanner. Shown are the coil tuning capacitor, C_t, and two variable impedance-matching capacitors, C_m of approximately equal range, soldered in series with each terminal of the coil. One of these capacitors is soldered to the shield of a coaxial cable and the other is soldered to the center conductor of the cable. When the coil is used as a detector and connected to the scanner's sensitive preamplifier receiver, the coil must be isolated from the transmit power using a transmit-receive (T/R) switch (see Section 3.2.3).[21]

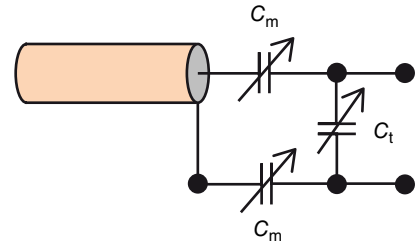

Figure 3.5. Coil-cable, double-balanced matching circuit. Capacitors C_m are adjusted to match the coil to the cable (typically 50 Ω) and should be approximately equal, while C_t is adjusted to tune the coil to resonance

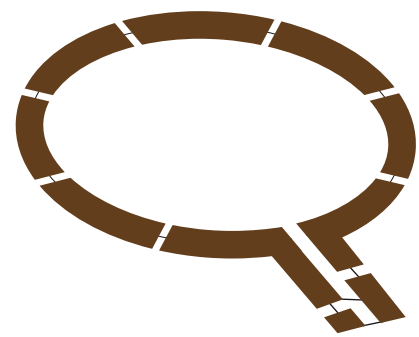

Figure 3.6. Single loop surface coil, capacitively split, made from foil solenoid. Distributed tuning capacitors (not shown) are used to bridge the gaps

To allow tuning to higher resonant frequencies with larger sized surface coils, the coil conductor can be split and the tuning capacitance distributed around the coil with discrete elements bridging the gaps as shown in Figure 3.6. This coil is depicted as being constructed of foil. The B_1 fields of this split coil (Figure 3.7) are similar to those of Figure 3.4. Adding lumped capacitance across multiple splits in the coil loop in this manner is a significant advance that reduces the effect of capacitive coupling and electric (E)-field losses between the coil and the sample by breaking up the voltage difference between the coil and the sample.

Surface coils may be constructed of wire or foil and may be shaped in three-dimensional (3D) geometries and sizes to best fit and couple to a region of interest (ROI). Figure 3.8 shows a square 'saddle-shaped' surface coil conformed to a cylindrical surface. Cryogenically cooled and superconducting versions of a single loop coil that can significantly enhance SNR when sample noise is not dominant, can be bought

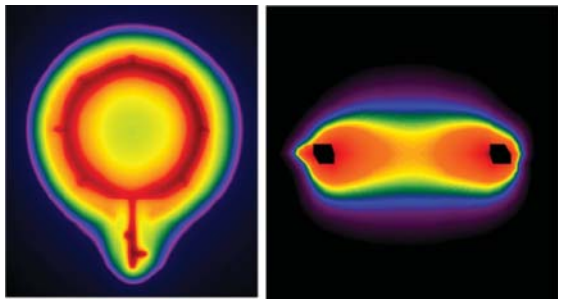

(a) (b)

Figure 3.7. B_1 field in the (a) transaxial and (b) axial central planes for the single loop, split coil in Figure 3.6 (scale is similar to Figure 3.4)

Figure 3.8. Rectangular, sample-conforming saddle-shaped, foil solenoid surface coil. The B_1 field in this case is ditected primarily horizontal in this diagram

commercially.[22–24] One constraint to keep in mind is that these coils must be oriented such that the axis of the coil is generally perpendicular to the axis of the magnet bore to maximize transmit and/or receive efficiency. These loops can also be double tuned for observing two nuclei either serially or simultaneously in an NMR experiment, depending on the way the coil is interfaced to the MRS system and the pulse sequence protocols used.[25]

3.2.2 Multiple Concentric Loops

Multiple loop elements may be configured in an array about a sample to accomplish various objectives.

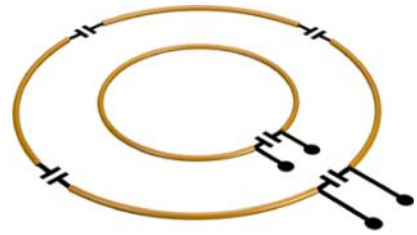

Figure 3.9. Concentric loops surface coil. The outer coil is split and fitted with distributed tuning capacitors

Concentric loops as shown in Figure 3.9 can be used for localizing a small ROI by field profiling, or when it is desired to provide a uniform excitation field from the larger coil, over the sensitive volume of the smaller one, e.g., for MRS quantification. In this case, the coils are separately connected to the transmitter and receiver but must be electronically decoupled from each other as they are coaxial. Alternatively, the concentric coils can be used for multinuclear MRS wherein each loop is tuned to a different NMR frequency.[26] For multinuclear applications, the larger of the two loops might be used for proton (^{1}H) scout imaging, shimming, decoupling, and/or Overhauser enhancement (nuclear Overhauser effect, NOE; see Chapter 1), while the smaller loop is used to acquire spectra from a second nuclear species. In this case, both coils are used in transceiver mode, with each is connected to its tuned matching network, T/R switch, filter, preamplifier, and power amplifier.

3.2.3 Phased Arrays

Multiple loops can also be configured into phased-arrays of nonconcentric coils as shown in Figure 3.10.[7] Phased arrays, used as surface or volume coils, extend the performance of an electrically small and efficient loop to an arbitrarily large field-of-view (FOV). Phased arrays are most often used as application-specific, receive-only detectors that operate in conjunction with a larger, uniform transmit coil such as the body coil of a clinical magnetic resonance imaging (MRI)/MRS system.[27–29] Each loop is connected to its own receiver channel often beginning with a low-noise gallium–arsenide field-effect transistor (GaAsFET) decoupling preamplifier embedded in each loop (see Chapter 2).

As in the case of the single coils, the multiple preamplifiers connected to each loop in the array

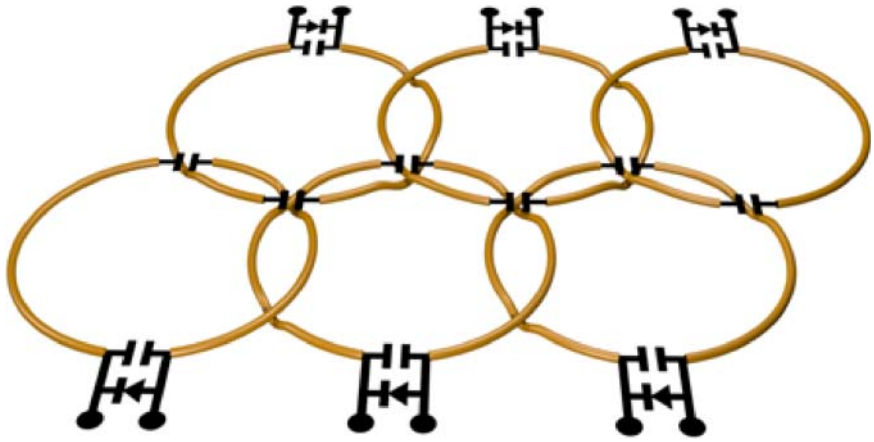

Figure 3.10. Six-channel phased array comprised overlapping split circular surface coils

must be protected at the loop element terminals from excessive induced voltages during transmission, and each loop must be actively detuned during the RF transmit pulse periods because the induced currents will otherwise oppose the transmit field. This is achieved by a scanner-activated high-voltage limit, low-noise, positive-intrinsic-negative semiconductor (PIN) diode circuit like that shown in Figure 3.11. Basically, the scanner provides a voltage (V_{DC}, typically 5–15 V) during transmission that turns on the diode and shorts out the tuning capacitance, detuning the coil. Figure 3.10 depicts a single diode in each loop to represent this detuning circuit in a six-coil array with distributed tuning capacitance. Transceiver arrays that use the coil elements for both excite and receive will make use of a PIN diode T/R switch only, to switch the coil terminals sequentially between the power amplifier during transmission (to protect the receiver) and to the receiver during reception.

The loops in the array must also be isolated from their neighbors to decouple correlated sample noise and optimize parallel imaging performance by insuring that the signals from the multiple channels are as independent as possible. This decoupling is accomplished by cancelling the mutual inductance between neighboring loops by means of capacitive or inductive adjustments. This typically begins with careful adjustment of the overlap between adjacent loops, such as shown in Figure 3.10, to ultimately achieve an isolation of around 12 dB (network analyzer S12 measurement) or more for best coil operation. The larger transmit volume coil must also be detuned during signal reception. This detuning is also achieved

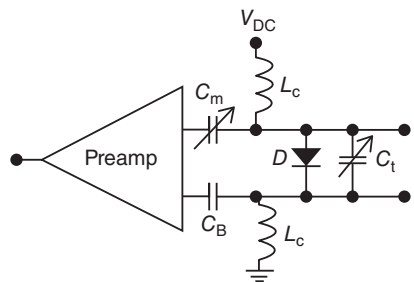

Figure 3.11. Parallel PIN diode (D) and preamplifier detuning circuit for one channel of a receiver phased-array. The diode is switched on by voltage V_{DC} from the scanner during excitation. The V_{DC} signal can be conveyed on the receiver output line, capacitively decoupled from the preamplifier. C_B, C_m, and C_t are tuning and matching capacitors

by scanner-activated PIN diode circuits in the transmit coil that shunts signal to ground or produces an open circuit as in Figure 3.11 or 3.12, respectively.

Arrays bring multiple advantages to MRS. They can be tuned to more than one nucleus by double tuning each loop or by tuning adjacent loops to alternate frequencies. As receiver/detectors, arrays offer a means of covering larger ROIs more efficiently with electrically smaller, less radiating coil elements than large volume coils or loops. In this respect, phased-arrays may be considered volume coils in their own right, other variations of which are discussed later. Receiver arrays can greatly enhance SNR[7] as well as the speed of data acquisition through parallel imaging and multiband techniques.[27–29] As transmit elements, they can be used for optimizing B_1 homogeneity at higher B_0 field

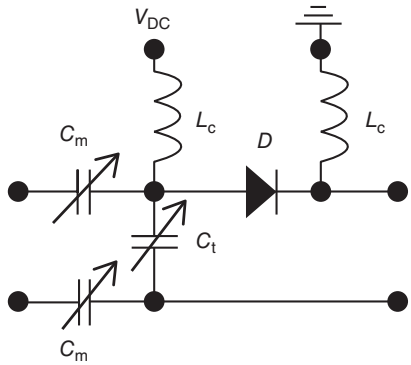

Figure 3.12. Series PIN diode detuning circuit for transmit phased array elements

strengths, where wavelengths are short in tissue, for minimizing RF power deposition over an ROI by field profiling, B_1 shimming, and 'beam-steering' selective excitation techniques. For all of these reasons, the use of phased arrays is widespread, at least for ^{1}H MRI and MRS. Their availability for non-^{1}H nuclei, however, is more limited.

3.3 VOLUME COILS

3.3.1 Solenoids

Wire-wound solenoids are one of the earliest choices of volume coil design. Figure 3.13 shows a multiturn solenoid whose purpose is to extend and intensify the linear B_1 field of a single loop along the axis of the RF coil. Such a coil, with multiple turns around a volume, has significantly higher coil inductance than single-turn designs and thus requires a proportionately lower tuning capacitance. Owing to its high inductance, this design is most effectively used as a simple transceiver coil for small laboratory animals, excised tissue samples, or test tube or capillary samples bearing lower gyromagnetic ratio nuclei where a lower-$\boldsymbol{\nu_0}$ coil is required. In addition to being a good performer for small samples at lower frequencies, this is a simple and easy coil to build and use in the laboratory.

3.3.2 Crossed Pairs

Felix Bloch's crossed-coil design is shown in Figure 3.14.[3] This design is comprised of a pair of independent loops and can be used in two ways. Bloch connected one loop to his transmitter and the other loop to his receiver. When the loop planes are crossed or perpendicular as shown, the transmit field of one loop is geometrically isolated from the received field of the other loop. Another use for this loop pair is to generate a quadrature or circularly polarized transmit and/or receive field. In such a coil set, the transmit (receive) signal is divided into two and separately fed to (detected from) each coil with a 90° phase shift. Circularly polarized excitation provides a more uniform field over a larger FOV in the sample than using one or both coils without the quadrature excitation, and the SNR of the NMR signal detected in quadrature from the sample will be improved by as much as a $\sqrt{2}$-fold.

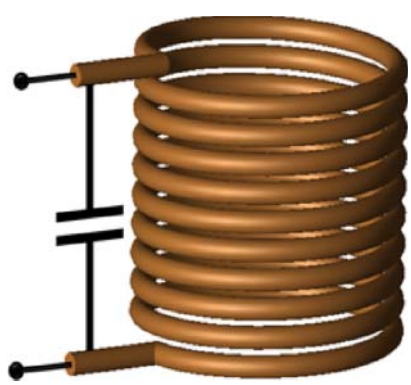

Figure 3.13. Multiloop wire solenoid with tuning capacitor connected across its terminals. The B_1 field is primarily in the vertical direction in the diagram

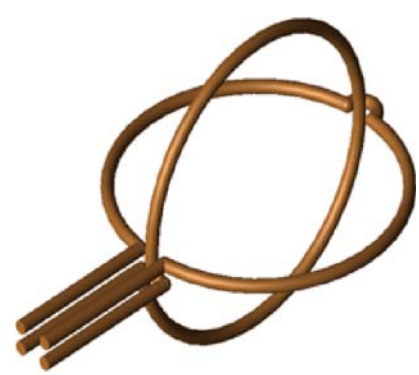

Figure 3.14. Crossed wire loops depicted as a two-coil orthogonal pair. The B_1 field is in the plane perpendicular to the four-feed terminals

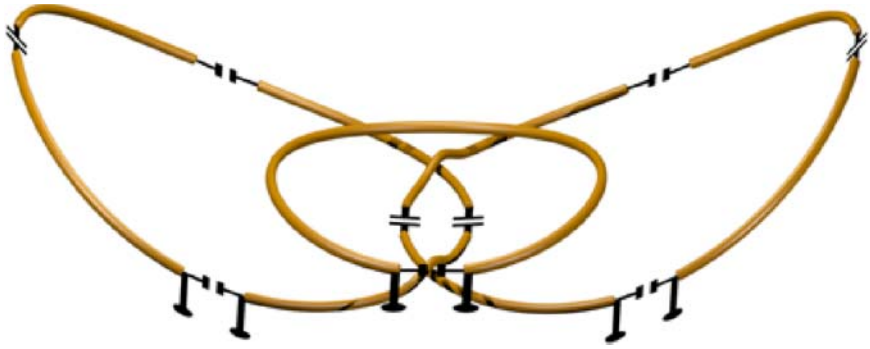

Figure 3.15. Quadrature surface coil formed from a crossed-coil pair with a third nested loop for use as a three-channel phased array or a multi nuclear applications with the inner coil used for MRS of a low-sensitivity nucleus

A third way to use this coil is as a double-tuned or multinuclear coil. In this case, one of the two loops is tuned to the $\boldsymbol{\nu_0}$ of a first nuclear species and the second loop is tuned to the $\boldsymbol{\nu_0}$ of a second nuclear species. Such a crossed-Bloch pair can be used to excite and/or detect two different MRS signals from two different species to perform heteronuclear decoupling, spectral editing, or NOE (as with the coil pair in Figure 3.9). These coils can be used as transmit-only coils, receive-only coils, or transmit and receive coils. Again however, the axes of this coil pair must be oriented substantially perpendicular to $B_{0,}$ and despite having more open space than the solenoid that obstructs the magnet bore when used in vertical bore magnet configurations, access to its central sample space remains somewhat obstructed.

One potentially useful variation, which might be considered either as a three-channel phased array or as a form of crossed-coil design, is shown in Figure 3.15. Here, the crossed pair is opened and spread over a curved, anatomic surface, while still achieving a quadrature field over a portion of the sample space. This configuration can be useful as a quadrature transceiver for imaging. Alternatively, it can be combined with a second transceiver loop tuned to a low gyromagnetic ratio nucleus and nested at the intersection of the larger crossed pair to provide efficient, local ^{1}H MRI performance, and sensitive non-^{1}H MRS.[30,31]

3.3.3 Saddle Pairs

The series-wound saddle pair shown in Figure 3.16 can be viewed as a two-loop solenoid but wound to efficiently and conveniently accommodate a sample in a linear B_1 field perpendicular to the magnet's B_0 field, with the desired cylindrical access.[6,32–34] More desirable for some applications is the combination of two such saddle pairs with each pair rotated 90°, in the configuration pictured in Figure 3.17. This crossed saddle pair can be used in all of the ways possible with the crossed pair of Figure 3.14, but in a much more space-efficient design for performing NMR in cylindrical bore superconducting magnets. This coil can generate a fairly uniform circularly polarized B_1 over its entire volume that is perpendicular to the magnet bore and to the coil's cylindrical axis, by separately exciting each pair with two RF signals phase shifted by 90°, as discussed earlier. To minimize coupling and maximize isolation between the two saddle pairs for best SNR and quadrature performance and to cover the largest volume FOV, the overlap between the two pairs is adjusted to cancel or minimize the mutual inductance between the loops. The amount of overlap

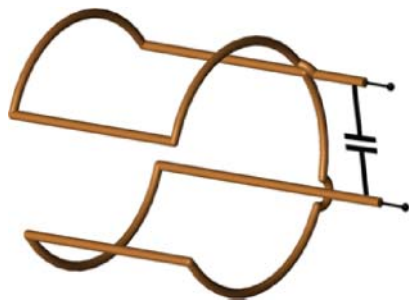

Figure 3.16. Series wound saddle pair (compare with Figure 3.8) with a tuning capacitor. The B_1 field is primarily in the vertical direction

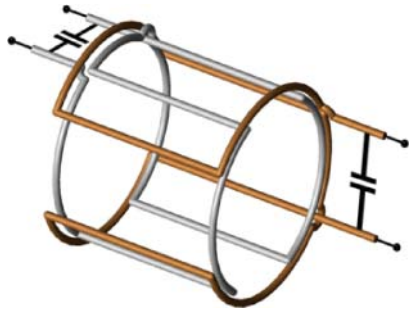

Figure 3.17. Two series-wound crossed wire saddle pairs rotated so that their B_1 axes are orthogonal to form a crossed saddle pair

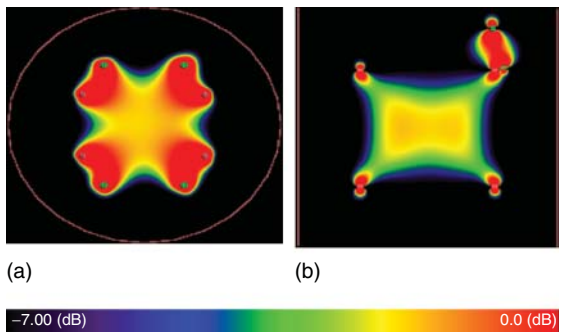

Figure 3.18. B_1 field in the (a) transaxial and (b) axial center planes for the circularly polarized crossed-wire saddle pairs of Figure 3.17. The log color scale for this figure applies to all following field contour figures

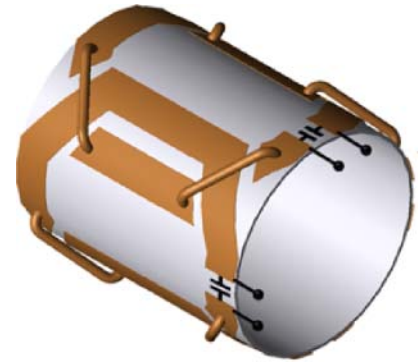

Figure 3.19. A crossed foil saddle pairs with wire jumpers spanning the crossover points

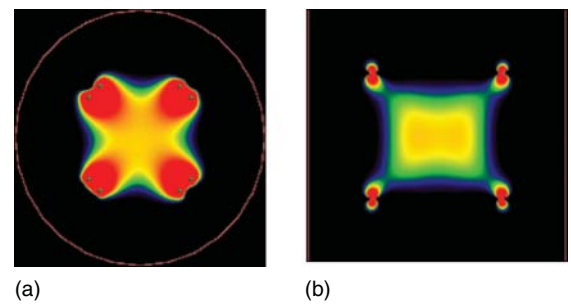

Figure 3.20. B_1 field in the transaxial and axial center planes for the circularly polarized crossed-foil pairs in Figure 3.19

depends on the coil dimensions and the sample loading and is typically determined empirically by adjusting the size and orientations of the coils until a maximum isolation (e.g., an S12 > 12 dB measured on a network analyzer) is achieved. As with the crossed-Bloch pair, each saddle pair can also be used as separate transmit and receive coils, or tuned to the NMR frequencies of two different nuclei for multinuclear MRS. Many modern MRS detector coils use variations of the crossed saddle pair design. The fields in the transaxial and axial central planes for this coil are shown in Figure 3.18.

Saddle pairs can be constructed from foil as well, as illustrated in Figure 3.19. Foil may be used for ease-of-fabrication. For example, foil coil elements can be milled, etched, or glued to a supporting member with ease, accuracy, and precision from circuit board material or copper tape. The substrate material can add to the stability of the coil circuit as well. To avoid parasitic capacitance between overlapping loops separated by thin insulation, wire jumpers can be used (Figure 3.19). While the electrical quality factor Q ($=2\pi\nu_0$ L/R), a measure of the efficiency of an RF circuit, may be a bit lower with foil loops vs wire loops or copper tubing, the FOV coverage of a foil-etched coil is very similar to a wire wound coil of the same dimensions (compare Figures 3.18 and 3.20).

If the two opposing sides of each saddle coil are not connected in series but are instead isolated for connection to their own receiver preamplifier or RF power source, a four-channel cylindrical volume coil results, as shown in Figure 3.21. The four channels can be used as a multichannel transmit and/or receive volume coil array, or for multinuclear MRS applications wherein one or more of the individual coil elements is tuned to a different NMR frequency, to enable combined ^{1}H MRI, MRS, or decoupling experiments,

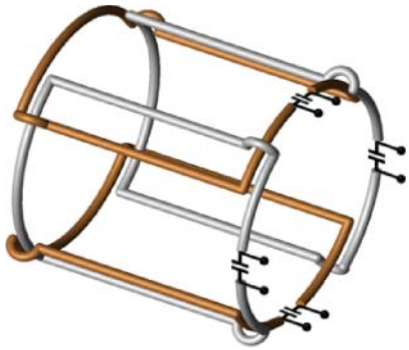

Figure 3.21. Four-loop wire volume coil formed from four saddle coil loops on a cylindrical former. The B_1 field is in the plane perpendicular to the cylindrical axis

Figure 3.22. Four-loop volume coil fabricated from foil saddle coil elements with wire jumpers spanning the crossover points

as discussed earlier. Such designs mark the evolution toward multielement volume coils. Figure 3.22 shows a version fabricated with foil and wire jumpers.

3.3.4 Slotted Tube Resonator

Another coil design fabricated from foil on a cylindrical former is the 'slotted tube resonator' of Alderman and Grant shown in Figure 3.23,[8] used for early 1.5 T MRI. It is composed of a pair of end-rings connected by two broad opposing conducting sections that tend to reduce inductance that facilitates tuning at higher ν_0, leaving windows that span about 100° on opposite sides of the tube (the 'slot'). Similar to the split surface coils, the end conductors are split in four places to accommodate distributed tuning capacitors. Electrically,

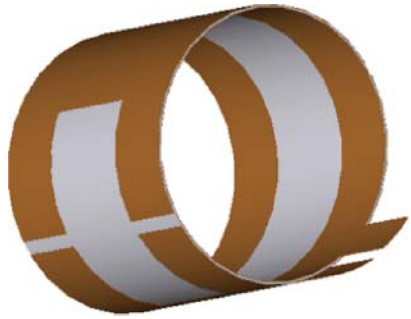

Figure 3.23. Alderman–Grant coil. The copper strut on top is mirrored on the bottom and the B_1 field is directed left-right through the window

the structure is analogous to connecting two end-rings with distributed capacitance in parallel via the broad axial sections, to form a tuned LC circuit.

3.3.5 Birdcage Coils

As noted in Section 3.1.1, birdcage coils are wire or foil wound, lumped element coil circuits based on ladder rather than loop or solenoid circuits.[8,10–13,35–38] The birdcage coil achieves a uniform B_1 field within its typically cylindrical volume by applying a 360° azimuthal distribution of linear currents surrounding the volume. The return paths for these linear current elements is on end rings, and the ladder rungs provide current paths connecting them. In theory, an infinitely long birdcage fitted with an infinite number of rungs would achieve perfect field uniformity within the coil volume. However, a 'square' coil whose length equals its diameter or shorter is sufficient for most MRI and MRS, FOVs.

The electrical circuit of a birdcage coil is equivalent to a narrow-bandwidth filter circuit whose center frequency can be tuned to ν_0 with lumped tuning capacitances distributed either in the rungs (low-pass birdcage), or with capacitance distributed in the end rings ('high-pass birdcage'; Figure 3.24), or with lumped capacitance distributed in both the rungs and the rings (band-pass birdcage). Each design has performance advantages and disadvantages that depend on the NMR frequency and the application.[10,11,38] The high-pass coil can achieve higher frequencies – an important feature – but can present sample loading problems. All the birdcage structures are symmetric and can be driven and/or the signal received as a circularly polarized coil to achieve the best SNR and

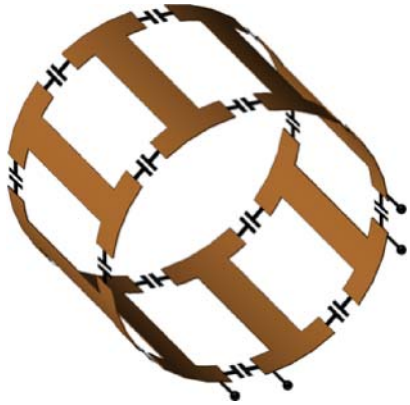

Figure 3.24. High-pass bird cage coil with feed ports spaced at 90° for quadrature excitation or detection

FOV coverage. For quadrature operation, transmit and/or receive cables are attached 90° apart at the terminal positions shown, using the matching circuit of Figure 3.5 at each input. As in Section 3.3.2, when used for transmission the RF power must be provided as two channels that are 90° phase shifted at the two coil ports. This can be accomplished using a single RF power amplifier and a 'quadrature hybrid' circuit. The same hybrid can be used to recombine the two, 90° phase-shifted receive channels representing the circularly polarized (B_1) NMR signal, to feed a single receiver channel in the simplest transmit and receive interface for these coils.

While ubiquitous transceiver head coils are still in use, the most common modern application for the birdcage is for uniform transmit coils used in conjunction with phased-array receiver coils. Because clinical transmit coils are very large, these big resonators require a significant number of capacitive breaks in both the rings and the rungs to render a band-pass coil. Such coils operate on the edge of self-resonance, are very radiative, and require large (e.g. 32-kW) pulsed power amplifiers to drive them. The RF power deposition from these lossy radiators presents significant limitations to RF protocols. Accordingly, the utility of birdcage transmitters becomes limited for most larger preclinical and human applications at 3 T and above, the field at which many MRS applications begin. Birdcages almost always operate inside a Faraday shield (Figure 3.2). The center-plane birdcage B_1 fields calculated in Figure 3.25 show the characteristic FOV for this uniform transmitter. The end-rings tend to cancel the MRI/MRS signal, causing a concave B_1 field cut off at the ends of the coil. This can be advantageous, as it prevents signal aliasing from beyond the coil volume.

Birdcage coils can also be double tuned for multinuclear MRS. A common design approach for double tuning a birdcage is to add a second set of end rings, effectively creating two coils of different electrical lengths in a single circuit.[35]

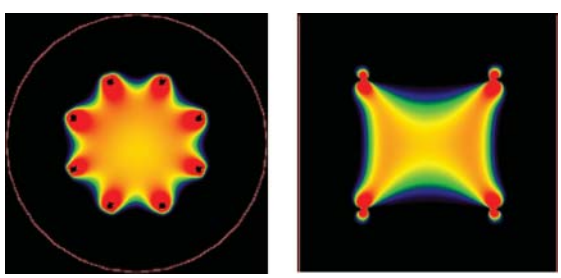

(a) (b)

Figure 3.25. B_1 field in the (a) transaxial and (b) axial central planes for a circularly polarized bird cage coil

3.3.6 Millipede Coils

The Varian Inc. millipede MRS coil was a favorite that is still produced privately by its inventor, Ernest Wong at Extend MR, LLC.[13,37] The millipede coil is analogous to a foil made low-pass birdcage design that maximizes the number of rungs. The tuning capacitance is displaced to each end of the coil rather than in the middle: it is distributed in the foil rung–ring overlap at the ends of each rung. The benefit of this design is its high uniformity over most of the volume of the coil. See the millipede coil and its field contours

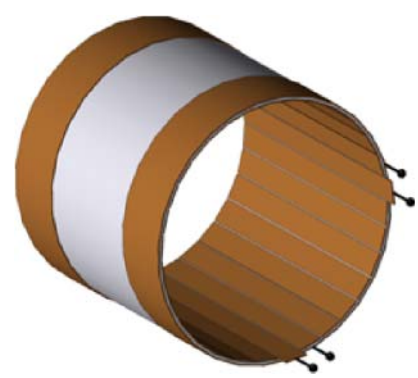

Figure 3.26. Millipede coil

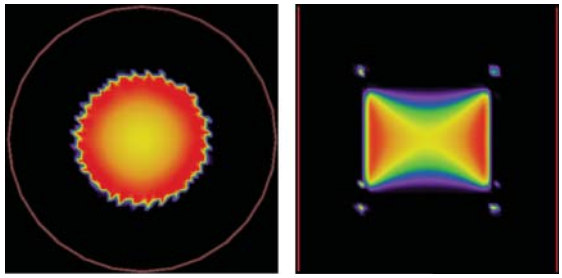

Figure 3.27. B_1 field, (a) transaxial and (b) axial for circularly polarized millipede coil

in Figures 3.26 and 3.27. It is operated mostly as a circularly polarized transceiver coil with its transmit and receive terminals set 90° apart.

3.3.7 Litz Coils

Litz coils are a wire or foil wound, lumped element cage coil variant that are produced and sold to many users by Doty Scientific, Inc., Columbia SC.[12,36] 'Litz' meaning braided or woven refers to the woven appearance of these coils. This design uses capacitive overlaps by its foil rungs and rings to achieve a tuned cage-like mode of operation. While few MRS experimentalists build these intricate coils, they are well made by their manufacturer and are widely used in the mostly vertical bore and preclinical horizontal bore markets. For simplicity of viewing, a linear litz coil is shown in Figure 3.28 with the B_1 fields produced in Figure 3.29. Circularly polarized and double-tuned litz coils are more common and show good performance.[36] A linear cage-like field contour is apparent.

Figure 3.28. Litz coil configured for linear operation. The B_1 field is vertical through the windows, top and bottom

3.4 TRANSMISSION LINE COILS

As noted earlier, the first MRS coil built by Robert Pound for Ed Purcell was a re-entrant klystron transmission line design based on microwave radar research.[4] Any circuit that propagates a TEM wave defines a transmission line, and the name 'TEM' is applied to this class of coil circuits. TEM coils include coaxial, stripline, and microstrip transmission lines, as well as resonant cavities and waveguides.[17–19,39–43] The primary objective for employing these designs is to achieve high efficiency and uniform current and field distributions at high B_0 and Larmor frequencies and large sample volumes including human systems. The lumped element circuits that are comprised of the discrete inductors and capacitors employed in the wire-wound coils described earlier, are inherently low-frequency devices. Their design equations are approximated by Thevenin's and Kirchoff's equivalent circuit equations, and their fields are approximated by the Biot–Savart Law.

When circuit wavelengths exceed about a tenth of a wavelength, they begin to radiate energy like an antenna. As the sample sizes remain the same and the wavelengths decrease with increasing B_0 and $\boldsymbol{\nu_0}$, lumped element designs must be abandoned in favor of transmission line designs, and calculations based on Maxwell's time-dependent field equations. Similar to ultra-high-frequency (UHF) circuits in the telecommunications industry, UHF NMR coils benefit from transmission line (TEM) design. With such designs, there are few lumped elements other than trimmer capacitors and chokes (inductors). The bulk of the inductance, capacitance, conductance, and small resistances of the coil antenna are parameters in transmission line equations and are continuously distributed throughout the TEM circuit. The TEM coils have high Q values that provide for efficient operation at higher operating frequencies where lumped element devices become problematic or no longer work, but where MRS shows much promise.

An early example of a transmission line coil for MRS is the Schneider and Dullenkopf, slotted tube resonator pictured in Figure 3.30.[14,15] The transmission line nature of this coil is easy to see from the outer conductor serving as a shield, with a coaxial, albeit hollow, center conductor containing the sample space.

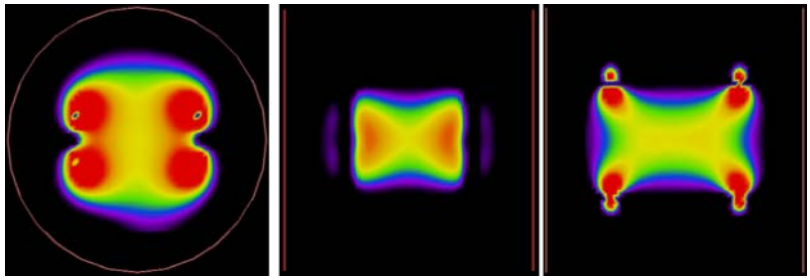

Figure 3.29. Transaxial B_1 in the (a), *xz* (b), and *yz* (c) axial central planes of the linearly polarized litz coil in Figure 3.28

Figure 3.30. Slotted tube resonator

The transmission line parameters are distributed over the length of this structure, between the shield and the center conductor plates. This design has evolved into a more useful and widely used 'TEM' design for ultra-high-field systems of $B_0 \geq 4$ T, as pictured in Figures 3.31 and 3.32.[17,18,39]

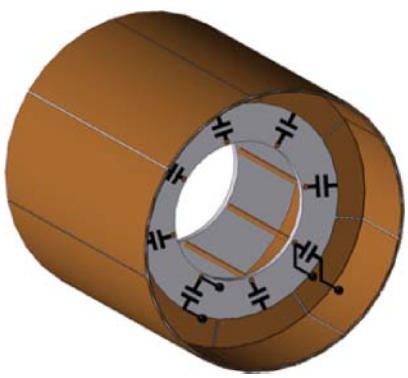

Figure 3.31. An inductively coupled coaxial line TEM coil

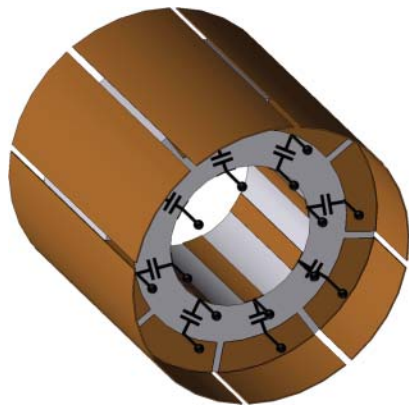

Figure 3.32. An actively coupled TEM coil formed from striplines

3.4.1 TEM Coils: Coaxial Lines, Striplines, and Microstrips

Modern TEM coils are capacitively shortened and tuned, half-wave transmission line resonators that, while using similar principles to early tube resonator designs, possess practical features for modern utility, such that their final appearance may bear little resemblance to the slotted tube resonator.[19,39–43] Among these features, the center conductor 'rungs' of these coils generate a highly uniform field like the rungs of a birdcage. Unlike the end-ring-connected birdcage coils, however, the rung conductors of the TEM coil are not connected at all. Their current return path is on the shield of the coil, as in a transmission line. This feature produces several benefits. First, each rung in the TEM coil is an electrically short and efficient, independent resonator: the TEM coil is effectively an array of these discrete resonant units. The useful

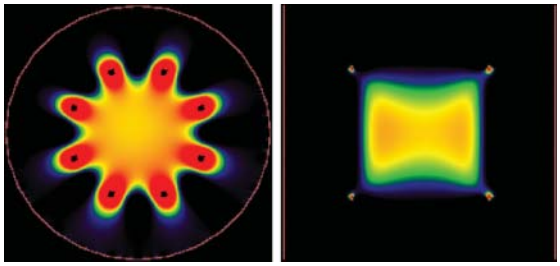

Figure 3.33. B_1 field in the (a) transaxial and (b) axial central planes of a circularly polarized TEM coil

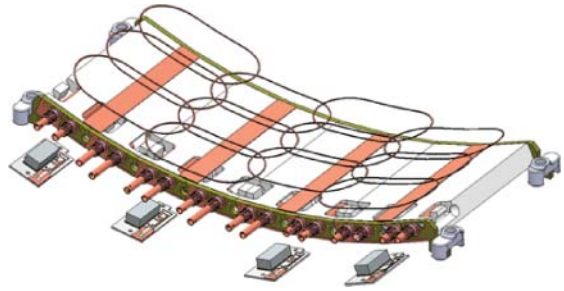

Figure 3.34. TEM surface array combined with a nested loop phased array. The loops are centered over the striplines

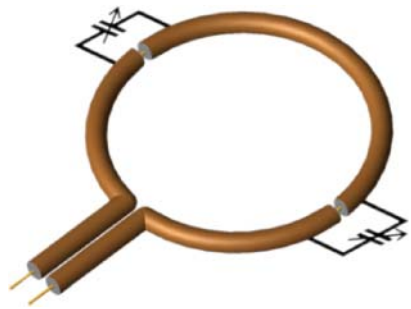

Figure 3.35. Transmission line, double-tuned surface coil

frequency of this coil therefore depends on the inductance of a single rung only and not on the circuit size of the whole coil as in the case of the end-ring-coupled birdcage coil. TEM coils have been shown to produce efficient body coils to 8 T and above.[39,44]

Second, because each element operates independently of the next, the individual elements can be separately driven by a different transmit signal with 5 degrees-of-freedom, namely phase, magnitude, frequency, space, and time. This allows for B_1 shimming, beam-steering spatially selective excitation, parallel imaging, and multiband operation. In addition, because there are no end-ring field cancellations, the FOV for a TEM coil is longer and more uniform than a birdcage of equal length. Compare the TEM field contours of Figure 3.33 to the birdcage contours of Figure 3.25. As with the birdcage, these coils can be used as receivers, transmitters, or transceivers.

While cylindrical volume coils are shown in Figures 3.30–3.32 because TEM coils are essentially an array of independent transmission line elements, they can be conformed to many useful spatial forms. A common example is the TEM surface array (Figure 3.34) used for ultra-high-field body MRI and MRS.[39] The TEM coil can also be double tuned by tuning adjacent rungs to an alternate NMR frequency of a desired nucleus. As with most double-tuned coils, an ^{1}H frequency is typically chosen for scout imaging, landmarking, shimming, and sometimes decoupling, and a second, non-^{1}H nucleus is tuned for MRS. This coil works quite well because the coil couples to the same sample volume for both nuclei, achieving comparable sensitivity at two frequencies as its single-tuned counterpart owing to the independent operation of the individual resonators.

Figure 3.34 shows a commonly used TEM configuration of linear transmit elements paired with a loop array receiver. Linear transmit elements in a surface array such as this, or in a volume coil, are relied upon for generating a more uniform B_1 excite field than is achievable with small single elements, while a close-fitting phased array next to the sample acts as a sensitive signal detector. Note that when linear transmission line elements are used in this way, a geometric field decoupling is realized when the loop elements are centered over the line elements. The assembly shown can be used in a number of ways. It can be used as a surface array for covering a larger ROI than achievable with single elements. When this is paired with another similar assembly on the opposite side of a body, it is very effective and efficient for body imaging, as compared to a whole body cylindrical coil of similar design.

3.4.2 Other Transmission Line Coils

TEM coils can take other forms as well. For example, the double-tuned surface coil pictured in Figure 3.35 is constructed from a section of semi-rigid coax cable, although the same coil could be executed with

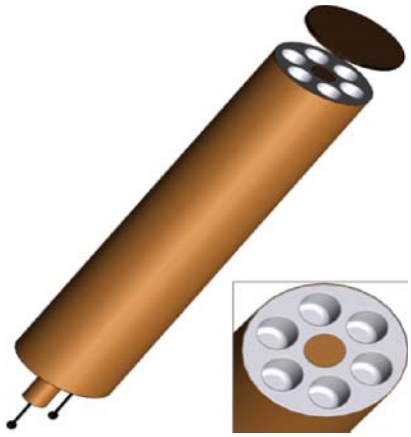

Figure 3.36. Open and short stubline coils

stripline or microstrip. In this coil, the continuous center conductor is tuned by circuit length and trimmer caps to a lower frequency, and the split shield is tuned with trimmer capacitors to a higher frequency. Most of the reactance of the coil is continuously distributed in transmission line manner to yield a balanced multinuclear surface coil.[1]

Another interesting transmission line design for high-resolution MRS is pictured in Figure 3.36.[19] As seen in Figures 3.36 and 3.37, a B_1 field of maximum intensity is generated at the tip of a resonant, halfwave coaxial line. Sample space is drilled into the dielectric between the outer and center conductor of the semirigid coaxial line section. For maximum efficiency, this dielectric can be selected to match the sample in order to minimize reflection and losses. This 'stubline' coil seems well suited for high-resolution, vertical bore magnets. The same approach could be extended to horizontal bore systems using dielectric wave guides with access holes or apertures cut though the waveguide sidewalls at current nodes that couple to anatomy at those points with maximum efficiency. These structures can be double tuned by appropriate choices of dielectric inside and outside of the cavity.[19] The inside of the cavity 'sees' one wavelength and the outside of the cavity sees another, typically either air or tissue.[45]

3.5 ANTENNAS

Finally, we conclude with a third coil-circuit class, the antenna.[20] While the wire and transmission line coils

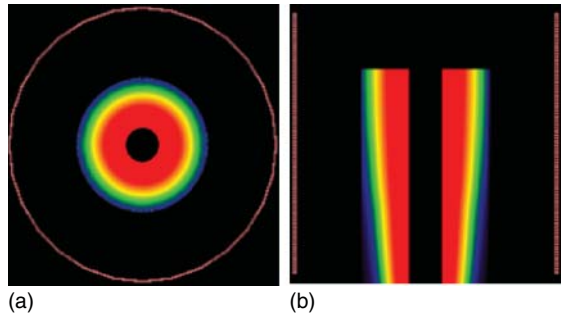

Figure 3.37. B_1 field, both (a) transaxial and (b) axial, for stubline coils

above are designed to store an RF magnetic field within or adjacent to their circuit, an antenna is designed to radiate its energy efficiently to the far field. Using an antenna may be appropriate when a sample ROI is in the far field ($>\lambda$). This condition occurs for MRI and MRS at the highest B_0 and largest physiological samples. This class of detectors has proved successful for reaching deep body ROIs at $B_0 = 7$ T (300 MHz) to 10.5 T (450 MHz), for example. Antennas comprised arrays of center-fed dipoles, as pictured in Figure 3.38, have been built and tested and found to perform favorably compared to TEM coil arrays under these highest field conditions for human MRI/MRS. Compare the field contours of the dipole in Figure 3.39 to the TEM contours in Figure 3.33. Because, like the TEM coils, these arrays have no end-rings, the axial field extends further, and more uniformly than a birdcage of equal physical length. However, the birdcage would

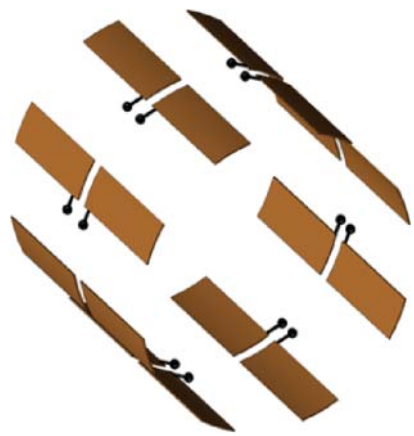

Figure 3.38. Dipole array arranged around a cylindrical sample chamber

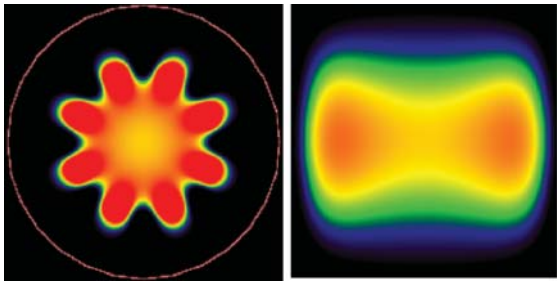

(a) (b)

Figure 3.39. B_1 field, (a) transaxial and (b) axial, in the central planes of the dipole array in Figure 3.38

not work at these highest frequencies and sample dimensions. Similar to TEM coils and other array structures, these dipole antennae can be double tuned by tuning alternating elements in the array to alternating frequencies.

REFERENCES

1. J. T. Vaughan, in Ultra High Field Magnetic Resonance Imaging, ed. P. Robitaille, Springer Academic/Plenum Publishers: New York, NY, 2006, Chap. 6. RF Coils, 127.
2. F. Bloch, *Phys. Rev.*, 1946, **70**, 460.
3. F. Bloch, W. W. Hansen, and M. Packard, *Phys. Rev.*, 1946, **70**, 474.
4. E. M. Purcell, H. C. Torrey, and R. V. Pound, *Phs. Rev.*, 1946, **69**, 37.
5. J. J. Ackerman, T. H. Grove, G. G. Wong, D. G. Gadian, and G. K. Radda, *Nature*, 1980, **283**, 167.
6. D. I. Hoult, C. N. Chen, and V. J. Sank, *Magn. Reson. Med.*, 1984, **1**, 339.
7. P. B. Roemer, W. A. Edelstein, C. E. Hayes, S. P. Souza, and O. M. Mueller, *Magn. Reson. Med.*, 1990, **16**, 192.
8. D. W. Alderman and D. M. Grant, *J. Magn. Reson.*, 1979, **36**, 447.
9. C. E. Hayes, *Magn. Reson. Imag.*, 1993, **11**, 81.
10. C. E. Hayes, *NMR Biomed.*, 2009, **22**, 908.
11. C. E. Hayes, W. A. Edelstein, J. F. Schenck, O. M. Mueller, and M. Eash, *J. Magn. Reson.*, 1985, **63**, 622.
12. F. D. Doty, G. Entzminger Jr, and C. D. Hauck, *J. Magn. Reson.*, 1999, **140**, 17.
13. Wong W. H. and Sukumar S., Millipede Coils. Varian, Inc. (Palo Alto, CA), assignee. United States patent 6285189, 2001.
14. H. J. Schneider and P. Dullenkopf, *Rev. Sci. Instrum.*, 1977, **48**, 68.
15. H. J. Schneider and P. Dullenkopf, *Rev. Sci. Instrum.*, 1977, **48**, 832.
16. P. H. Röschmann, Surface Coil for High-frequency Magnetic Fields for Magnetic Resonance Examinations. U.S. Philips Corp. (New York, NY), assignee. United States patent 4775837, 1988.
17. J. T. Vaughn Jr., Radio Frequency Volume Coils for Imaging and Spectroscopy. UAB Research Foundation (Birmingham, AL), assignee. United States patent 5557247, 1996.
18. J. T. Vaughan, H. P. Hetherington, J. O. Otu, J. W. Pan, and G. M. Pohost, *Magn. Reson. Med.*, 1994, **32**, 206.
19. J. T. Vaughan, RF Coil for Imaging System. Massachusetts General Hospital (Boston, MA), assignee. United States patent 7268554, 2003.
20. A. J. E. Raaijmakers, in RF Coils for MRI, eds J. T. Vaughan and J. Griffiths, John Wiley and Sons, Ltd: Hoboken, NJ, 2012, Chap. 17. Antennas as Surface Array Elements for Body Imaging at Ultra-high Field Strengths.
21. D. M. Petersen, in RF Coils for MRI, eds J. T. Vaughan and J. Griffiths, John Wiley and Sons, Ltd.: Hoboken, NJ, 2012, Chap. 25. Impedance Matching and Baluns.
22. S. Junge, in RF Coils for MRI, eds J. T. Vaughan and J. Griffiths, John Wiley and Sons, Ltd: Hoboken, NJ, 2012, Chap. 20. Cryogenic and Superconducting Coils for MRI.
23. H. Kovacs, D. Moskau, and M. Spraul, *Prog. Nucl. Mag. Res. Sp.*, 2005, **46**, 131.
24. P. Styles, N. F. Soffe, and C. A. Scott, *J. Magn. Reson.*, 1989, **84**, 376.
25. B. L. Beck, in RF Coils for MRI, eds J. T. Vaughan and J. Griffiths, John Wiley and Sons, Ltd: Hoboken, NJ, 2012, Chap. 4. Double-Tuned Surface Coils.
26. M. Bendall, *Magn. Reson. Med.*, 1988, **8**, 380.
27. D. K. Sodickson, M. A. Ohliger, R. Lattanzi, and G. C. Wiggins, in RF Coils for MRI, eds J. T. Vaughan and J. Griffiths, John Wiley and Sons, Ltd: Hoboken, NJ, 2012, Chap. 8. Coil Array Design for Parallel Imaging; Theory and Applications.
28. M. A. Griswold, in RF Coils for MRI, eds J. T. Vaughan and J. Griffiths, John Wiley and Sons, Ltd: Hoboken,

NJ, 2012, Chap. 10. Characterization of Multichannel Coil Arrays on the Benchtop.

29. R. Duensing, in RF Coils for MRI, eds J. T. Vaughan and J. Griffiths, John Wiley and Sons, Ltd: Hoboken, NJ, 2012, Chap. 9. Transceiver Loop Arrays.
30. A. W. Magill and R. Gruetter, in RF Coils for MRI, eds J. T. Vaughan and J. Griffiths, John Wiley and Sons, Ltd: Hoboken, NJ, 2012, Chap. 5. Nested Surface Coils for Multinuclear NMR.
31. C. M. Collins and A. G. Webb, in RF Coils for MRI, eds J. T. Vaughan and J. Griffiths, John Wiley and Sons, Ltd: Hoboken, NJ, 2012, Chap. 3. Quadrature Surface Coils.
32. C. N. Chen, D. I. Hoult, and V. J. Sank, *J. Magn. Reson.*, 1983, **54**, 324.
33. D. I. Hoult, C. N. Chen, and V. J. Sank, *Magn. Reson. Med.*, 1984, **1**, 171.
34. V. J. Sank, C. N. Chen, and D. I. Hoult, *J. Magn. Reson.*, 1986, **69**, 236.
35. J. Murphy-Boesch, in RF Coils for MRI, eds J. T. Vaughan and J. Griffiths, John Wiley and Sons, Ltd: Hoboken, NJ, 2012, Chap. 12. Double-Tuned Bird Cage Coils: Construction and Tuning.
36. F. D. Doty and G. Entzminger, in RF Coils for MRI, eds J. T. Vaughan and J. Griffiths, John Wiley and Sons, Ltd: Hoboken, NJ, 2012, Chap. 21. Litz Coils for High Resolution and Animal Probes, Especially for Double Resonance.
37. E. W. H. Wong, in RF Coils for MRI, eds J. T. Vaughan and J. Griffiths, John Wiley and Sons, Ltd: Hoboken, NJ, 2012, Chap. 22. Millipede Coils.
38. N. De Zanche, in RF Coils for MRI, eds J. T. Vaughan and J. Griffiths, John Wiley and Sons, Ltd: Hoboken, NJ, 2012, Chap. 11. Birdcage Volume Coil Design.
39. J. T. Vaughan, in RF Coils for MRI, eds J. T. Vaughan and J. Griffiths, John Wiley and Sons, Ltd: Hoboken, NJ, 2012, Chap. 13. TEM Body Coils.
40. G. Adriany, in RF Coils for MRI, eds J. T. Vaughan and J. Griffiths, John Wiley and Sons, Ltd: Hoboken, NJ, 2012, Chap. 15. TEM Transceiver Head Coils for Ultra High Magnetic Fields.
41. G. Adriany, P. F. Van de Moortele, F. Wiesinger, S. Moeller, J. P. Strupp, P. Andersen, C. Snyder, X. Zhang, W. Chen, K. P. Pruessmann, P. Boesiger, T. Vaughan, and K. Ugurbil, *Magn. Reson. Med.*, 2005, **53**, 434.
42. N. I. Avdievich, in RF Coils for MRI, eds J. T. Vaughan and J. Griffiths, John Wiley and Sons, Ltd: Hoboken, NJ, 2012, Chap. 6. Quadrature Transverse Electromagnetic (TEM) Surface Coils.
43. N. I. Avdievich, in RF Coils for MRI, eds J. T. Vaughan and J. Griffiths, John Wiley and Sons, Ltd: Hoboken, NJ, 2012, Chap. 16. Transverse Electromagnetic (TEM) Surface Coils for Extremeties.
44. J. T. Vaughan, G. Adriany, C. Snyder, L. Bolinger, H. Liu, J. Tian, and K. Ugurbil, *Magn. Reson. Med.*, 2004, **52**, 851.
45. J. T. Vaughan, Cavity Resonator for NMR System. University of Alabama at Birmingham (Birmingham, AL), assignee. United States patent 5744957, 1998.

Chapter 4
A Practical Guide to In Vivo MRS

Dominick J.O. McIntyre
CRUK Cambridge Institute, Cambridge, UK

4.1 INTRODUCTION

A reader working through this book sequentially will have been introduced to in vivo magnetic resonance spectroscopy (MRS) at an abstract and theoretical level (see Chapters 1 and 2). This chapter sets out to describe the daily experience of the spectroscopist working in a preclinical or clinical MRI unit. While the spectroscopist's interaction with the subject will be quite different for a human patient or volunteer compared with a mouse, the instruments and protocols are very similar, and the choice of sequence depends much more on the nucleus to be measured than the type of subject. Therefore, this chapter sets out a generic experimental procedure from preparation for the arrival of the subject to offline processing of the acquired data, discussing multiple options as they arise.

Handbook of Magnetic Resonance Spectroscopy In Vivo: MRS Theory, Practice and Applications.
Edited by Paul A. Bottomley and John R. Griffiths
 ISBN: 978-1-118-99766-6
Also published in eMagRes (online edition)
DOI: 10.1002/9780470034590.emrstm1489

4.2 THE MAGNETIC RESONANCE UNIT

4.2.1 Entering the Unit

Whatever your subject may be, your first tasks as you arrive at the unit will be safety-related (see the American College of Radiology's White Paper on safety[1]. Two principal hazards are magnetic items that are allowed too close to the magnet such that they become projectiles that injure or kill staff or patients; and implants within the body that interact with the main magnetic field or RF or gradient pulses, potentially causing burns, internal injuries, or even death.[2] The unit will generally be locked at all times. Access will be restricted to staff who are trained in magnet safety (which can be summarized as 'Don't take anything magnetic anywhere near the magnet') and who have no hazardous implants within their bodies – such items may pose as much risk in the bodies of instrument operators as in patients.

Aneurysm clips[3] and cardiac pacemakers are generally the most common and important contraindications: while exposure to strong magnetic fields can be potentially fatal and metal fragments in the eyes can blind,[4] scanning with pacemakers is possible under controlled conditions[5,6] (use of sequences with reduced specific absorption rates [SAR], and certain pacemaker functions disabled). Generally, anything within a patient's body that they were not born with must be assessed for safety and their proximity to the region of interest (ROI) assessed for potential degradation of images and spectra, before the patient may

enter the magnet room. Useful screening forms may be found at the web site of the Institute for Magnetic Resonance Safety, Education, and Research[7]; this site also contains an excellent list of medical implants and their safety implications. Any patient arriving must be screened before scanning. Experimental animals generally present less of a challenge: microchips outside the area of study are usually not a problem for animals larger than mice (where the artifacts may extend across a large part of the body), but other experimental implants may not be MRI-compatible (for instance, long metallic pins for bones and devices for controlled drug infusion).

It is essential to avoid taking magnetic items close to the magnet. Modern self-screened magnets have very small stray fields, but this has the consequence that the field strength increases sharply closer to the magnet, and the resulting force on ferromagnetic objects can accelerate them into the magnet bore at dangerous speeds. You must remove all magnetic items (such as coins, watches, and bank cards with magnetic strips) before entering the stray field of the magnet.

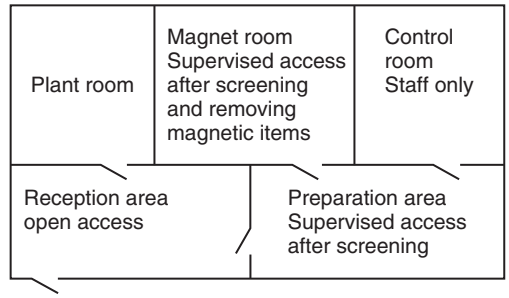

Figure 4.1. Example of a site layout for a clinical MRI unit, showing the stages that a patient must go through before being admitted to the magnet room where the magnetic field is potentially hazardous

Figure 4.2. Clinical MRI magnet. The controls on the front panel allow landmarking of a region of interest (ROI) on the patient and control of the position of the motorized bed. The shelves to the right store RF coils when not in use

4.2.2 Layout of the Unit

Unit design is driven by safety, the need to minimize noise, and institutional space limitations. Noise includes both acoustic noise emitted by the scanner and electrical noise picked up by the scanner's receiver. This last is critical for MRS, as broadband noise will quickly swamp low-amplitude metabolite signals, while coherent noise signals can mimic those of metabolites. A clinical unit will typically consist of an area for patient reception; an area for preparation of screened patients for scanning, including, removal of personal or magnetic items for safe storage; and an imaging area, subdivided into a control room, a magnet room, and a plant room as exemplified in Figure 4.1. The magnet room is a soundproof, electrically shielded, lockable room that fully encloses the magnet and most of its stray field (Figures 4.2 and 4.3).

Most scanners employ a superconducting magnet constructed from a coil of superconducting wire (typically NbTi) enclosed in a cryostat and immersed in a bath of liquid helium to maintain the superconducting temperature. A cryocooler[8] is used to prevent the liquid helium being boiled off by heat leaking into the cryostat: this device is often referred to as a *cold head*. The magnet room will also contain the receiver preamplifier, placed as close to the magnet as is practicable to minimize losses in the signal-to-noise ratio (SNR) in the cable from the RF detection coils, and electronics for connecting and switching the coils to the scanner's receiver. Other electronic components (see Chapter 2) are sited in an adjacent 'plant' room, with connections into the magnet room via a filter panel that minimizes the chance of electrical noise passing through the RF shielding of the magnet room. This separate plant room both limits electronic noise pickup and simplifies maintenance by allowing use of magnetic tools without risk from the magnetic field. Sound levels in the plant room can be sufficiently high to require ear protection, so this room is also generally soundproofed.

Finally, the main computer that runs the MR scanner is located in a control room. Subjects in simple

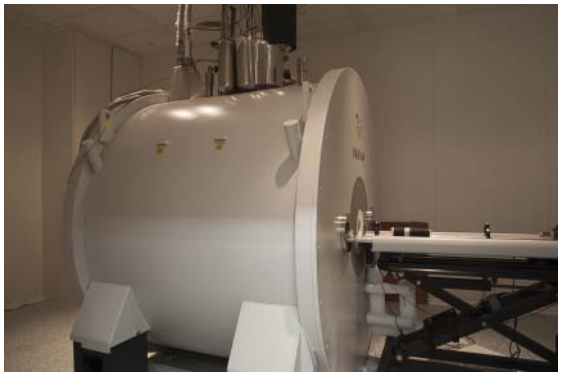

Figure 4.3. Pre-clinical or animal MRI/MRS system. This does not have the cosmetic casing of the clinical instrument or the motorized bed. Part of the cold head system for preventing liquid helium boil-off is visible atop the magnet

preclinical or animal studies can be prepared in the control room as confidentiality is not an issue for animals. However, those animal studies requiring sophisticated instrumentation and/or surgical preparation are best prepared in suitably equipped laboratories that are separated from the scanner facility and then transferred to the scanner area. Aside from such laboratory space, preclinical units generally have fewer enclosed rooms: for example, the equipment associated with smaller-bore systems may not need a dedicated plant room, and the magnet can be fitted with RF-shielded end-caps to provide an RF-shielded compartment instead of a separately shielded magnet room.

4.2.3 System Hardware

Typically, the operator controls the system from a computer running a standard operating system and custom software, which takes over the computer's user interface (UI) completely or which runs one or more windows in a standard UI. This will be connected to the NMR electronics via direct cabling or a dedicated Ethernet interface that allows rapid communications with no interference from other traffic or risk of interception. The operator will also have access to equipment for monitoring the subject's physiology, and in human systems, voice contact with subjects inside the magnet bore, and typically those in the magnet room as well. Thus, only the control computer and physiological monitoring equipment are outside the plant and magnet rooms.

The plant room contains apparatus to generate waveforms for RF and gradient pulses; amplifiers for these pulses; apparatus to digitize the received signal; equipment for making the main magnetic field as uniform as possible over the ROI, a process known as shimming (see Section 4.3.2.2); the compressor for the cold head; and water cooling and air-conditioning systems for the various power supplies. Gradient and RF waveforms are generated on the control computer and transmitted to controllers within the electronics to create the MRI and MRS pulse sequences: the computer determines the exact timing of all of the pulses and the signal reception and the exact amplitudes of all waveforms for each scan. Once started (either manually by the operator or automatically based on a preset schedule), the sequence may continue using preset timings, or individual scans within the sequence may be triggered based on physiological measurements from equipment used to monitor the subject's respiration and/or heart rate, for example.

Separate digital-to-analog converter boards are used to generate control waveforms for the three gradient axes and for one or more RF pulse channels. The gradient waveforms undergo pre-emphasis processing to compensate for inductive delays and eddy current effects and then are fed to the gradient amplifiers. These can produce currents of many hundreds of amperes, which pass through gradient coils and generate the magnetic field gradients that spatially localize the MRI and MRS signals within the magnet bore. Heat generated by these currents often requires both amplifiers and coils to be water cooled. As well as the MRI/MRS gradient coils, which produce linear field gradients, high-field scanners generally include extra coils known as *high-order shims*. These generate nonlinear field gradients in the form of spherical harmonics, but unlike the MRI gradients, they are static. The shim coils can compensate for more complicated field inhomogeneities than linear shims alone, resulting in better MRS line shapes over larger volumes. Linear shims are applied using small constant currents through the gradient coils.

Frequency synthesizers or crystal oscillators are used to generate continuous RF of constant amplitude and highly stable frequency and phase. This signal is amplitude-phase- and/or frequency modulated by the RF pulse envelope to generate the RF pulse, which is then fed to the RF power amplifier to obtain the high-peak power (e.g., up to 16 kW) that is required to achieve large flip angles in a few milliseconds. The RF power amplifier output is gated off when RF

pulses are not being applied, to prevent amplifier noise from contaminating the detected signal. Scanners used for proton (^{1}H) MRI and MRS only may have a single power amplifier tuned for maximum output at the ^{1}H frequency or several identical amplifiers if the scanner has multichannel parallel excitation capabilities. Scanners equipped for nonproton MRS will generally have two power amplifiers, one for ^{1}H and a broadband amplifier for other nuclei, with separate RF channels to control each. These may allow pulses at both ^{1}H and another nucleus to be played out simultaneously, enabling decoupling and nuclear Overhauser enhancement (NOE) sequences.

The gradient cables are connected directly (or via low-pass filtering to eliminate RF noise) to the gradient coils. A single RF coil may serve for both transmission and reception, and the RF interconnections are more complicated to take account of that. For transmit/receive (T/R) coils, the same cabling must carry high-power RF pulses (on the order of 1–16 kW peak) to the coil, and the much weaker (<1 mW) excited NMR signal back to the system preamplifier. Internal switching (the T/R switch) protects the preamplifier from the high-power pulse and prevents noise from the amplifier contaminating the signal. The signal must be detected as soon as possible, and detection in <0.5 ms is often possible in practice, in simple pulse acquire and chemical shift imaging (CSI) sequences. The preamplifier is positioned as close to the magnet as possible to minimize signal attenuation in the cable. The preamplifier output returns to the receiver system within the plant room, usually via further amplification stages, where it is converted into a lower intermediate frequency by mixing with a carrier signal derived from the frequency synthesizer, and then digitized.

4.2.4 RF Coils

RF coils may be transmit-only, receive-only, or fulfill both purposes. They may be volume coils, enclosing the whole body, the head (Figure 4.4), or a limb, or surface coils placed over a tissue ROI. Smaller coils provide higher SNR per unit volume at the expense of depth of penetration, field-of-view, and homogeneity of the transmit field and detector sensitivity.

Typically, when separate coils are used for transmission and reception, both coils will employ PIN (*p*-type intrinsic *n*-type) diode switching to shift their frequency off-resonance when not in use. This reduces cross-talk between the two coils which would otherwise cause 'hot spots' and signal dropouts in image intensity.

Figure 4.4. Head coil for ^{1}H MRI and MRS at 1.5 T

Linear coils will be connected to the transmitter and/or preamplifier with a single cable. Quadrature coils[9,10] (whose circular polarization provides a $\sqrt{2}$ improvement in SNR with half the transmitter power requirement, see Chapter 1) have two ports connected via a quadrature hybrid, which splits the transmitted power into in-phase and 90° phase-shifted excitation signals for the two channels during excitation and recombines the two incoming phase-shifted signals into a single channel for the preamplifier during reception. Parallel transmission systems employ two or more channels powered separately and can accommodate independent variations in phase, amplitude, and even the pulse shape for each channel, to compensate for nonuniformities in the excitation field (B_1). Parallel or phased-array receiver coils, similarly require a separate preamplifier for each channel, and the received signals are separately digitized and combined in software. On clinical systems, this is typically handled via a single multiway connector, but preclinical systems often require individual BNC (Bayonet Neill–Concelman) cable connections for each channel. Finally, ^{1}H and nonproton coils are typically connected to separate channels to allow decoupling, switching coils, and switching the MRS nucleus from the scanner without changing connections. Most coils are designed to operate at a single frequency, but dual-tuned coils may be constructed which simplify ^{1}H MRI and shimming before a nonproton MRS study.

It is common to require at least two probes for an MRS examination, particularly for one involving nonproton MRS. Clinical scanners generally have a

whole-body transmitter coil built into the magnet inner bore and use receive-only coils appropriate for the body part under study.

4.3 THE SCANNING PROCEDURE

4.3.1 Preparing the Subject for Scanning

Importantly, no human MRI/MRS research study can be performed in Europe or North America without an institutionally approved human study protocol, which will detail the purpose of the study, its potential hazards, subject inclusion and exclusion criteria, how informed consent will be obtained and by whom, who will perform the study, what will be done with the data, and how incidental findings will be handled. The system operator and key investigators must be familiar with these, *before* the first volunteer is scanned. The use of animals for research MRI/MRS studies will generally also require approval from an institutional animal care and use committee, which details the protocols that will be performed before, during, and after the scanning, the number and types of animals studied, and their fate. United Kingdom and Australia legislation requires licensing for the institution, each individual project, and for the personnel involved, aimed at optimizing animal welfare and minimizing the numbers used.

In either preclinical or clinical settings, the subject is admitted to the MR scanning area, prepared for the scan, and placed within the magnet with the MRI/MRS coils, and monitoring and gating that are appropriate for the study. The spectroscopist will create a new scan on the computer, enter the subject's details, and set up the sequences to be run and the coils to be used. The sequences can be loaded individually, but it is preferable to load a protocol containing all of the sequences to be used, with the correct parameters (such as number of slices, slice thickness, and echo time) already set.

In a clinical setting, the incoming subject must be consented and a checklist gone through for any exclusions. He or she will be asked to change into a gown and to remove any magnetic items and place them in a locker. The patient is then brought into the magnet room, given earplugs to protect them from acoustic noise generated by the gradient pulses, placed on the patient bed in front of the magnet, and positioned in the MRI/MRS coils. A lighting and position control system located on the magnet front panel is used to set a 'landmark' at the location of the tissue ROI in the subject, which is adjusted by moving a motorized cradle within the patient bed. The subject should be given an alarm button that can be used to attract the operator's attention during the scan: the bore contains an intercom system so that the operator and subject can converse between or during scans. If respiratory and/or cardiac gating are being used, the relevant sensors are attached and the signals checked for proper detection. Finally, the motorized cradle is advanced to insert the subject into the magnet, moving the land-marked ROI to the magnet isocenter where the field homogeneity is highest.

The above-mentioned setting assumes that clinical subjects will be awake. This is generally true, although nervous or claustrophobic patients will occasionally need mild sedation, and pediatric subjects may be sedated. Conversely, the vast majority of animal subjects will be anaesthetized before the scan. Lines for administration of any agents required during the scan will be inserted before magnet entry. Monitors for temperature, respiration, and heart rate may be connected: even if measurement of respiration is not required for gating, respiration and temperature are important for maintaining anesthesia (see Chapters 14 and 15 for preclinical studies and Chapter 16 for clinical studies).

Animals will typically be placed within a handling tray, the coils positioned, the desired scan area landmarked, and the whole inserted into the magnet. If a volume coil is to be used, this will usually be locked in position in the magnet before the animal is inserted. Great care must be taken with positioning to ensure that the ROI is at the center of the magnet and the gradient coils for optimal field homogeneity and registering the target area to the coordinate frame of the localizing gradients. Unlike clinical systems, preclinical/animal systems do not normally have motorized positioning systems and repositioning can take some time.

Some coils now need to be adjusted by tuning to the exact NMR frequency and matching the impedance to the input impedance of the preamplifier, which is usually set at the characteristic impedance of the connecting cable (e.g., 50 Ω), yielding the lowest noise figure.[10] In a properly matched system, all of the power from the transmitter enters the coil, and none is reflected back to the transmitter. This minimizes the RF power required. Similarly, all of the signal is ideally received by the preamplifier, and none is reflected, which maximizes the SNR of the final spectrum. This process involves adjusting capacitors, guided by a reflection display built into the system, a portable nonmagnetic

sweep generator that will show a plot of reflection in decibels as a function of frequency, an RF impedance meter, or a network analyzer. Tuning and matching with a sweep generator typically involves minimizing the reflected power on a 'scope display' and centering it at the MRS frequency. Clinical systems frequently use coils that do not require manual tuning and matching because their resonance frequency does not change significantly with patient load, and the preamplifier noise figure does not vary much over the range of loads usually encountered (e.g., 25–75 Ω).

4.3.2 Scanning Setup

The subject is now fully prepared for scanning, but a number of prescans are carried out before the actual scanning process begins. These include calibrating the RF power required, shimming the magnetic field to optimize homogeneity, and setting the transmitter and receiver offset frequencies. In some cases, particularly on clinical systems, these processes may be so automated that the operator will not be aware of what is happening. Alternatively, they may need to be directed to run, or it may be necessary to override automatic settings where the algorithm has not reached an acceptable state or if a different set of operating parameters are needed for a study. In addition, the operator may choose between a range of automated methods. It is therefore important for the operator to understand what is being adjusted during the prescan phase in the context of the desired experimental or clinical study objectives, even if the only possible intervention is to rerun the same process in the hope that it will work better a second time.

4.3.2.1 RF Power Calibration and B_1 Shimming

Some of these processes will be repeated for different scans. Conversely, for nonproton spectroscopy using surface T/R coils, power calibration may not be done routinely at all. Adiabatic RF pulses whose flip angle is constant over a wide range of RF power are often used to compensate for the highly inhomogeneous RF field strength produced by one of these coils (see Chapter 5). Thus, a single calibration using a highly concentrated phantom solution with the coil loaded similarly to how a subject would load it, may suffice for all future experiments employing the same study protocol. Drift in the power calibration or degradation in the coil performance should in this case be assessed by routine quality assessment (QA) scans (see the following discussion).

A problem with calibration – particularly for nonproton nuclei – is that little or no signal may be visible in a single scan. In an extreme example, a time-course study of the metabolism of fluorinated drugs will yield no signal before the fluorinated agent is injected, as there is no endogenous MRS-visible fluorine in the body. Similarly, for hyperpolarized ^{13}C studies, the endogenous signal from the ROI will be far smaller than that available after substrate injection. Any calibration performed after injection must be very rapid to avoid loss of information about the initial kinetics of the injected substrate and avoid loss of hyperpolarization in those studies (see Chapter 34). In such cases, it is possible to use a small, highly concentrated phantom fitted to the coil for calibration, provided that the phantom MRS signal does not overlap the resonances that are being studied experimentally. Otherwise, the experimenter's only option is to rely on prior phantom calibration, which may be a confounding factor if there are large variations in coil loading among different subjects and/or the calibration phantom.

In the absence of such issues, calibration can be carried out quickly by playing out a series of pulses with increasing amplitudes. The excitation pulses used may be nonselective, slice selective, or employ a three-dimensional (3D) localization sequence such as point resolved spectroscopy (PRESS) to optimize the flip angle over a small ROI even when the RF homogeneity of the coil is nonuniform. For conventional RF pulses applied with a volume transmit coil, the acquired data will show a simple sinusoidal relationship between RF amplitude and signal, allowing an easy, even automatic, calibration. Adiabatic excitation pulses generate signal that increases to a plateau. Inversion pulses can be calibrated by playing out the inversion pulse at increasing amplitudes until a signal null is obtained.

When the experimenter is using a single linear coil, or a quadrature coil driven by a single channel via a quadrature hybrid, this is all that is required for RF power calibration. However, some systems now support the use of multiple independent transmit channels, which require independent calibration.[11] While it is possible to construct volume coils such as birdcage[12] or millipede designs that have highly uniform RF fields when empty, when a quasi-conducting sample is placed in the transmit coil the RF may no longer be uniform. This nonuniformity typically manifests as

'hot spots' or signal dropouts in the images, which can also result in excessive local power deposition (SAR) in some regions of the sample. These problems increase with the sample size and the operating frequency, as the RF wavelength in tissue decreases below the sample dimensions and anatomical structures within the sample. Thus, they are potentially much more severe for a clinical whole-body ^{1}H coil at 7 T where the RF wavelength in tissue is approximately 12 cm than for a head coil at 3 T or the body at 1.5 T. Driving the two ports of a birdcage with the same pulse profile, but different phases, amplitudes, and start time can improve the uniformity of excitation, reduce SAR hot spots, and the overall RF power required. The process of optimizing these parameters is termed B_1 *shimming.*[11] Transverse electromagnetic (TEM) coils work well at higher frequencies than birdcage coils and can be constructed with independent channels (up to 16 at present), to provide improved homogeneity over other options. It is also possible to apply different RF pulse shapes to each channel, a process known as *transmit sensitivity encoding (SENSE)* or *parallel transmit*, thereby providing rapid excitation and localization to an ROI.

4.3.2.2 Shimming

When the subject is inserted into the magnet, susceptibility differences between the tissue and the surrounding air and within the tissue will distort the main magnetic field B_0, as dictated by Maxwell's equations. This effect is particularly important for MRS, as, if left uncompensated, inhomogeneity of <1 ppm in B_0 can distort and broaden line shapes and even cause neighboring spectral peaks to overlap. Shimming is the process of optimizing the currents in the high-order shim coils (see Section 4.3.3) to compensate for these susceptibility distortions as much as is possible (see Chapter 2). Susceptibility effects scale with B_0, so higher-field systems tend to be equipped with more shim coils for providing ever higher-order corrections.

Not all tissues are shimmable to the same homogeneity: the finest line widths are available in parts of the brain remote from bone structures or air spaces, while the frontal and temporal lobes are harder to shim. In tissues like liver, that contain large amounts of paramagnetic deoxygenated blood, microscale susceptibility variations mean that very narrow lines are not attainable. Automated shimming methods include FASTMAP,[13] which analyses the phases of a series of projections through the voxel to provide an accurate shim in a few minutes; and phase-map based methods that employ gradient-echo imaging sequences to map the field offset over a slice or volume, then compute a least-squares fit of the known field profiles of the shims to the field map. It is also possible to shim, manually or automatically, on the integral of the signal recorded from either unlocalized or localized volumes. Shimming is generally carried out on the large ^{1}H water signal, even for nonproton studies.

4.3.2.3 Frequency Calibration

The shimming process will usually shift the mean field strength over the ROI slightly, and the operating frequency of the system must therefore be reset to match this. As volume selection for spectroscopy uses field gradients and frequency-selective pulses, calibration errors displace the voxel from the desired ROI (see Chapter 7). For ^{1}H MRS, water suppression using frequency-selective pulses will be degraded by incorrect calibration. As with RF power calibration, frequency calibration is challenging when little or no endogenous signal is available. In this case, a frequency reference phantom may be used, or the required offset estimated from previous phantom studies and the experimentally observed ^{1}H water offset.

4.3.3 Scout Imaging

Often, spectroscopy will be performed as part of a clinical or research study in which MRS data are acquired along with MRI using multiple contrast mechanisms. While the various MRI methods fall beyond the scope of this book, we note that the MRS will at minimum require an initial set of three-plane MRI scans for localizing, followed by high-resolution MRI covering the MRS ROI, and ideally, MRI in at least two perpendicular orientations to allow accurate 3D localization of the ROI.

4.3.4 MRS Setup and Acquisition

The spectroscopist must now choose the MRS localization method to be used. The first question is whether to use a single voxel or a multivoxel method. The simplest method of localization is to use nonselective pulses with a surface coil placed over the

tissue of interest, which limits the signal acquired to the field of view of the coil. Generally, though, more sophisticated sequences are needed to eliminate signal outside the ROI but within the coil's sensitive volume. The principal localization sequences are PRESS,[14] stimulated echo acquisition mode (STEAM),[15] localization by adiabatic selective refocusing (LASER),[16] and image-selected in vivo spectroscopy (ISIS)[17] (see Chapter 7 for more detail). The first three of these use double (PRESS and STEAM) or triple (LASER) spin-echoes, with slice-selective gradients applied along three orthogonal directions for each of the excitation, and refocusing pulses to acquire the signal from a volume defined by the intersection of the slices. These three sequences can in principle provide a spectrum from a single scan, although in practice multiple averages are required to improve SNR. They differ in the refocusing pulses: PRESS uses 180° pulses to provide spin-echoes. STEAM employs 90° pulses that reduce power deposition and allow for sharper slice definition and shorter echo times than PRESS, albeit at the expense of halving the SNR. With modern gradient performance allowing shorter PRESS echo times, STEAM is now used less often. LASER employs a train of adiabatic refocusing pulses: these give excellent volume definition even in the presence of the inhomogeneous B_1 provided by surface coil excitation and reduce the effects of J-coupling. However, the power deposition is higher than for PRESS and STEAM.

ISIS uses three slice-selective inversion pulses with the slice-selective gradients applied along three orthogonal directions, followed by a nonselective excitation pulse. This is repeated in an eight-step cycle with different combinations of the inversion pulses being omitted, and the signals are then combined by addition and subtraction so that all the signal from outside the ROI that lies at the intersection of the three inverted slices, cancels. This method is useful for species with short spin–spin (T_2) relaxation times, as the signal is entirely along the B_0 or $\pm Z$-axis during the preparation phase and undergoes only spin–lattice relaxation (T_1) decay. However, motion and partial saturation effects during the eight-scan cycle can result in incomplete cancellation and substantial contributions from outside the ROI to the final spectrum. Phosphorus (^{31}P) MRS is the principal application for ISIS: this is used mainly for pH measurements (see Chapter 25), studying tissue energetics (see Chapters 42, 51, and 55), and tumor studies.

The choice of localization sequence is largely determined by the relative sensitivity, the T_2 and/or spin–spin (J-)coupling of the resonances of interest, and how many ROIs need to be studied: for some nuclei (e.g., ^{31}P), key metabolites (such as ATP) have relatively short T_2 values and dephasing due to J-coupling, while ^{1}H metabolites have a range of T_2s of a few milliseconds up to hundreds of milliseconds, depending on the molecular properties. Metabolites with short T_2 values require sequences with a very short delay between excitation and acquisition of signal, such as ISIS. Metabolites with longer T_2 values can tolerate longer delays, and indeed, it is possible to use spin-echo sequences with the echo time optimized for a particular J-coupled resonance of interest. The ^{1}H signal from tissue typically includes large, broad resonances of very short T_2 which are often of little clinical interest: using longer echo times can be advantageous in reducing these signals, resulting in the remaining resonances sitting on a flatter baseline, which makes quantification easier.

^{1}H-visible tissue components include water and lipid at concentrations much higher than most metabolites of interest. Water is visible at some level in all tissues at all echo time values, and its signal must therefore be suppressed to allow accurate quantification of other metabolites. This is generally done by applying one or more narrow band RF pulses centered on the water frequency followed by crusher gradients to ensure that the longitudinal water magnetization is minimal immediately before the localization sequence starts. However, it is also common practice to acquire an unsuppressed water scan that can be used to compensate eddy current effects on the spectral line shapes and/or for use as a concentration reference for metabolites acquired from the same ROIs.

Lipids have relatively short T_2 values and are often not detectable at longer echo times of 144 ms and above. In normal brain, little lipid signal is visible even at short echo times as it is mainly membrane-bound and has very short T_2. However, in pathology such as tumors, there is often an intense lipid signal associated with necrosis that can mask metabolites including lactate, which is an important marker for hypoxia.

Phase-encoding gradients may be inserted into all of the above-mentioned sequences to obtain data in parallel from multiple voxels; this is known as *spectroscopic imaging* or CSI (see Chapter 8). One-, two-, or three-dimensional schemes may be used. For a given sequence repetition time and overall acquisition

time, the SNR per unit volume is the same for CSI as it is for single voxel MRS. Typically, acquisitions of this type will last upward of a few minutes, depending on the desired SNR and, for CSI, the dimensions of the CSI data set. For hyperpolarized studies, such long acquisition times are unacceptable, and these will use accelerated or single-shot spectroscopic imaging sequences if multivoxel data are required (see Chapter 34); such sequences are also applicable to ^{1}H MRS studies (see Chapter 12).

4.4 POST-SCAN PROCEDURES

Once all scans have been acquired, the subject may be removed from the magnet. If the subject is a patient, you should not discuss the scans with him or her; this is the responsibility of the clinician handling the case. If the subject is a research volunteer, and the scan reveals previously unknown pathology, you should follow your unit's procedures for incidental findings. The system operator and key investigators must be familiar with these (as well as the MRI/MRS protocol), *before* the first volunteer is scanned.

The acquired data should be backed up daily: in a clinical environment, it will probably be transferred to the local picture archiving and communications system (PACS). While these systems are excellent for image analysis, spectroscopy analysis is usually carried out in a specialized package run on an offline workstation, and the acquired data should be transferred without delay to that workstation. A number of specialized MRS fitting packages are available, which typically model spectra either by parameterized prior knowledge or using spectra of individual metabolite solutions acquired under the same experimental conditions as a basis set for fitting. LCModel is one package that uses a metabolite solution basis set (see Chapters 18 and 20). Java-based magnetic resonance user interface (jMRUI) and its predecessor MRUI, and TARQUIN fit MRS data in the time domain, without previously applying a Fourier transform (see Chapters 19 and 20).

Ideally, a daily QA scan should be performed on scanners used regularly for MRS. This involves performing a setup procedure and running a scan on a standard phantom to ensure that the RF power, SNR, and shim remain consistent from day to day: variations therefrom may allow early detection of hardware failures and pre-emptive repairs before a subject enters the scanner.

Finally, this chapter closes as it opened, with safety: lock up the unit before you leave!

RELATED ARTICLES IN EMAGRES

Cryogenic Magnets for Whole-Body Magnetic Resonance Systems

Proton Decoupling During In Vivo Whole Body Phosphorus MRS

Proton Decoupling in Whole Body Carbon-13 MRS

Radiofrequency Systems and Coils for MRI and MRS

Spatial Encoding Using Multiple rf Coils: SMASH Imaging and Parallel MRI

Sodickson, Daniel K.: The Many Guises of Tomography – A Personal History of Parallel Imaging

Coil Array Design for Parallel Imaging: Theory and Applications

Double-Tuned Surface Coils

Double-Tuned Birdcage Coils: Construction and Tuning

Birdcage Resonators: Highly Homogeneous Radiofrequency Coils for Magnetic Resonance

Birdcage Volume Coil Design

Millipede Coils

TEM Body Coils

Safety Considerations in MRI

Safety and Sensory Aspects of Main and Gradient Fields in MRI

Safety Regulation in MR

Bioeffects and Safety of Radiofrequency Electromagnetic Fields

Health and Safety Aspects of Human MR Studies

RF Device Safety and Compatibility

Radiofrequency Fields: Interactions, Biological Effects, and Safety Issues

Receiver Design for MR

Whole Body Magnetic Resonance Spectrometers: All-Digital Transmit/Receive Systems

REFERENCES

1. E. Kanal, A. J. Barkovich, C. Bell, J. P. Borgstede, W. G. Bradley, J. W. Froelich, J. R. Gimbel, J. W. Gosbee, E. Kuhni-Kaminski, P. A. Larson, J. W. Lester, J. Nyenhuis, D. J. Schaefer, E. A. Sebek, J. Weinreb, B. L. Wilkoff, T. O. Woods, L. Lucey, and D. Hernandez, *J. Magn. Reson. Imaging*, 2013, **37**, 501.
2. J. F. Schenck, *J. Magn. Reson. Imaging*, 2000, **12**, 2.
3. R. P. Klucznik, D. A. Carrier, R. Pyka, and R. W. Haid, *Radiology*, 1993, **187**, 855.
4. W. M. Kelly, P. G. Paglen, J. A. Pearson, A. G. San Diego, and M. A. Soloman, *Am. J. Neuroradiol.*, 1986, **7**, 243.
5. S. Nazarian, A. Roguin, M. M. Zviman, A. C. Lardo, T. L. Dickfeld, H. Calkins, R. G. Weiss, R. D. Berger, D. A. Bluemke, and H. R. Halperin, *Circulation*, 2006, **114**, 1277.
6. S. Nazarian, R. Hansford, A. Roguin, D. Goldsher, M. M. Zviman, A. C. Lardo, B. S. Caffo, K. D. Frick, M. A. Kraut, I. R. Kamel, H. Calkins, R. D. Berger, D. A. Bluemke, and H. R. Halperin, *Ann. Intern. Med.*, 2011, **155**, 415.
7. mrisafety.com. The official site of the Institute for Magnetic Resonance Safety, Education, and Research, 2015. http://www.mrisafety.com (accessed May 26, 2015).
8. R. Radebaugh, *J. Phys. Condens. Matter*, 2009, **21**, 164219.
9. D. I. Hoult, C.-N. Chen, and V. J. Sank, *Magn. Reson. Med.*, 1984, **1**, 339.
10. D. W. McRobbie, E. A. Moore, M. J. Graves, and M. R. Prince, in MRI from Picture To Proton, 2nd edn, Cambridge University Press: Cambridge, 2007, Chap. Radiofrequency system, 175.
11. W. M. Brink, V. Gulani, and A. G. Webb, *J. Magn. Reson. Imaging*, 2015, **42**, 855.
12. C. E. Hayes, W. A. Edelstein, J. F. Schenck, O. M. Mueller, and M. Eash, *J. Magn. Reson.*, 1985, **63**, 622.
13. R. Gruetter, *Magn. Reson. Med.*, 1993, **29**, 804.
14. P. A. Bottomley, *Ann. N. Y. Acad. Sci.*, 1987, **508**, 333.
15. J. Frahm, K.-D. Merboldt, and W. Hänicke, *J. Magn. Reson.*, 1987, **72**, 502.
16. M. Garwood and L. DelaBarre, *J. Magn. Reson.*, 2001, **153**, 155.
17. R. J. Ordidge, A. Connelly, and J. A. B. Lohman, *J. Magn. Reson.*, 1986, **66**, 283.

Localization

Chapter 5
Adiabatic Excitation Pulses for MRS

Robin A. de Graaf
MRRC, Yale University, New Haven, CT, USA

5.1 INTRODUCTION

Radio frequency pulses are at the heart of every magnetic resonance (MR) experiment. They are the principle tools to achieve spin manipulations like excitation, inversion, and refocusing. The range of RF pulse types is enormous and can include RF amplitude, frequency, and gradient modulations. The majority of MR experiments are performed with conventional, amplitude-modulated RF pulses, which include hard (i.e., square or unmodulated), Gaussian, sinc, and optimized Shinnar-Le Roux (SLR)[1] pulses. When used in combination with volume resonators that are characterized by a relatively homogeneous RF transmit field, amplitude-modulated RF pulses provide excellent results. However, the nutation angle of amplitude-modulated RF pulses is linearly dependent on the RF transmit field strength, B_1. As such, their performance strongly degrades when used in combination with surface coils that allow more sensitive signal detection, and are also characterized by an inhomogeneous RF transmit field. The spatially varying nutation angle can lead to signal loss, undesired image contrast and artifacts.

This short overview is focused on adiabatic RF pulses that have simultaneous amplitude and frequency modulation. This seemingly minor modification has major consequences on pulse performance. Adiabatic RF pulses have an extreme tolerance to variations in RF amplitude. In addition, adiabatic RF pulses have been shown to provide superior off-resonance performance. Taken together, adiabatic RF pulses can provide a convenient, user-friendly option to ensure maximum performance in a wide range of experiments. While there is still continuing development of adiabatic RF pulses, it should be realized that their concept has been utilized since the very first NMR experiments by Bloch[2] and Purcell *et al.*[3] who used adiabatic full (or fast) passage (AFP) for magnetization inversion.

The theoretical principles of adiabatic RF pulses have been reviewed in detail.[4–6] Here, we focus on their practical implementation, calibration, and applications. Following a brief section on the theoretical foundations of adiabatic RF pulses, emphasis is given to the choice of modulation functions and their effect on off-resonance performance. The utility of adiabatic RF pulses is demonstrated by three in vivo MR spectroscopy (MRS) applications.

Handbook of Magnetic Resonance Spectroscopy In Vivo: MRS Theory, Practice and Applications.
Edited by Paul A. Bottomley and John R. Griffiths
 ISBN: 978-1-118-99766-6
Also published in eMagRes (online edition)
DOI: 10.1002/9780470034590.emrstm1443

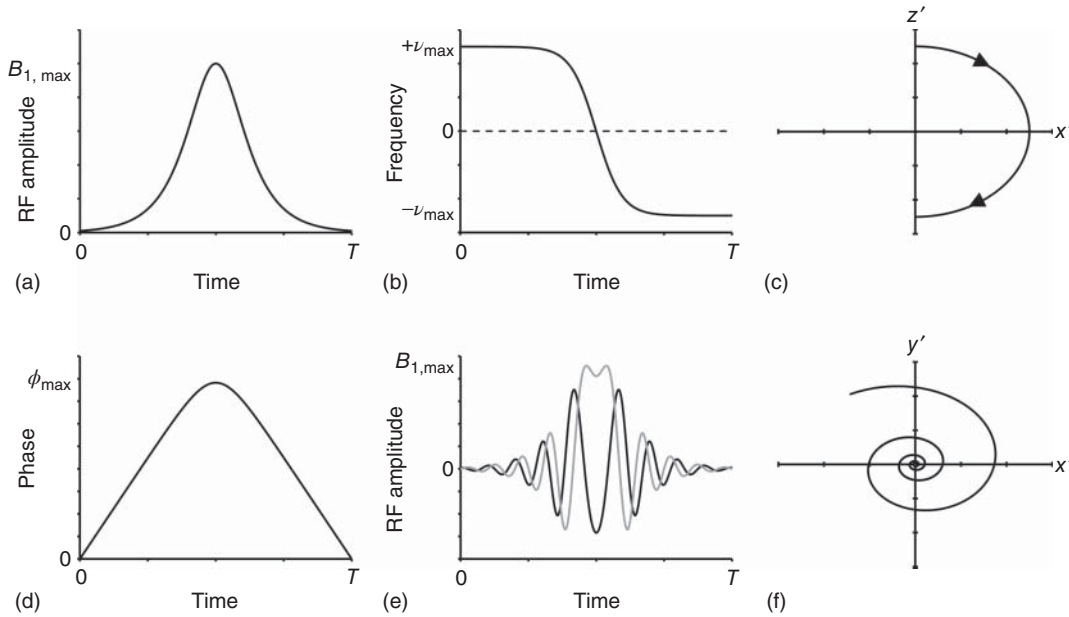

Figure 5.1. (a) Amplitude and (b) frequency modulation functions for a hyperbolic secant (HS1) adiabatic RF pulse. (c) Rotation of the effective field in a frequency-modulated (FM) frame in which the orientation of $B_1(t)$ is constant along x'. (d) Phase modulation function as calculated from (b) using equation (5.5). (e) Real (black, B_{1x}) and imaginary (gray, B_{1y}) components of $B_1(t)$. (f) Rotation of the B_1 field in a constant-frequency, phase-modulated (PM) frame

5.2 THEORY

5.2.1 Modulation Functions

The amplitude $B_1(t)$ and frequency $\Delta\nu(t)$ modulations of adiabatic RF pulses can be described in a constant phase, frequency-modulated (FM) reference frame as

$$B_1(t) = B_{1,\max} f_B(t) \tag{5.1}$$

$$\nu(t) - \nu_c = \Delta\nu(t) = \nu_{\max} f_\nu(t) \tag{5.2}$$

where $B_{1,\max}$ and $\nu_{\max}$ are the maximum RF amplitude and maximum frequency offset (in Hz), respectively, and ν_c the RF carrier frequency (in Hz). Note that some previous publications use angular frequency $\Delta\omega(t) = 2\pi\Delta\nu(t)$, instead. For convenience, both $B_1(t)$ and $\Delta\nu(t)$ are expressed in units of Hz. The Larmor equation can be used to convert units from Tesla and Hertz, for example, B_1 (in T) $= (2\pi/\gamma)B_1$ (in Hz), where γ is the gyromagnetic ratio (in rad T^{-1} s^{-1}). One of the most common adiabatic RF pulses is the hyperbolic secant (HS1) pulse[7,8] for which the modulations are given by

$$B_1(t) = B_{1,\max}\,\mathrm{sech}\,(\beta\,(1 - 2t/T)) \tag{5.3}$$

$$\Delta\nu(t) = \nu_{\max}\tanh(\beta(1 - 2t/T)) \tag{5.4}$$

where T is the pulse length and $0 \le t \le T$. β is a dimensionless truncation factor that is typically defined as $\mathrm{sech}(\beta) = 0.01$. Figure 5.1(a) and (b) shows the RF modulations as defined by equations (5.3) and (5.4). Figure 5.1(c) shows the trajectory of the effective field $B_e(t)$, which represents the vector sum of $B_1(t)$ and $\Delta\nu(t)$. It follows that in the FM frame, the orientation of the $B_1(t)$ field remains stationary along the x'-axis, whereas the $B_e(t)$ field rotates from the $+z'$-axis through the $+x'$-axis onto the $-z'$-axis.

On most modern spectrometers, adiabatic RF pulses are implemented as amplitude and *phase*-modulated (PM) RF pulses. The frequency and phase modulations are closely related as phase is the time integral of frequency according to

$$\phi(t) = 2\pi \int_0^t \Delta\nu(t)\mathrm{d}t \tag{5.5}$$

which, for an HS1 pulse evaluates to

$$\phi(t) = \frac{\pi \nu_{\max} T}{\beta} \ln \left[\frac{\operatorname{sech}(\beta(1 - 2t/T))}{\operatorname{sech}(\beta)} \right] \tag{5.6}$$

Figure 5.1(d) shows the HS1 phase modulation given by equation (5.6). The derivation of a closed-form expression for the phase modulation based on other frequency modulation functions $f_\nu(t)$ may not always be possible. In general, a closed-form expression is not required as the phase modulation can be obtained through numerical integration according to equation (5.5). In a constant-frequency PM reference frame, the trajectory of the RF field can be described by two magnetic fields $B_{1x}(t)$ and $B_{1y}(t)$, along the x and y axes, respectively, given by $B_{1x}(t) = B_1(t)\cos\phi(t)$ and $B_{1y}(t) = B_1(t)\sin\phi(t)$ and are shown in Figure 5.1(e). Figure 5.1(f) shows the trajectory of the $B_1(t)$ field in the PM frame. Whereas adiabatic RF pulses are experimentally executed with amplitude and phase modulation, the principles of adiabatic RF pulses and their effect on the magnetization are best understood in the FM frame with amplitude and frequency modulation.

5.2.2 Adiabatic Condition

So far, only the magnetic fields associated with the adiabatic RF pulses have been considered. However, the ultimate purpose of AFP pulses is to invert the longitudinal magnetization. Figure 5.2 shows the modulation of the magnetization during an HS1 AFP pulse in the FM frame $x'y'z'$. At the onset of the pulse, the effective field $B_e(0)$ is equal to the frequency offset $\nu_{\max}$ along the $+z'$-axis. The longitudinal magnetization is parallel to $B_e(0)$. As the pulse is executed according to the modulations shown in Figure 5.1(a) and (b), the frequency offset decreases and the RF field along the x'-axis increases, rotating the effective field $B_e(t)$ away from the $+z'$-axis. As long as the effective field is rotating slowly compared to its amplitude, the longitudinal magnetization will remain parallel to $B_e(t)$ and therefore follows $B_e(t)$. Halfway through the pulse, both $B_e(T/2)$ and the magnetization have been rotated to the x'-axis. If the pulse is terminated at this point in time, it is referred to as an adiabatic half-passage (AHP) pulse and it has achieved excitation. When the AFP pulse is continued, the effective field is rotated toward the $-z'$-axis, ultimately resulting in an inversion of the magnetization.

The primary requirement for the magnetization to remain parallel with $B_e(t)$ is that the effective field rotates slowly. The rate of change of $B_e(t)$ is equal to $d\alpha(t)/dt$, where $\alpha(t)$ is the angle between $B_e(t)$ and the z'-axis (Figure 5.2a). In a rotating frame of reference in which the orientation of $B_e(t)$ is always along z'', the rate of change in $B_e(t)$ can be represented as a vector along the y''-axis (Figure 5.2b). The $B_e(t)$ and $d\alpha(t)/dt$ vectors together make up a total effective field $B_e'(t)$ around which the magnetization is precessing. When the rate of change $d\alpha(t)/dt$ is small compared to $B_e(t)$, the $B_e(t) \sim B_e'(t)$ and the magnetization follows the effective field as described earlier. When $d\alpha(t)/dt$ is relatively large compared to $B_e(t)$, $B_e'(t)$ significantly deviates from $B_e(t)$ leading to erratic rotations of the magnetization around $B_e'(t)$.

A rotation is said to be adiabatic when $B_e(t) \sim B_e'(t)$ throughout the pulse, which can be represented by the inequality:

$$\left|B_e(t)\right| = \sqrt{B_1^2(t) + \Delta\nu^2(t)} \gg \left|\frac{d\alpha(t)}{dt}\right| \tag{5.7}$$

with

$$\alpha(t) = \operatorname{atan}\left(\frac{\Delta\nu(t)}{B_1(t)}\right) \tag{5.8}$$

Equation (5.7) is commonly referred to as the 'adiabatic condition' and has been extensively used in the design and optimization of modulation functions for AFP pulses.[9,10] Using the vector diagrams and equation (5.7), it is now straightforward to understand the high immunity of adiabatic RF pulses to RF inhomogeneity. Figure 5.2(c–e) shows the RF modulation $B_1(t)$, effective field $B_e(t)$, and rate of change $d\alpha(t)/dt$ during an HS1 pulse for various RF amplitudes. For a maximum RF amplitude $B_{1,\max}$ of 1.25 kHz, it is clear from Figure 5.2(c) that $|B_e(t)| \sim |d\alpha(t)/dt|$ for a significant part of the pulse when $t \sim T/2$. As a result, the magnetization rotates around $B_e'(t)$, which significantly deviates from $B_e(t)$, leading to erratic modulations of the magnetization as shown in Figure 5.2(f). In other words, a 4 ms HS1 pulse with a 2.5 kHz maximum frequency modulation does not adequately satisfy the adiabatic condition of equation (5.7) at $B_{1,\max} = 1.25$ kHz thereby leading to an incomplete inversion. The situation for $B_{1,\max} = 2.5$ kHz (Figure 5.2d and g) and 5.0 kHz (Figure 5.2e and h) is significantly different in that the magnetization largely follows the effective field from the $+z$ to the $-z$-axis. Figure 5.2(d) and (e) reveals that $|B_e(t)| \gg |d\alpha(t)/dt|$ throughout the pulse, ensuring complete inversion. From Figure 5.2, it should be clear that an increase in $B_{1,\max}$ leads to

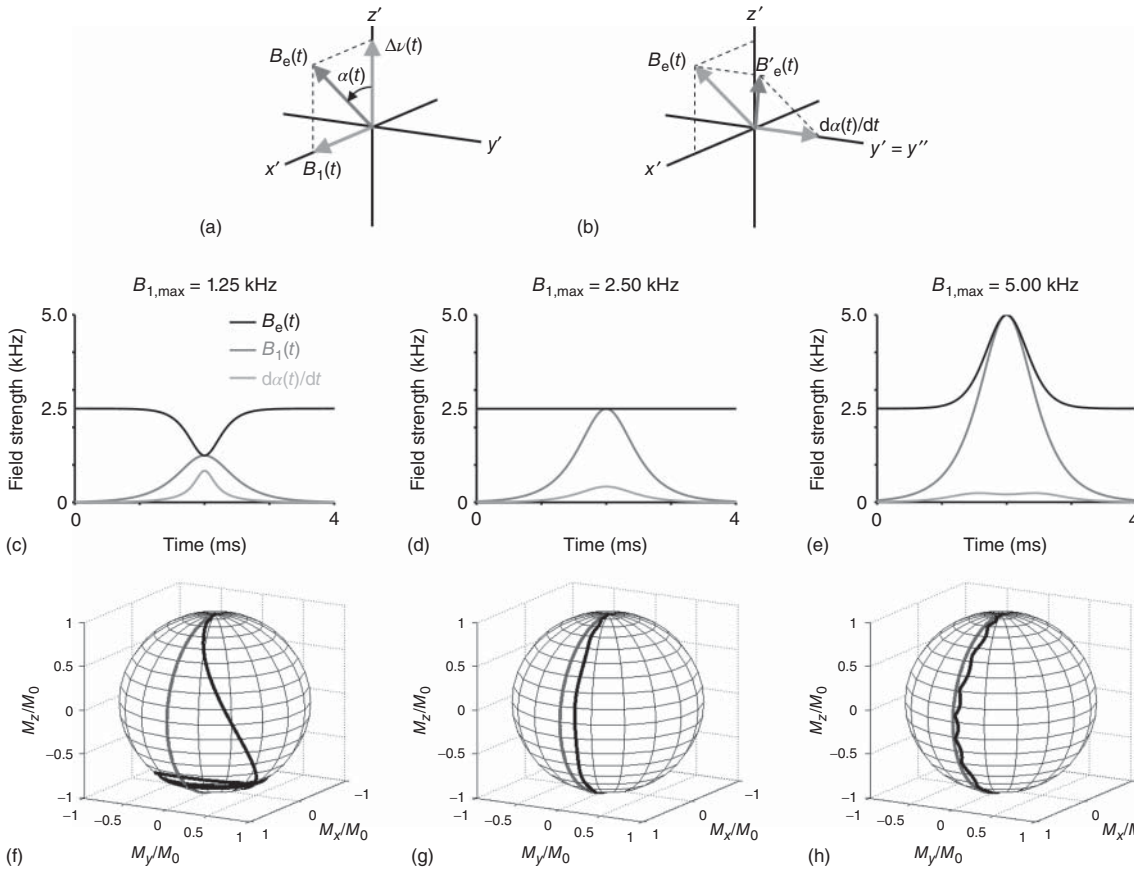

Figure 5.2. (a) Magnetic field components in a FM frame-of-reference $x'y'z'$. (b) Magnetic field components in a secondary frame-of-reference $x''y''z''$, which rotates around the $y' = y''$-axis with frequency $[\mathrm{d}\alpha(t)/\mathrm{d}t]$. $B_e(t)$ starts and remains along the z''-axis (not shown). (c–e) Temporal evolution of $B_e(t)$, $B_1(t)$, and $[\mathrm{d}\alpha(t)/\mathrm{d}t]$ during a 4-ms HS1 pulse ($R = 20$) at maximum RF amplitudes $B_{1,\max}$ of (c) 1.25 kHz, (d) 2.50 kHz, and (e) 5.00 kHz. (f–h) Temporal evolution of the longitudinal magnetization during the same 4.0 ms HS1 ($R = 20$) pulse. At a $B_{1,\max}$ of (f) 1.25 kHz, the adiabatic condition of equation (5.7) is not sufficiently satisfied leading to incomplete inversion. At $B_{1,\max}$ of (g) 2.50 kHz and (h) 5.00 kHz, the adiabatic condition is satisfied throughout the pulse leading to a near-complete inversion

different $B_e(t)$ and $\mathrm{d}\alpha(t)/\mathrm{d}t$ modulation curves, but as long as $|\mathrm{d}\alpha(t)/\mathrm{d}t| \ll |B_e(t)|$ throughout the RF pulse, the magnetization follows the effective field, thereby resulting in inversion.

Using tools identical to those shown in Figure 5.2, that is, vector diagrams and equation (5.7), it is straightforward to show that HS1 AFP pulses only achieve inversion for frequency offsets ν that satisfy $-\nu_{\max} \le \nu \le \nu_{\max}$, that is, the inversion profile is frequency selective. For frequency offsets $\nu > \nu_{\max}$, the effective field $B_e(t)$ rotates away from the $+z'$-axis as $\Delta\nu(t)$ decreases and $B_1(t)$ increases. However, as $\nu(t) - \nu > 0$ throughout the pulse, the effective field never crosses the transverse plane. Instead, $B_e(t)$ rotates back toward the $+z'$-axis. When the adiabatic condition is adequately satisfied, the magnetization follows $B_e(t)$ as it rotates away from and then back to the $+z'$-axis, leading to an effective rotation of 0° at the end of the pulse.

Tannus and Garwood used the adiabatic condition of equation (5.7) to derive a general class of adiabatic modulation functions that satisfy the adiabatic condition equally for all frequencies $|\nu| \le |\nu_{\max}|$. The details of these so-called offset-independent adiabaticity

(OIA) modulation functions can be found in Refs 10, 11. One of the most useful groups of OIA pulses is the HSn family, which can be described by:

$$B_1(t) = B_{1,\max}\mathrm{sech}\left(\beta(1-2t/T)^n\right) \tag{5.9}$$

$$\Delta\nu(t) = \Delta\nu_{\max}\left[1 - 2\left(\int_0^t f_b^2(t)\,\mathrm{d}t \Big/ \int_0^T f_b^2(t)\mathrm{d}t\right)\right] \tag{5.10}$$

where n is an integer. Note that for $n = 1$, the pulse reduces to the HS1 pulse described earlier. Once the adiabatic condition is satisfied, OIA pulses have some common features that include a constant inversion profile for $|\nu| \leq |\nu_{\max}|$ and an identical average B_1 field, $B_{1,\mathrm{rms}}$ for the minimum $B_{1,\max}$, necessary to achieve inversion. The point at which the adiabatic condition is satisfied varies widely among OIA and other AFP pulses.

Figure 5.3 shows the performance of three AFP pulses over a range of B_1 amplitudes and frequency offsets. Figure 5.3(c–e) and (h–j) shows the performance of the OIA pulses HS1 (Figure 5.3a and b) and HS8 (Figure 5.3f and g) with different R values, where $R \equiv 2\Delta\nu_{\max}T$. Figure 5.3(m–o) shows the performance of an optimized AFP pulse (Figure 5.3k and l) that can be described by:

$$B_1(t) = B_{1,\max}\tanh\left(\xi\left(1 - |1 - 2t/T|\right)\right) \tag{5.11}$$

and

$$\Delta\nu(t) = \nu_{\max}\tan\left(\kappa\left(1 - 2t/T\right)\right) / \tan\left(\kappa\right) \tag{5.12}$$

which for $\xi = 10$ and $\kappa = \mathrm{atan}(20)$ closely resembles an AFP pulse with numerically optimized modulation (NOM) functions optimized to give the largest bandwidth at the lowest RF amplitude.[9,12]

From Figure 5.3, it follows that HS1 and HS8 pulses both achieve OIA at $R \geq 40$. The HS8 pulse achieves good performance at $B_{1,\max} \sim 1.3$ kHz, whereas the HS1 pulse requires $B_{1,\max} \sim 2.5$ kHz to achieve the same inversion. When the different amplitude modulation functions are taken into account, the average RF amplitude $B_{1,\mathrm{rms}}$ is roughly similar for both pulses. The HS8 pulse is therefore a good choice when the maximum RF amplitude is limited, whereas the HS1 provides a sharper inversion profile with narrower transition bands. At low R values, the HS8 pulse does not adequately satisfy the adiabatic condition, making the HS1 pulse the only valid choice. The AFP pulse described by equations (5.11) and (5.12) behaves very differently from the HS1 and HS8 pulses. Even though the minimum R value to achieve adequate performance is much higher, the pulse performs well at relatively low $B_{1,\max}$. In addition, while HS1 and HS8 achieve frequency-selective inversion independent of the applied RF amplitude, the inversion bandwidth of the NOM AFP pulse increases with increasing $B_{1,\max}$. This is because the NOM AFP pulse does not exhibit OIA. As a result, the NOM AFP pulse is an excellent choice for inversion over wide bandwidths, whereas the HS1 and HS8 are better choices for frequency-selective inversion as required in spatial localization. The exact performance of a given AFP pulse is not easily deduced from visual inspection of the $B_1(t)$ and $\Delta\nu(t)$ modulation functions. Instead, the pulse performance should be calculated using the Bloch equations (Figure 5.3) or experimentally calibrated (see Section 5.3).

5.2.3 AFP Refocusing

As shown in Figures 5.2 and 5.3, AFP pulses demonstrate a superb performance for inverting longitudinal magnetization ($M_z \to -M_z$). However, other rotations such as excitation ($M_z \to M_x$) and refocusing ($M_x + iM_y \to M_x - iM_y$) are equally important for a wide range of experiments. The primary difference between M_z and M_{xy} during an AFP pulse is that M_z is initially parallel to $B_e(0)$, whereas M_{xy} is initially perpendicular to $B_e(0)$. When the effective field $B_e(t)$ rotates slowly relative to its amplitude, that is, when $|\mathrm{d}\alpha(t)/\mathrm{d}t| \ll |B_e(t)|$, M_z remains parallel to $B_e(t)$, which ultimately leads to spin inversion. Similarly, provided that the adiabatic condition is satisfied, M_{xy} will remain perpendicular to $B_e(t)$ throughout the pulse, leading to an inversion of the xy-plane, that is, refocusing. However, the refocusing properties are compromised as the transverse magnetization has acquired a phase angle $\beta(t)$ due to precession around $B_e(t)$ given by:

$$\beta(t) = 2\pi\int_0^t B_e(t)\mathrm{d}t \tag{5.13}$$

where $B_e(t)$ is the effective magnetic field given by equation (5.7). Figure 5.4 shows the effects of an AFP pulse on the three magnetization components M_x, M_y, and M_z. The AFP pulse achieved B_1 insensitive (Figure 5.4b) and frequency-selective (Figure 5.4c) inversion when starting with M_z before the pulse. Using M_x or M_y as a starting point before the AFP pulse will lead to B_1- and offset-dependent signal dephasing (Figure 5.4d and e) according to equation (5.13). The

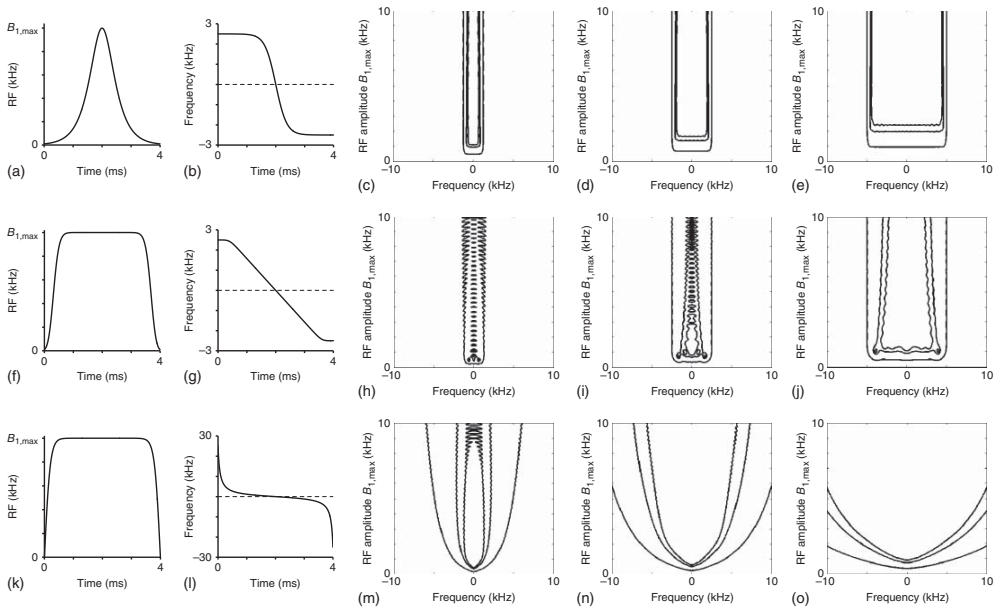

Figure 5.3. (a, f, k) Amplitude and (b, g, l) frequency modulation functions for (a, b) HS1 ($R = 20$), (f, g) HS8 ($R = 20$), and (k, l) NOM ($R = 200$) AFP pulses. Inversion profiles as a function of RF amplitude $B_{1,max}$ and frequency offset for (c–e) HS1, (h–j) HS8, and (m–o) NOM AFP pulses. HS1 and HS8 AFP pulses were executed with (c, h) $R = 10$, (d, i) $R = 20$, and (e, j) $R = 40$, whereas the NOM pulse was executed with (m) $R = 100$, (n) $R = 200$, and (o) $R = 400$. Contour lines are shown for $M_z/M_0 = -0.98$ (inner line), -0.90 (middle line), and 0.00 (outer line)

presence of RF inhomogeneity and different frequencies will lead to phase cancelation and signal loss. In other words, a single AFP pulse is a good inversion pulse, but it is a poor choice for signal refocusing as required in a spin-echo sequence.

Conolly *et al.*[13,14] were the first to recognize that the application of additional AFP pulses could rewind the phase acquired during the first AFP pulse. After the initial description of a 3π pulse, consisting of three AFP pulses of various lengths, Conolly *et al.*[14] subsequently proposed the use of two identical AFP pulses to rewind undesirable phase accumulation. Figure 5.4(f) shows the pulse sequence element in which two identical AFP pulses are surrounded by delays to form a double spin-echo. The phase accumulated during the first pulse according to equation (5.13) is canceled by the second RF pulse, such that the transverse magnetization phase is constant as a function of RF amplitude (Figure 5.4i) and frequency offset (Figure 5.4j). For the longitudinal magnetization, the AFP pulse pair acts as a 2π pulse, bringing the magnetization back to the $+z'$-axis when the RF pulse satisfies the adiabatic condition. The AFP-based double spin-echo element provides very robust slice selection when the pulses are executed during magnetic field gradients.

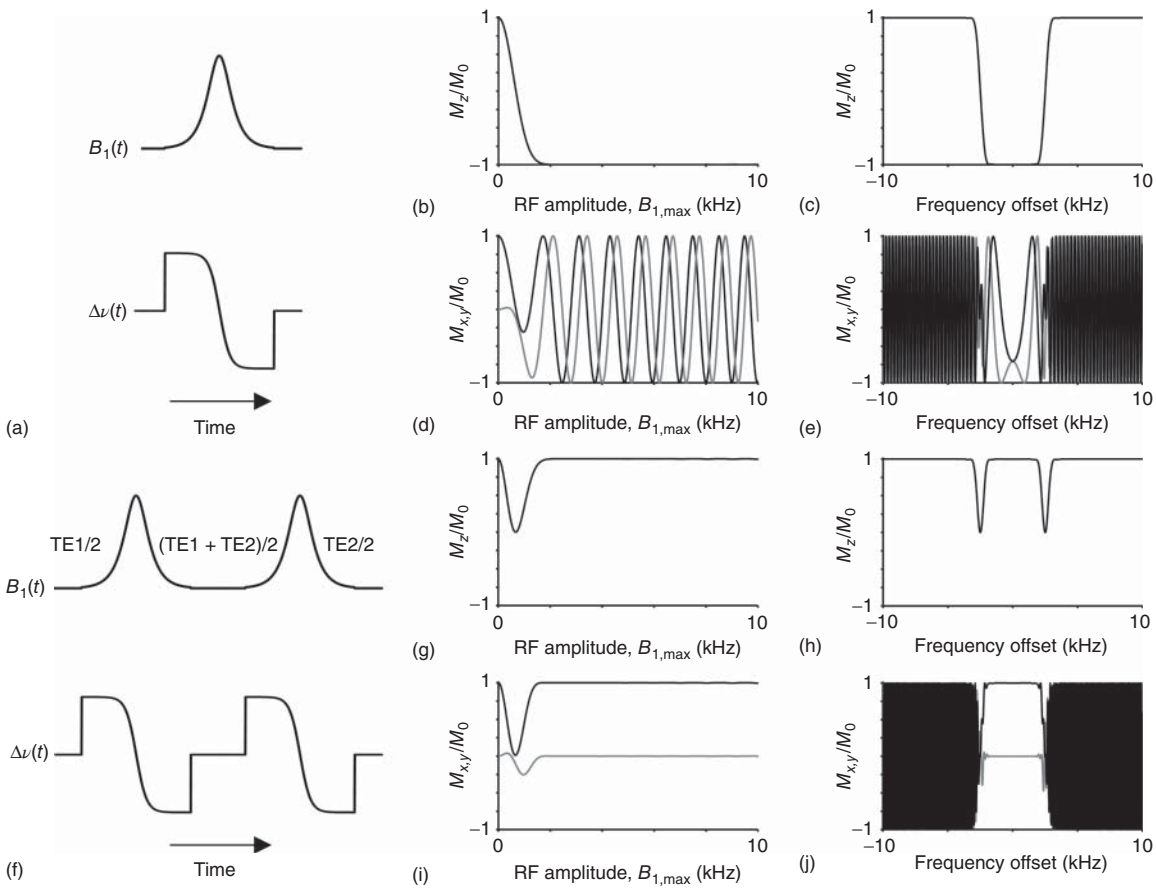

Figure 5.4. Inversion and refocusing properties of (a–e) single and (f–j) double AFP pulses. (a) A single AFP pulse achieves (b) B_1-independent inversion above a minimum threshold B_1 and (c) frequency-selective inversion. (d, e) Using a single AFP pulse for refocusing leads to a (d) B_1 and (e) frequency-dependent phase. (f) A double AFP pulse sequence achieves an identity (or 2π) rotation that is (g) B_1 independent and (h) frequency selective. Using the AFP pulse pair for refocusing eliminates the (i) B_1 and (j) offset-dependent phase roll

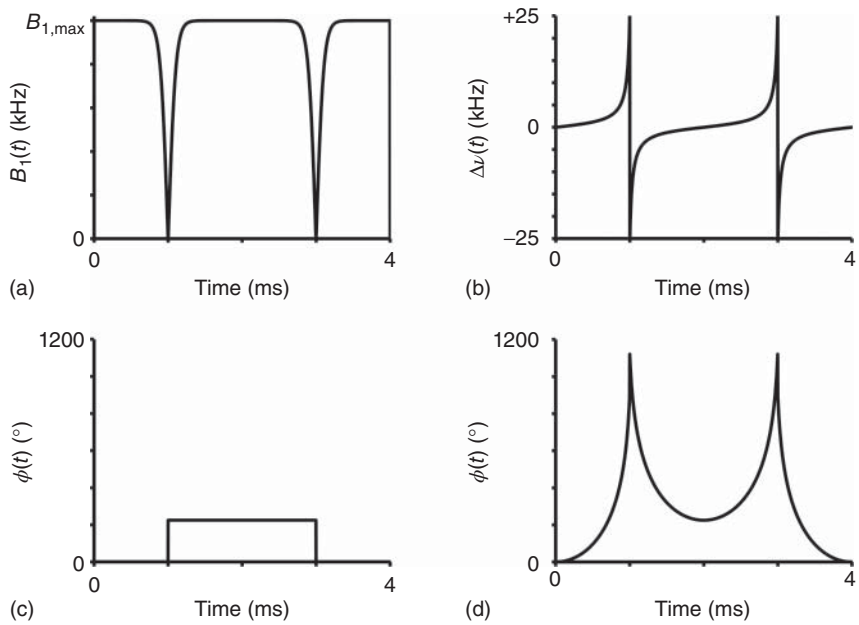

Figure 5.5. (a) Amplitude and (b) frequency modulations of a BIR-4 pulse, based on the modulation functions given by equations (5.11) and (5.12). (c) A phase offset of the middle two segments by $180° + \theta/2$ leads to a final, B_1-independent nutation angle of θ. (d) Phase modulation obtained by numerical integration of the frequency modulation in (b) and the addition of the discrete phase jumps of (c)

5.2.4 Adiabatic Plane Rotation of Arbitrary Nutation Angle

As noted, AFP pulses are an excellent choice for spin inversion. While a single AFP pulse is not suitable for spin refocusing, the combination of two AFP pulses allows the formation of a perfectly refocused, frequency-selective spin-echo. When an AFP pulse is only executed until its midpoint in time, the pulse achieves B_1-insensitive excitation albeit forfeiting frequency selectivity. Unfortunately, the AFP pulse is not suitable for any other rotations that, for example, require plane rotations or arbitrary nutation angles. The B_1-insenstive rotation using 4 segments (BIR-4) pulse is a plane rotation pulse that can achieve arbitrary nutation angles with high immunity to both RF inhomogeneity and resonance offsets. BIR-4 was derived from composite pulses, which are composed of multiple hard RF pulses that compensate each other's imperfections. Garwood and Ke[12] generated a time-symmetric, composite pulse $90°_{0°}180°_{180°+\theta/2}90°_{0°}$, which can achieve an arbitrary nutation angle θ simply by changing the phase of the center 180° pulse. The immunity toward RF inhomogeneity and frequency offset could be greatly enhanced by replacing the hard RF pulses with AFP pulse segments as shown in Figure 5.5. Without the phase offset for the middle two 90° segments, the pulse would simply generate an identity (or 360°) rotation. However, with a phase offset of $180° + \theta/2$ for the middle two segments, an arbitrary nutation angle θ can be achieved. In addition, the time symmetry of BIR-4 ensures that the net rotation angle of the magnetization around the effective field according to equation (5.13) is zero, thus making BIR-4 a general purpose, plane rotation pulse. BIR-4 has found applications in MRI,[15,16] polarization transfer,[17,18] spectral editing,[19,20] T_1 relaxation measurements,[21,22] and saturation transfer.[23]

5.3 APPLICATIONS

The use of adiabatic RF pulses is widespread in MRS applications. This is not surprising as many MRS studies are sensitivity limited and are therefore often performed with surface coil transceivers. The immunity

of adiabatic RF pulses to RF inhomogeneity ensures maximum sensitivity, while at the same time providing convenient and user-friendly MR methods that guarantee optimal performance without subject-specific adjustments of RF transmit power settings. Here, three MRS applications are discussed that demonstrate some of the features of adiabatic RF pulses.

5.3.1 3D Spatial Localization

Image-selected in vivo spectroscopy (ISIS)[24] and localization by adiabatic spin-echo refocusing (LASER)[5,25] are two spatial localization methods that are entirely based on adiabatic RF pulses. ISIS is based on the inversion properties of AFP pulses, whereas LASER is based on the refocusing properties of AFP pulse pairs. Figure 5.6 shows the ISIS and LASER pulse sequences with HS1 pulses for inversion/refocusing and a BIR-4 pulse with modulations given by equations (5.11) and (5.12) for excitation. The ISIS method sequentially executes the eight on/off combinations of the three AFP pulses, which in conjunction with an appropriate receiver phase cycle leads to 3D localization due to cancelation of signals that are not affected by all three RF pulses. Magnetic field crusher gradients following each AFP pulse ensure the elimination of spurious signals from outside the volume of interest. The main advantage of ISIS localization is that it can be placed before any excitation sequence, enabling very short or zero echo-time acquisitions. The primary disadvantage is that multiple scans are required to achieve 3D localization, thereby introducing sensitivity to subject motion and to system instability.

In 3D LASER (Figure 5.6b), the AFP pulses are executed following excitation, permitting single-scan 3D localization at the cost of a longer, minimum echo time (TE). On animal scanners, the minimum TE is often determined by the available RF peak power and gradient slew rates, which typically accumulate to TE_{min} values of 15 ms or less. On high-field human scanners, the minimum TE is often dictated by RF power deposition making TE_{min} 50 ms or longer. In order to reduce TE while still retaining most of the 3D LASER benefits, the semi-LASER sequence has been described[26,27] in which one pair of AFP pulses is eliminated and replaced by a slice-selective (but non-adiabatic) excitation pulse.

Figure 5.7 shows a practical example of ^{1}H MRS based on 3D LASER localization on the human leg at 7 T. A visually intuitive and straightforward manner to calibrate the AFP pulses is to extend the LASER sequence with a readout gradient during signal acquisition. Fourier transformation of the gradient-echo signal provides a 1D spatial profile of the localized volume along the selected direction. Increasing the RF power (Figure 5.7b) brings the AFP pulses closer to the point where the adiabatic condition, equation (5.7), is adequately satisfied. At about 0.9 kW, the intensity of the spatial profile levels off, indicating that the adiabatic RF pulses have reached the minimum threshold to satisfy the adiabatic condition. Increasing the transmit power increases the power deposition without any further benefit in sensitivity or localization quality. It is therefore advisable to set the transmit power 1–2 dB above the minimum threshold power to ensure that the spatial localization quality is maintained on all subjects, despite small differences in RF coil performance. It should be noted that the power requirements for the 3D LASER AFP refocusing and BIR-4 excitation pulses are most likely different, just as the performance of AFP pulses varies with different modulation functions (Figure 5.3). It is therefore advisable to calibrate the AFP pulse power first (at a constant excitation pulse power), after which the BIR-4 pulse power can be calibrated. Further note that while a BIR-4 pulse may work satisfactorily on-resonance at low RF power, it may require substantially more RF power to achieve the desired nutation angle over the full spectral width.

5.3.2 Outer Volume Suppression

Spatial localization is an important component of any MRS study and adiabatic RF pulses can be utilized in a number of them as described for ISIS and LASER. For relatively homogenous 'volume' coils, non-adiabatic localization methods such as stimulated echo acquisition mode (STEAM)[28] and point-resolved spectroscopy (PRESS)[29] can provide reasonable localization at short TE values without high RF power deposition. However, modest RF inhomogeneity, imperfect RF pulse profiles, and finite T_1 relaxation times can all compromise localization performance. In these cases, localization can be significantly improved by employing a secondary localization method such as outer volume suppression (OVS).

OVS is achieved with a frequency-selective excitation pulse followed by a magnetic field crusher gradient. Figure 5.8(a) shows the OVS performance of a 1 ms conventional, amplitude-modulated SLR

pulse at $B_{1,\max} = 1.5$ kHz. As the nutation angle of a single pulse is close to 90°, the OVS performance is good and covers about 6.0 kHz. As the OVS module is repeated three times to enhance the insensitivity to RF inhomogeneity, a slight mismatch (of up to ±10%) of the 90° nutation angle does not severely compromise the OVS performance. Figure 5.8(a) also shows the OVS performance of a 1-ms HS4 pulse ($R = 20$) at $B_{1,\max} = 1.5$ kHz. While OVS based on HS4 pulses executed under nonadiabatic conditions has the same sensitivity toward RF inhomogeneity as the SLR-based OVS shown in Figure 5.8(a), there are two distinct advantages for using HSn pulses for OVS. First, as discussed previously[6,30] the frequency-selective profile of HSn pulses remains constant even when executed in a non-adiabatic

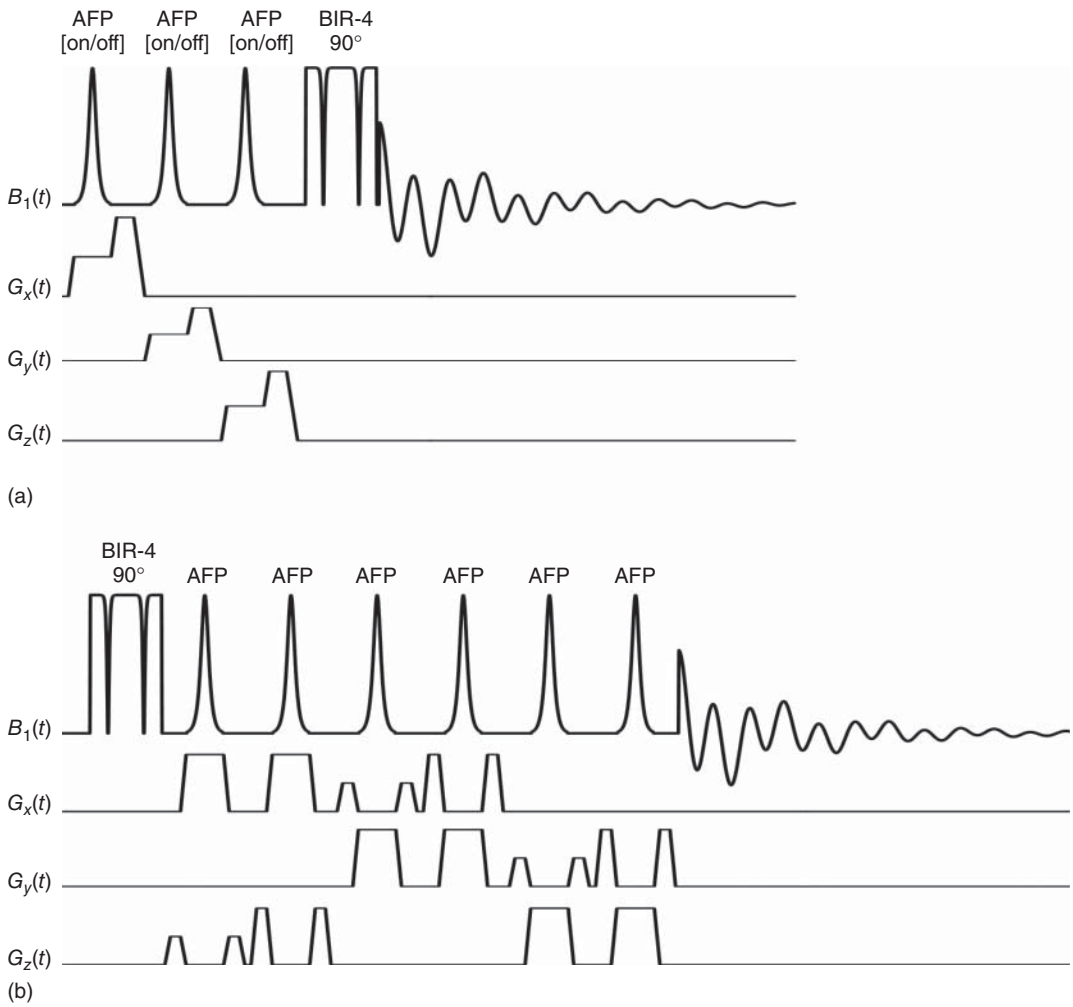

Figure 5.6. 3D spatial localization methods based on AFP pulses. (a) ISIS and (b) LASER. (a) The ISIS sequence requires a minimum of eight acquisitions to execute all on/off combinations of the three AFP pulses in order to achieve complete 3D localization. During the off condition, the gradients are retained to keep the eddy current response identical for all acquisitions. As localization is achieved based on the longitudinal magnetization, any excitation pulse sequence can follow the ISIS module. (b) LASER is based on the refocusing properties of AFP pulse pairs (Figure 5.4). By executing three AFP pulse pairs along orthogonal directions, complete 3D localization is achieved in a single acquisition. Surrounding each AFP pulse with unique crusher gradients is essential for eliminating artifacts

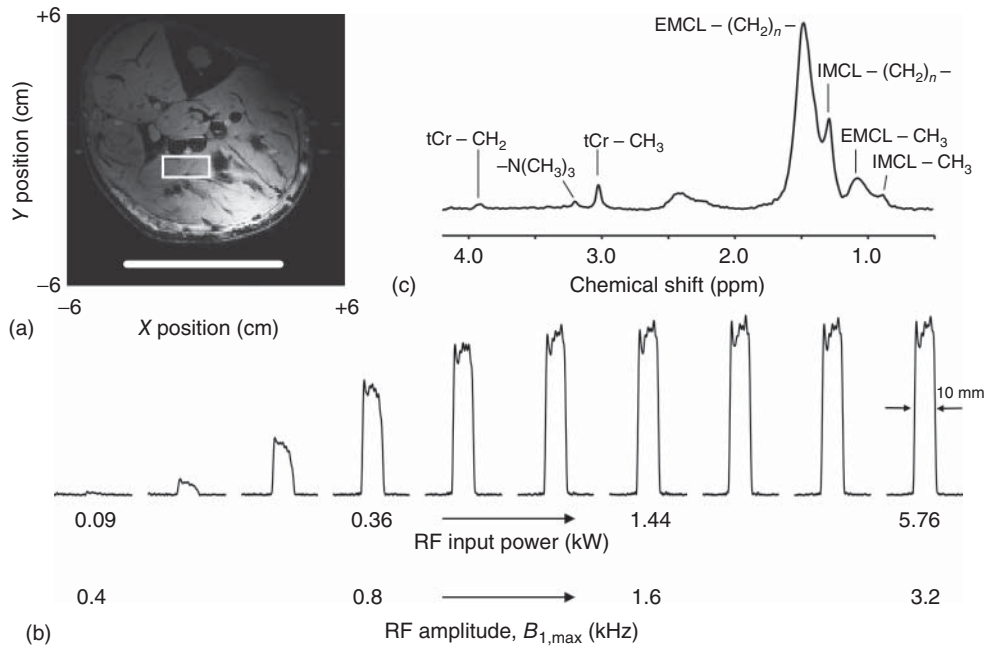

Figure 5.7. (a) MR image of the human leg at 7 T indicating a 25 mm × 10 mm × 20 mm volume and an 80 mm diameter surface coil transceiver. (b) Calibration of the AFP pulse power (6 ms HS1, $R = 20$) on 1D spatial profiles. The RF power increases in steps of 2 dB, leading to a doubling of $B_{1,\max}$ every three profiles. The signal from the 3D localized volume increases with increasing RF power until the adiabatic condition is adequately satisfied ($B_{1,\max} \sim 1.2$ kHz). Increasing the RF power further does not lead to improved performance but does increase the RF power deposition. (c) 3D LASER ^{1}H MR spectrum obtained without any secondary localization technique (TR = 4000 ms, TE = 150 ms, NA = 64)

power regime. As such, the OVS slice profile is well behaved despite the presence of strong RF inhomogeneity. For most amplitude-modulated pulses, the frequency-selective profile greatly deteriorates when the nutation angle deviates from the range for which the pulse was optimized. In those cases, the OVS slice profile can be heavily distorted and even suppress desirable signals. Second, at the same maximum RF amplitude of 1.5 kHz, the HS4 pulse achieves >20 kHz bandwidth, more than three times that achieved by the SLR-based OVS. This increased bandwidth reduces chemical shift displacement artifacts, which are especially prominent at high magnetic fields (Figure 5.8b and c).

Figure 5.8(e) shows 1D spatial profiles of the human brain at 7 T (Figure 5.8(d)) along the Y direction, perpendicular to the plane of the surface coil transceiver. The spatial profile shows clear signals from water and lipids in the skull region that are largely removed with OVS without affecting the brain signal. Experimental calibration of OVS transmit power (Figure 5.8f) is similar to that of the LASER AFP pulses with the exception that the OVS pulses behave non-adiabatically. Therefore, the OVS performance does not level off, but rather hits a maximum before deteriorating at higher power levels. The immunity of the non-adiabatic OVS module can be increased by repeating the OVS modules or by imposing additional amplitude modulation between the OVS modules.[30] Figure 5.8(g) shows a 3D STEAM-localized ^{1}H NMR spectrum from the human brain at 7 T without OVS as a secondary localization method. The spectral quality is high as judged by the narrow spectral lines and the high sensitivity. However, visible artifacts from extracranial lipids are visible in the 1.0–2.0 ppm region. These lipid signals obscure signals from lactate and alanine and may even compromise the rest of the spectrum when sufficiently intense. Figure 5.8(h) shows the same spectrum acquired in the presence of complementary HSn-based OVS modules. The majority of the spectrum is unaffected, but the artifactual lipid signals have been suppressed to below the spectral noise floor.